AN ABSTRACT OF THE DISSERTATION OF

Mathew A. Cleveland for the degree of Doctor of Philosophy in Nuclear Engineering presented on December 2, 2011.
Title: Radiative Heat Transfer in Combustion Applications: Parallel Efficiencies of Two Gas Models, Turbulent Radiation Interactions in Particulate Laden Flows, and Coarse Mesh Finite Difference Acceleration for Improved Temporal Accuracy

Abstract approved: _____

Todd S. Palmer

We investigate several aspects of the numerical solution of the radiative transfer equation in the context of coal combustion: the parallel efficiency of two commonly-used opacity models, the sensitivity of turbulent radiation interaction (TRI) effects to the presence of coal particulate, and an improvement of the order of temporal convergence using the coarse mesh finite difference (CMFD) method.

There are four opacity models commonly employed to evaluate the radiative transfer equation in combustion applications; line-by-line (LBL), multigroup, band, and global. Most of these models have been rigorously evaluated for serial computations of a spectrum of problem types [1]. Studies of these models for parallel computations [2] are limited. We assessed the performance of the Spectral-Line-Based weighted sum of gray gasses (SLW) model, a global method related to K-distribution methods [1], and the LBL model. The LBL model directly interpolates opacity information from large data tables. The LBL model outperforms the SLW model in almost all cases, as suggested by Wang et al. [3]. The SLW model, however, shows superior parallel scaling performance and a decreased sensitivity to load imbalancing, suggesting that for some problems, global methods such as the SLW model, could outperform the LBL model.

Turbulent radiation interaction (TRI) effects are associated with the differences in the time scales of the fluid dynamic equations and the radiative transfer equations. Solving on the fluid dynamic time step size produces large changes in the radiation field over the time step. We have modified the statistically homogeneous, non-premixed flame problem of Deshmukh et al. [4] to include coal-type particulate. The addition of low mass loadings of particulate minimally impacts the TRI effects. Observed differences in the TRI effects from variations in the packing fractions and Stokes numbers are difficult to analyze because of the significant effect of variations in problem initialization. The TRI effects are very sensitive to the initialization of the turbulence in the system. The TRI parameters are somewhat sensitive to the treatment of particulate temperature and the particulate optical thickness, and this effect are amplified by increased particulate loading.

Monte Carlo radiative heat transfer simulations of time-dependent combustion processes generally involve an explicit evaluation of emission source because of the expense of the transport solver. Recently, Park et al. [5] have applied quasi-diffusion with Monte Carlo in high energy density radiative transfer applications. We employ a Crank-Nicholson temporal integration scheme in conjunction with the coarse mesh finite difference (CMFD) method, in an effort to improve the temporal accuracy of the Monte Carlo solver. Our results show that this CMFD-CN method is an improvement over Monte Carlo with CMFD time-differenced via Backward Euler, and Implicit Monte Carlo [6] (IMC). The increase in accuracy involves very little increase in computational cost, and the figure of merit for the CMFD-CN scheme is greater than IMC.

Radiative Heat Transfer in Combustion Applications: Parallel Efficiencies of Two Gas Models, Turbulent Radiation Interactions in Particulate Laden Flows, and Coarse Mesh Finite Difference Acceleration for Improved Temporal Accuracy

by

Mathew A. Cleveland

A DISSERTATION

submitted to

Oregon State University

in partial fulfillment of
the requirements for the
degree of

Doctor of Philosophy

Presented December 2, 2011
Commencement June 2012

Doctor of Philosophy dissertation of Mathew A. Cleveland presented on December 2, 2011.

APPROVED:

Major Professor, representing Nuclear Engineering

Head of the Department of Nuclear Engineering and Radiation Health Physics

---

Dean of the Graduate School

I understand that my dissertation will become part of the permanent collection of Oregon State University libraries. My signature below authorizes release of my dissertation to any reader upon request.

Mathew A. Cleveland, Author

ACKNOWLEDGEMENTS

I would like to thank Dr. Palmer my advisor for all of his support and help throughout my graduate career. I would also like to thank Dr. Cathy Summers for over seeing the contract which funded my research. This work was supported by the Department of Energy-National Energy Technology Laboratory Contract No. 41817M4077. Finally, I would also like to thank my family for there love and support.

TABLE OF CONTENTS

TABLE OF CONTENTS (Continued)

Page

TABLE OF CONTENTS (Continued)

Page

LIST OF FIGURES

LIST OF FIGURES (Continued)

LIST OF FIGURES (Continued)

LIST OF TABLES

LIST OF TABLES (Continued)

Radiative Heat Transfer in Combustion Applications: Parallel Efficiencies of Two Gas Models, Turbulent Radiation Interactions in Particulate Laden Flows, and Coarse Mesh Finite Difference Acceleration for Improved Temporal Accuracy

1 Introduction

With growing concerns over global warming, industries have been called upon by their federal and local governments to significantly reduce waste and environmental impact. The coal power industry has come under significant scrutiny because many attribute global warming to the excessive release of CO_2 into the environment. Coal, which accounts for approximately 51% of the electricity transmitted by the U.S. power grid, releases millions of tons of CO_2 into the atmosphere annually[8]. In an attempt to adapt to the changing market, coal power producers are turning to "clean coal" technologies to mitigate their environmental impact. One such clean coal technology is pulverized oxy-coal combustion[9]. This technology relies on the combustion of pulverized coal in an oxygen-rich environment. Oxygen is introduced into the system and the flue gas is recycled during the combustion resulting in a more complete combustion of the coal and reduction of the harmful nitrates in the flue gas. It also increases the carbon dioxide concentration, which increases the efficiency of carbon sequestering systems.

Changing or building new coal combustion systems will be an expensive and complicated procedure. There are still many unknown factors when dealing with combustion systems of this nature, such as flame temperatures and combustion rates. Some of these factors can be estimated experimentally, but others are either too expensive or unsafe to determine physically. This leaves computational models

as the best alternative. These models must account for the wide variety of physical phenomena which occur in these systems such as fluid flow, heat transfer, and chemical reactions. This dissertation is concerned with the numerical simulation of radiative heat transfer in oxy-coal combustors.

Radiative heat transfer (RHT) is the dissipation or transfer of energy via photon emission and interactions. This is one of the three modes of heat transfer. In most heated systems, these three heat transfer modes; conduction, convection, and radiative heat transfer, are all present together. In many cases, however, one or two heat transfer modes are dominant, such that the others can be neglected.

Numerical approaches to solving the RHT equations in combustion applications have been available for a long time[10]. For some simple systems, the RHT equations can be solved analytically; but for most practical applications, this is not the case. If an analytical solution is not possible, it is necessary to solve the equations using either deterministic, stochastic, or hybrid numerical methods. Deterministic methods rely on discretizations of the partial differential equations in each of the independent variables to generate a linear (or non-linear) system of algebraic equations, which can be used to solve for the specific intensity or energy density of the radiation. Stochastic methods rely random sampling of probabilities distribution functions to evaluate different physical or mathematical systems[11].

The Monte Carlo method is a stochastic method that can be used to evaluate particle transport[11]. In this method, discrete energy packets are sampled from the probability distribution of source emission, and these energy packets are then "transported" using a random walk algorithm. In a random walk, (pseudo) random numbers are used to sample from probability distributions which describe the possible interactions of energy packets in the problem domain. In most stochas-

tic methods, the exact solution to the original partial differential equations will be preserved if an infinite number of energy packets are created and transported through the system using the defined probabilities.

There are advantages and disadvantages to solving these equations with either stochastic or deterministic methods. Stochastic methods are inherently parallelizable, because the random walk of one energy packet is independent of all the others. Therefore, if the volume in which the random walk takes place can be represented explicitly on a single processor, the processor can independently calculate the history of that energy packet. Deterministic methods are generally not considered to be as easy to parallelize as stochastic methods. This is because the solution of the linear (or non-linear) system is strongly dependent on the entirety of the matrix. This is particularly true for dense or ill-conditioned matrices. On serial computers, however, deterministic solvers are generally faster than stochastic solvers. Another drawback of stochastic methods is that solutions suffer from statistical noise, whereas deterministic solutions do not. Deterministic methods generate results throughout the problem domain, whereas stochastic methods are often used to generate solutions in user-specified subdomains of the problem. Most deterministic methods suffer from truncation errors that arise from spatial, angular, energy and/or temporal approximations. These can also be found in some stochastic methods when the material and geometric representations must be approximated.

Radiative heat transfer problems can be parallelized in two ways; domain repetition and domain decomposition. *Domain repetition* creates identical physical domains that are translated onto multiple processors. In the case of deterministic methods, this can be useful in solving multifrequency problems where each proces-

sor will solve a matrix for a different frequency. In problems where frequencies are dependent on one another (i.e. problems with scattering), intermittent communication between processors would be necessary. Stochastic methods can replicate the domain on every processor and allow each processor to transport discrete energy packets on the entirety of the mesh. At the end of the simulation, the results on each individual processor can be combined to obtain the final solutions.

Domain decomposition is when the problem domain is divided into multiple volumes and each is placed on its own processor. Domain decomposition can be further divided into overlapping (Schwarz) methods and iterative substructuring (non-overlapping) methods[12]. Deterministic methods will generally require an outer iteration on the solution of the shared boundaries of the domains. Stochastic methods can also be used in this way, but more commonly, stochastic packets are communicated between domains during the calculation. Both parallelization techniques can be used together, creating a simulation with both domain repetition and domain decomposition.

Domain repetition for stochastic methods appears to be the most attractive parallelization technique because each processor can run completely independent of the others. Most real problems of interest, however, are far too large to fit the entire domain in the memory of a single processor. This limits both deterministic and stochastic methods to domain decomposition with the optional addition of domain repetition. Domain decomposed simulations have the additional cost of interprocessor communication, and suffer (potentially) from load balancing issues. The *load balance* of a system is how well the computational work is distributed over the number of processors. In a perfectly balanced parallel system, all processors share the computational load equally.

The selection of opacities models, which approximates the fundamental opacity data that describes photon interactions with materials, is very important with regards to computational efficiency and parallel performance. Gas opacities wildly vary in magnitude as a function of frequency. This is because the material emit and absorb photons that match discrete quantum changes of their associated gas molecules[13]. This makes developing multifrequency models very difficult. Most frequency integration methods are independent of the solution method (stochastic or deterministic); however, their implementation, efficiency, and accuracy may vary with transport solver being used. For the purpose of this work, the focus will be on frequency integration methods as they relate to radiative heat transfer solved via stochastic methods. Multifrequency methods can be broken down into five primary types; line-by-line(LBL), multigroup, narrow band, wide band, and global models[1]. The first attempt to solve a frequency dependent radiative transfer problem via Monte Carlo, as noted by Wang et al.[14], was Modest in 1992 with a statistical narrow band model. The narrow band model is now only one of the many models that have been employed to solve the radiative transfer equation with a Monte Carlo scheme.

Heterogeneous transport has been extensively studied, particularly in the field of neutron transport, since the 1940's[15]. Pulverized coal combustion encounters many material heterogeneities such as flue gas, coal particles, fly ash, and char. These heterogeneities can best be described as stochastic mixtures. A stochastic mixture is a combination of two or more materials that can be defined by a statistical distribution. Work by Marakis et al. showed that wall heat fluxes are strongly affected by the presence of each of these materials [16]. Particle interactions in radiative heat transfer account for four different phenomena [1]; diffraction, refrac-

tion, reflection, and absorption. Diffraction is the scattering of photons from one direction to another when they pass near a particle. Refraction is when a particle enters a material and then leaves at a different angle. Reflection is when a photon is immediately redirected off the surface of a particle. Absorption is when the energy of a photon is fully deposited into a particle. There are a variety of ways to predict and account for these different phenomena, including Lorenz-Mie theory, Rayleigh theory, and geometric optics. The accuracy of each method is greatly dependent on the frequency of the photon, the particle size, and particle material properties [1].

The growing availability of computational resources allows researchers to solve increasingly complex systems of equations. For combustion modeling, these resources are used to evaluate a coupled system of equations; conservation of mass, conservation of momentum, conservation of energy, speciation, rate kinetics, and the radiative transfer equation. Coupling radiation with fluid flow presents number of difficulties including significant time scale differences, the existence of turbulent radiation interaction effects (TRI), errors associated with operator splitting, and difficulties resolving the non-linearities between the equations.

Turbulent radiation interaction effects (TRI) occur because of the difference in time scale of the radiative transfer equation and the fluid dynamic equations[1]. The time scale of the radiative transfer equation is on the order of the speed of light, whereas the time scale of the fluid dynamic equations is on the order of the speed of sound. This implies that if the radiative transfer equations are solved over typical time scales of the fluid dynamics equations, the radiative transfer solution will appear to be steady state. This has little effect for problems that are fully developed and laminar because there is little variation in the material properties

over a time step. However, if the flow is not fully developed, or turbulent, then strong fluctuations of the material properties can occur over a fluid time step. Since the radiative transfer equation is near steady state for these large time steps, the fluctuations in the material state are felt instantaneously for both local and global quantities of the radiative transfer equations. Neglecting these effects creates overestimates of mean material temperatures and underestimates of the mean heat fluxes at the boundaries[1].

One of the non-linearities that occurs in these coupled combustion systems is the feedback between the radiation and fluid fields[1]. These equations are generally solved independently and coupled through the conservation of energy equation. This equation evaluates changes in the material properties that drive both equations. Converging the non-linearities between the fluid and radiation generally requires that both fields be evaluated multiple times for every time step. This can be very expensive, even in very parallelized systems. High-order/low-order solvers are advantageous in improving the efficiency of these types of problems. High-order solvers, such as Monte Carlo, can resolve a larger amount of detail (such as angular, spatial, and frequency dependence) than low-order problems. This comes at the cost of increased computation time. These high-order/low-order schemes attempt to reduce the computational cost by using multiple iterations of the low-order problem, and only space iterations of the high-order scheme, to converge non-linearities in the equations. This results in a similar amount of detail and accuracy, as compared to the high-order scheme, at a reduced computational cost.

To decrease the computational cost of solving the radiative transfer equation multiple times, a low-order scheme could be used for the majority of these iter-

ations, during a time step. Course Mesh Finite Difference (CMFD) is one such high-order/low-order scheme. Course Mesh Finite Difference (CMFD) has been successfully applied as an acceleration technique in which a coarsened solution is used to approximate the fine solution. This course solution is coupled to the fine solution in such a way that cell currents are preserved, using a correction term which is applied to the mean opacity at the cell faces [17]. CMFD has been shown to be advantageous in acceleration k-eigenvalue problems[18, 19]. A similar high-order/low-order scheme known as the quasi-diffusion[20] has also been used as an acceleration technique. Park and Knoll[5] have implemented quasi-diffusion to the thermal radiation transport equations, using the zeroth and first order angular moments as the low-order solver and Monte Carlo as the high-order solver. They successfully accounted for the non-linearities in the source emission term, however, they did encounter an amplification in Monte Carlo noise.

1.1 Research Questions

The following research questions are addressed in this work;

1. How do different opacity models compare in scalability and computational efficiencies on parallel architectures?

2. How does the presence of coal particulate affect turbulence radiation interaction effects?

3. How does the temporal truncation error in the low-order solution of a CMFD scheme affect the convergence of the high-order solution?

1.2 Literature Review

This section contains a review of the literature on frequency dependent radiative heat transfer methods, turbulence radiation interactions, and temporal integration schemes for numerical solution of the radiative heat transfer equation.

1.2.1 Frequency Dependent Radiative Heat Transfer

The line-by-line (LBL) method is considered the most accurate way to account for frequency dependence; however, the extraordinary cost of implementing LBL methods makes them unattractive for some applications [13, 1]. The line-by-line method constructs opacities based on spectral line databases, such as HITRAN, and solves the radiative transfer equation for several hundred thousand wavenumbers [1]. Some improvements have been made to the efficiency of line-by-line methods. Wang et al. [14] developed a line-by-line Photon Monte Carlo method which, as expected, is very accurate. Surprisingly, this method is also predicted to be faster than a global method for problems with significant time dependence.

Narrow band models make approximations about the overlapping characteristics of discrete lines, increasing the efficiency of the opacity calculation. Two of the most common models are the Elsasser model (which assumes a constant line intensity and shape) and statistical models (which assume a random distribution of intensity and shape). These methods are much faster and can be as accurate as the line-by-line method for homogeneous systems that are dominated by the black body emission spectrum [1]. However, this situation is rare in real problems of interest and significant errors occur when these criteria are not met [1, 13]. Narrow band models have also been integrated with global models with some success [1]. For these reasons, multifrequency development for radiative heat transfer to date

has been dominated by global methods.

Wide band models develop approximate opacity values and/or distributions of opacities associated with the primary absorbance bands for a given material. *Absorbance bands* are discrete ranges of frequencies that cover a particular vibrational-rotational absorbance and emission range. Correlations are then used to approximate how the opacity of each band is affected as a function of temperature and pressure. These methods have been explored in a great deal of detail by Edwards et al. [21, 22] It is common to find errors in excess of 30% for these methods [1]. Difficulties in these models include the selection of the band locations and the accuracy of their associated correlations.

A method of note that has been applied in combination with narrow band and wide band models is the K-distribution method [23, 1]. This method develops an opacity set where the opacities associated with different frequencies are reorganized to create a smooth function in opacity. Distribution functions are developed to accompany each new opacity function so they can appropriately account for emission strength. This method also has difficulties accounting for heterogeneities.

Global opacity integration methods create differential opacity intervals, known as *gray gases*, that are integrated over the entire frequency range. These methods are known to suffer significant errors when applied to heterogeneous problems. One example is the weighted sum of gray gases method which develops a variety of gray gases and their associated weights to account for emission strength. These weights are similar to the distribution functions used by the K-distribution method. Several variations of these methods have been developed to make them better suited for problems with heterogeneities [24]. Among these variations is the Spectral-Line-Based weighted sum of gray gases (SLW) [13] method, which has been shown to

be a coarse representation of the FSK model [1]. This method relies on either the correlated-K or scaled-K approximations [1]. The correlated-K approximation assumes that the reorganized opacity distributions at different material states can be connected via a correlation function [1]. The scaled-K approximation assumes that only the magnitude of the reorganized opacity distribution is changed between material states and therefore a scaling value can be applied to account for this shift.

A multigroup approach has been demonstrated both by Rodolphe [25] and Zhang et al. [23]. The approach taken by Zhang et al. generates multigroup opacities where opacites are grouped according to the absorption opacity dependency on partial pressure and temperature [23]. All wavenumbers that are found to have the same dependence on these quantities are placed in a group. They also applied the K-distribution method within the opacity groups.

Computational resources continue to rapidly grow, increasing the availability of hardware for solving larger and more complicated numerical systems. This, as of late, can be correlated with the heavy expansion of parallel systems ranging from heterogeneous super computers, such as the LANL Roadrunner machine [**?**], to multi-core GPUs and CPUs in personal computers. With the ever-expanding availability of these resources, it is necessary to analyze the scalability of numerical methods to help determine expected parallel performance.

Wang and Modest have demonstrated that the spectral LBL model has significant performance and accuracy advantages over the full-spectrum k-distribution(FSK) model in non-gray heterogeneous participating media when run in serial [3]. The SLW model is expected to have similar performance attributes to those found in the FSK model. Pal et al. show some parallel efficiency comparisons of the FSK model and the LBL model. In these comparisons the FSK models were solved

using P_1, P_3, and finite volume solvers. They evaluated average CPU times for a serial calculation and a single 16 processor run. These runs neglect communication cost and idle processor times because they use average CPU time as the numeric benchmark. The strong scaling efficiencies of the radiative transfer solvers varied between 75% for the LBL model and 97% for the FSK model with a P_1 solver [2].

1.2.2 Particulate, Radiation, and Turbulence

Four primary methods have been employed to solve stochastic mixture problems; the brute force method, atomic mixing, chord length sampling, and lattice structures [26]. A variety of sensitivity studies have been performed by Liu [27, 28] on particle size and temperature distributions. These studies show that radiative transfer, particularly in high-temperature environments, can be significantly affected by heterogeneities between particles.

A single realization of a stochastic mixture does not accurately reflect the true material distribution, but rather it represents a single probable portrait of a material. The brute force method relies on generating many different realizations of a stochastic mixture, solving each of these radiative transfer problems, and averaging their results. This approach has been shown to be very accurate, but its computational costs are prohibitively expensive for real problems of interest [26].

Atomic mixing methods approximate the optical properties of a stochastic mixture with a single opacity. This single opacity represents a statistical average of the heterogeneous material properties. Marakis et al.[16] used an atomic mixing model to account for coal particles, fly ash, and char to determine how mean flame temperature might be effected by their presence. This model was not used to compare with experimental results, but rather to benchmark heat flux sensitives to the

presence of different particles and scattering functions [16]. Atomic mixing models are generally fast and if opacities are appropriately averaged, the models will produce very accurate results. The difficulty here lies in generating the averaged opacities. If the true intensity is known throughout a cell that is being averaged, it is possible to generate an exact average opacity for the cell.

Chord length sampling coupled with a Monte Carlo algorithm has been explored heavily. The *chord length sampling* method generates a probability distribution function (PDF) that describes the distribution of the different materials which compose the stochastic mixture. This PDF is then used to determine the next probable location in which a photon might move to another material. If the distance to the next interaction is longer than the distance to the next material, it is assumed that the photon entered the new material at the closest location. This method can be very accurate, and in the case of a purely absorbing media with an infinite sampling, it will generate the exact solution. This is not the case for problems with scattering. The chord length sampling method makes the assumption that every segment of a photon history is uncorrelated [26]. This implies that if a photon is scattered back toward a sampled material, that material no longer exists as it was known to the photon on its previous history segment. This can cause significant errors in problems with appreciable backscattering.

Lattice models can be used to approximate heterogeneous materials. A lattice cell can be constructed such that the volume ratio of a single cell accurately portrays a designated material mixture. Multiple lattice cells can then be used to reproduce the heterogeneous material; however, numerical error can accumulate if the geometric randomness of the material is not accounted for. An example of this is the universe concept used in the Monte Carlo N-Particle code (MCNP) [29, 26].

Recently, stochastic lattices have been employed in MCNP with some very promising results [30, 26]. A stochastic lattice accounts for heterogeneities, similar to the standard lattice model, using lattice cells that account for statistical material compositions. These stochastic lattice cells are randomly filled with the stochastic material. This method suffers from problems similar to those of the chord length sampling method.

The difference in time scale of the radiative transfer equation and the fluid dynamic equations presents a unique phenomena. The time scale of the radiative transfer equation is on the order of the speed of light, whereas the time scale of the fluid dynamic equations is on the order of the speed of sound. This implies that if the radiative transfer equations are solved over typical time scales of the fluid dynamics equations, the radiative transfer solution will appear to be steady state. This has little effect for problems that are fully developed and laminar because there is little variation in the material properties over a time step. However, if the flow is not fully developed or turbulent, then strong fluctuations of the material properties can occur over a fluid time step. Since the radiative transfer equation is near steady state for these large time steps, the fluctuations in the material state are felt instantaneously for both local and global quantities of the radiative transfer equations. Neglecting these effects creates overestimates of mean material temperatures and underestimates of the mean heat fluxes at the boundaries.

The effects from Turbulence Radiation Interactions (TRI) in particulate laden flows can have a significant effect on thermal radiation fields and corresponding material heating [31]. Radiative heat transfer has been extensively studied in a variety of stochastic media including combustion problems [32, 33, 14, 31]. Most combustion problems contain strong heterogeneities which can be treated stochas-

tically. In pulverized coal combustion, these heterogeneities include particulate such as coal, fly-ash, and char [31, 16]. These materials are typically accounted for stochastically using an atomic mix model. TRI effects have been shown to be very sensitive to the presence of soot in turbulent flames, significantly decreasing mean flame temperatures [34].

This work expands upon a simplified test case, developed by Deshmukh et al. [4], to highlight the effects of fuel particulate on TRI phenomena. The code used in this work is a 3D parallel coupled radiative heat transfer and reacting fluid flow solver. The radiative heat transfer equation is solved via the Monte Carlo method. Radiation interactions with particulate can be accounted for either using Mie theory [35] or geometric optics [1] depending on particulate size. The reacting fluid flow model solves the continuity equation, the compressible or incompressible Navier-Stokes equations, the mixture fraction equations, and energy equation. The compressible Navier-Stokes equations are solved using a Large-eddy simulation (LES) [36] model, and particle-fluid interactions are accounted for using Discrete Element Modeling (DEM)[36].

Particulate properties, specifically material temperatures, can be treated in a variety of ways. Small particulate such as fly-ash, char, and very small coal particulate are typically chosen to exist at the mean cell temperature. This a relatively good assumption because these materials are physically very small and dissipate any excess heat very quickly. The coal particulate on the other hand can be more difficult because the relatively large size of the particulate means that it will have heat latency that should not be neglected. It is suggested that coal particulate likely remains close to the original inlet temperature and the majority of thermal emission occurs in the soot envelope that forms immediately around the

particulate during combustion [37].

Flamelet models can be used to determine fluctuations in the material properties as a function of time. This information can then be used to determine the approximate mean emission term over the time step. This is typically referred to as "full TRI" even though the two way coupling with the material energy density feedback is not iterated to convergence. Full TRI also assumes the mean absorption rate is equal to the mean opacity over the time step multiplied by the mean intensity. This is known as the optically thin eddy approximation and is, to date, made in every numerical evaluation of TRI effects.

1.2.3 Temporal Integration Schemes for the Radiative Heat Transfer Equation

Implicit Monte Carlo (IMC) methods were first introduced in computational physics by Fleck and Cummings in 1971 [6]. IMC was developed as an attempt to solve highly absorbing and reemitting photon transport problems. Competing Monte Carlo methods of the time were explicit in the time discretization. These discretizations were very capable of solving optically thin problems where the radiation and photon energy densities were significantly out of equilibrium. However, they had difficulties solving highly absorbing and reemitting problems where the photon energy density was nearly in equilibrium with the material energy density. For these problems the explicit methods required very small time steps [6].

Fleck and Cummings proposed the development of IMC as a solution method that would be unconditionally stable. They introduced the concept of "effective scattering". When the photon energy density of the system is nearly in equilibrium with the material energy density, many photons are absorbed and quickly re-emitted by the background medium. Explicit methods require very small time

steps to remain stable in this limit. IMC treats the absorption and quick re-emission of these photons as a single "effective scattering" event.

IMC has been shown to be very robust and stable for problems ranging from very thin to very thick. Though IMC is capable of producing accurate results in thick diffusive regions, it reaches this solution very slowly. This is because in thick diffusive regions the photon interactions are dominated by effective scattering events. As the probability of scattering increases, the length of time for a random walk increases. This makes IMC problems unacceptably slow. A variety of approaches have been proposed to rectify this problem including Symbolic Implicit Monte Carlo, Implicit Monte Carlo Diffusion (IMD), and Discrete Diffusion Monte Carlo (DDMC) [38].

An alternative to this approximate implicit method is to fully resolve the non-linear source emission term using a non-linear iterative scheme [39]. These non-linear iteration schemes are generally applied to only deterministic methods because of the need to perform many iterations. Fully converging the non-linear source term alleviates the problems with overheating and "teleportation errors" commonly found in the approximate implicit methods.

Course Mesh Finite Difference (CMFD), as outlined by Downer et al.[17], is an acceleration technique that uses a coarse solution, which is coupled to a fine solution, in such a way that cell currents are preserved using a correction term which is applied at the cell faces [17]. CMFD has been shown to be advantages in acceleration k-eigenvalue problems[18, 19]. Typically these methods rely on deterministic solutions for both the high-order and low-order problems limiting angular and frequency representations of the solutions.

Recently, Lee et al. [40] have shown that CMFD coupled to Monte Carlo can

significantly reduce the standard deviations in local quantities when applied to k-eigenvalue problems. This approach relies on a coarsened solution to the diffusion equation to converge the fission source. Wolters [41] has also demonstrated some modified CMFD approaches can be used to decrease the sensitivity of standard CMFD to statistical noise.

Park and Knoll have recently applied quasi-diffusion to the radiative heat transfer equations [5]. This approach uses the zeroth and first order angular moments as the low-order equations and Monte Carlo transport as the high-order solver. This implementation only relied on a single iteration of the high-oder solver per time step, rather than fully converging the differences between the low-order and high-order problems. This is because the overall cost of the Monte Carlo solve is prohibitively expensive. Even though the differences between the two were not fully resolved, they found that a single iteration was satisfactory to resolve the non-linear emission source term. This had an added drawback in that there is additional cost to solving the low-order solution along with amplification of Monte Carlo noise associated with the correction between the high-order and low-order problems. This work relied on first order temporal discretization.

Second order temporal schemes are difficult to apply to Monte Carlo calculations because the non-linear relationship of the source terms are costly to determine. However, they can easily be applied to deterministic methods which can fully resolve the non-linear source term relatively quickly, as compared to Monte Carlo. Typically this is done using either a predictor-corrector method or a second-order differencing in time such as Crank-Nicholson. Park et al. suggest that higher order temporal integration schemes could be applied to their quasi-diffusion approach to improve accuracy [5].

1.3 Dissertation Overview

The remainder of this dissertation is organized as follows:

II. In Chapter 2, the radiative transfer and material energy balance equations are introduced and the basic Monte Carlo method is outlined.

III. Chapter 3 describes two different opacity treatments; the Spectral-Line-Based Weighted Sum of gray gases (SLW) model and the Line-By-Line (LBL) model. This section details the development of the models and the different parallel metrics that were used to analyze the models.

IV. In Chapter 4, turbulence radiation interaction (TRI) effects are defined along with different metrics for measuring the effects. This includes the development of a three-dimensional test case similar to the one developed by [4] with the addition of particulate.

V. In Chapter 5, The CMFD scheme is described in the context of a hybrid high-order/low-order radiative transfer scheme. The Crank-Nicholson temporal integration scheme is applied to the diffusion equation in the low-order scheme and the Monte Carlo transport method is used used for the high-order scheme.

VI. Chapter 6 outlines the numerical models used to test the methods which have been described in this work. This chapter also includes the results obtained for these numerical models.

VII. Chapter 7 contains a discussion of the results obtained from the numerical simulations performed for the models. This chapter also highlights the significance of these results and future work that could be investigated.

2 Transport Preliminaries

2.1 Introduction

This chapter presents the radiative transfer equations and the solution approaches used in this work. This includes a detailed outline of the Monte Carlo method as it applies to radiative transfer. This chapter also outlines the development of the diffusion equations and the assumptions associated with them. Finally, this section describes the different temporal and spatial discretizations that will be used in this work.

2.2 Radiative Transfer Preliminaries

The frequency-dependent thermal photon transport equation,

$$\frac{1}{c}\frac{\partial I}{\partial t} + \bar{\Omega} \cdot \bar{\nabla} I = -KI + KB, \tag{1}$$

describes the photon distribution in a physical system. In many problems of interest, the photon distribution is tightly coupled to the material energy balance, which is represented mathematically by,

$$\frac{\partial E^m}{\partial t} = \int_{4\pi} \int_0^\infty d\nu d\bar{\Omega} KI - \int_{4\pi} \int_0^\infty d\nu d\bar{\Omega} KB. \tag{2}$$

where the independent variables have been left out for brevity. In Equations 1 and 2, c denotes the speed of light $[cm/sec]$, and the independent variables for these equations are as follows: $\bar{r}$ is a location in the spatial domain $[cm]$, ν is the photon frequency, $\bar{\Omega}$ is the solid angle of photon travel $[steradians]$. The remaining quantities are, with their appropriate independent variables: the opacity $K(\nu, \bar{r}, t)$

$[1/cm]$, the photon intensity $I(\bar{r}, \nu, \bar{\Omega}, t)$ $[J/(cm^2 * sec * steradian * Hz)]$, the Planck function $B(\nu, T(\bar{r}, t))$, the material energy density $E_m(T(\bar{r}, t))$ $[J/cm^3]$, and the temperature of the background medium $T(\bar{r}, t)$ $[K]$.

The Planck function (or Planckian),

$$B(\nu, T) = \frac{2h}{c^2} \frac{\nu^3}{(e^{\frac{h\nu}{kT}} - 1)}, \tag{3}$$

describes the frequency distribution of the photons being emitted from a material at temperature $T(\bar{r})$. In this function, h is Planck's constant $[J * sec]$ and k is Boltzmann's constant $[J/K]$.

2.3 Monte Carlo Basics

A Monte Carlo method generates a finite number of photon histories that are governed by known probability distributions which describe the system. Consider a frequency independent version of Equations 1 and 2:

$$\frac{1}{c\Delta t}(I_{n+1} - I_n) + \bar{\Omega} \cdot \bar{\nabla} I_{n+1} = -K_n I_{n+1} + K_n a T_n^4, \tag{4}$$

and

$$E_{n+1}^m - E_n^m = \int d\bar{\Omega} K I_{n+1} \Delta t - \int d\bar{\Omega} K B(\nu, T_n) \Delta t \tag{5}$$

where Equations 4 and 5 have been integrated over a single time step Δt using Euler's method, and the material properties have been lagged at the previous time step. The errors in this assumption will be discussed in later chapters.

If N Monte Carlo histories are created, their weight w associated with each history can be defined as

$$w = \frac{1}{N} \left(K_n a T_n^4 + \frac{1}{c\Delta t} I_n \right). \tag{6}$$

Note that $\frac{1}{c\Delta t}$ has the same units as the opacity and, in this case, it is considered as the census opacity. *Census* is the energy that remains in the photon intensity field, rather than being absorbed into the material, at the end of the time step.

In this system, there are two possible interactions; census or absorption. To simulate the various physical processes in the transport of photons, psuedo-random numbers are used to sample from probability density functions $f(x)$[42]. Here, $f(x)dx$ is the probability that x lies between x and $x+dx$, such that $\int_0^\infty f(x)dx = 1$. For example, the probability that a photon will have an interaction between x and $x + dx$ can be written as

$$f(x)dx = e^{-K_t x}dx \tag{7}$$

where $K_t = K + \frac{1}{c\Delta t}$ is the total opacity. The cumulative probability distribution function (CPDF) $F(x)$ represents the probability that the random variable x' takes on a value between 0 and x:

$$F(x) = \int_0^x f(x')dx'. \tag{8}$$

Given the example probability density function in Eq. (7), the CPDF can be expressed as

$$F(x) = 1 - e^{-K_t x}. \tag{9}$$

Because the range of the CPDF will always be between zero and one, it is possible to select a random number, between zero and one to determine the distance x traveled by the particle before a collision[42]. This is done by setting $F(x)$ equal to a random number (ζ) and then solving for x. This would be the collision location in an homogeneous infinite medium where the total opacity is determined from the material properties. Real problems of interest have finite spatial domains with material regions considered to be homogeneous. It is necessary in this case to check

if the randomly selected interaction location exists in the defined geometry. This is accomplished by checking if the Monte Carlo ray intersects any region boundaries at a location to the original location of the particle than the next interaction. If so, the particle is moved to that position on the region boundary a new distance to collision is determined using the material properties of the new cell. This process is simple for one dimensional problems, but becomes increasingly more difficult in complex geometries. In this research, we implement a ray tracing scheme based on spatial cells with an arbitrary number of planar faces. This procedure is outlined below (see Figure 1):

1. Select the next random material interaction location. This results in a vector v from the initial location a to the final location b.

2. Loop over all the faces (f_j) that define cell i which contains the original starting location a. Here, j varies from 1 to $N_{f,i}$ faces.

    - Using simple geometry, it can be determined if vector v crosses the plane p_j which defines face f_j (see plane_intersection subroutine in Appendix A.1). This assumes that the face is always planar.
    - If the vector crosses the plane p_j at point c, it is then determined if the intersection takes place in the area created by its nodes n_k which define the face f_i on the plane. (see facet_area_diff subroutine in Appendix A.1)
    - If the distance to the face intersection ($\sqrt{(c-a)^2}$) is less than the distance to the next material interaction ($\sqrt{(b-a)^2}$), the photon crosses this face. If it is known that the cell is not convex, it can exit the loop at this point. If not, it is necessary to continue iterating through all faces,

and if there are multiple crossing locations the intersection is determined to be at location closest to the original position of the photon.

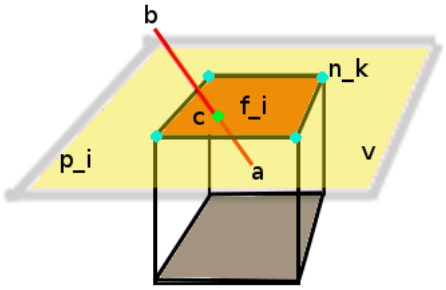

Figure 1: A Monte Carlo ray traveling from point a which intersects plane p_i at location c for face f_i defined by the nodes n_i before reaching point b

After obtaining a collision location within a cell, it is possible to determine the collision type by constructing another probability density function. For this example problem, there are two types of possible interactions; census and absorption. This creates a histogram that can be used to select a collision type using a random number (ζ) between zero and one;

$$k(\zeta) = \begin{pmatrix} census & 0 \leq \zeta \leq \frac{\frac{1}{c\Delta t}}{K_t} \\ absorbed & \frac{\frac{1}{c\Delta t}}{K_t} < \zeta \leq 1 \end{pmatrix}.$$

After selecting the collision type, the weight of the particle is "tallied"; adding the weight to a sum representing interaction events. Tallies are used to estimate the quantities of interest in the problem. It can be shown that for an infinite medium, these tallies approximate the intensity and the energy absorption. From the defined probabilities and Equations 4 and 6, the census tally can be written as;

$$\begin{aligned} \text{Census} &= P_c N w \\ &= \frac{\frac{1}{c\Delta t}}{K_t} N \frac{1}{N} \left(K_n a T_n^4 + \frac{1}{c\Delta t} I^n \right) \\ &= \frac{1}{c\Delta t} I^{n+1}. \end{aligned} \tag{10}$$

Similarly, the absorption tally can be written as;

$$\begin{aligned} \text{Energy absorbed} &= P_a N w \\ &= K I^{n+1}. \end{aligned} \tag{11}$$

2.4 The Diffusion Equation

The diffusion equation can be derived using the zeroth and first angular mo-

ments of the radiative transfer equation. The zeroth moment can be written as;

$$\frac{1}{c}\int_0^{4\pi}\left(\frac{1}{c}\frac{dI}{dt}+\bar{\Omega}\cdot\bar{\nabla}I+KI=KB\right), \tag{12}$$

where the radiative transfer equation was multiplied by $\frac{1}{c}$ to transform the coefficients into a familiar form. The photon energy density $E(\bar{r},\nu,t)$ $[J/cm^3-Hz]$ can be defined as;

$$E=\frac{1}{c}\int_0^{4\pi} I\ d\bar{\Omega}, \tag{13}$$

and the radiative flux $F(\bar{r},\nu,t)$ $[J/sec-cm^2-Hz]$ is defined as;

$$F=\int_0^{4\pi} I\ \bar{\Omega}\ d\bar{\Omega}. \tag{14}$$

We make use of the following identities

$$\int_0^{4\pi} d\bar{\Omega}=4\pi \tag{15}$$

and

$$\int_0^{4\pi} \bar{\Omega}\ d\bar{\Omega}=0. \tag{16}$$

These definitions simplify the majority of the integral terms found in the zeroth angular moment equation,

$$\frac{1}{c}\frac{dE}{dt}+\frac{1}{c}\bar{\Omega}\cdot\bar{\nabla}F+KE=Kb(\nu,T)aT^4, \tag{17}$$

where a is the radiation constant,

$$a=\frac{8\pi^5k^4}{15c^3h^3}, \tag{18}$$

and $b(\nu,T)$ is the normalized Planck function

$$b(\nu,T)=\frac{h}{kT}\frac{15}{\pi^4}\frac{\left(\frac{h\nu}{kT}\right)^3}{(e^{\frac{h\nu}{kT}}-1)}. \tag{19}$$

The zeroth moment of the material energy density equation becomes

$$\frac{1}{c}\int_0^{4\pi}\left(\frac{dE_m}{dt}=\int_0^{\infty}\int_0^{4\pi}d\bar{\Omega}'d\nu KI-\int_0^{\infty}\int_0^{4\pi}d\bar{\Omega}'d\nu KB\right)d\bar{\Omega}, \tag{20}$$

or after some simplification

$$\frac{1}{c}\frac{dE_m}{dt}=\int_0^{\infty}KEd\nu-\int_0^{\infty}Kb(\nu,T)aT^4d\nu. \tag{21}$$

To generate a single partial differential equation for the photon energy density, we need a relationship between F and E. The first moment of the radiative transport equation can be used to generate this relationship:

$$\frac{1}{c}\int_0^{4\pi}\left(\frac{1}{c}\frac{dI}{dt}+\bar{\Omega}\cdot\bar{\nabla}I+KI=KB\right)\bar{\Omega}d\bar{\Omega}. \tag{22}$$

The identities

$$\int_0^{4\pi}\bar{\Omega}\bar{\Omega}d\bar{\Omega}=\frac{4\pi}{3}, \tag{23}$$

and

$$\int_0^{4\pi}\bar{\Omega}\bar{\Omega}\bar{\Omega}d\bar{\Omega}=0, \tag{24}$$

are useful in simplifying Eq. (22), as is the linearly-anisotropic approximation of the intensity:

$$\frac{I}{c}\approx\frac{1}{4\pi}\left(E+\frac{3\bar{\Omega}}{c}F\right). \tag{25}$$

The streaming term in Eq. (22) becomes

$$\frac{1}{c}\int_0^{4\pi}\bar{\nabla}\cdot\bar{\Omega}\bar{\Omega}Id\bar{\Omega}= \tag{26}$$

$$\bar{\nabla}\cdot\frac{E}{4\pi}\int_0^{4\pi}\bar{\Omega}\bar{\Omega}d\bar{\Omega}+\frac{3}{c}\bar{\nabla}\cdot F\int_0^{4\pi}\bar{\Omega}\bar{\Omega}\bar{\Omega}d\bar{\Omega}=$$

$$\frac{1}{3}\bar{\nabla}\cdot E,$$

such that the final form of the first moment of the transport equation is

$$\frac{1}{c}\frac{dF}{dt} + \frac{1}{3}\bar{\nabla} \cdot E + KF = 0 \tag{27}$$

If it is assumed that the time dependence of the radiative flux is negligible, Eq. (27) becomes Fick's Law

$$\frac{1}{c}F = -D\bar{\nabla} \cdot E, \tag{28}$$

where $D(\nu, \bar{r})[cm]$ is the diffusion coefficient defined as $\frac{1}{3K}$.

Using this information, the diffusion equation and the material energy balance equation can be expressed as;

$$\frac{1}{c}\frac{dE}{dt} - \bar{\nabla} \cdot D\bar{\nabla}E + KE = \frac{K}{c}B, \tag{29}$$

and

$$\frac{1}{c}\frac{dE_m}{dt} = \int_0^\infty KEd\nu - \int_0^\infty \frac{K}{c}Bd\bar{\Omega}d\nu. \tag{30}$$

2.5 Discretization

This work uses a Cartesian spatial discretization and an equally spaced temporal discretization for the diffusion equation. A second order Crank-Nicholson scheme is used for the temporal discretization. The spatial discretization uses a second order central differencing discretization scheme.

2.5.1 Crank-Nicholson

A Crank-Nicholson algorithm is used for the temporal discretization of the diffusion equation. The time discretized form of the diffusion equation can be written as;

$$\frac{1}{c}\frac{E_{n+1} - E_n}{\Delta t} - \frac{1}{2}\left(\bar{\nabla} \cdot D\bar{\nabla}E_{n+1} + \bar{\nabla} \cdot D\bar{\nabla}E_n\right)\frac{1}{2}\left(KE_{n+1} + KE_n\right)$$
$$= \frac{K_a}{c}\frac{1}{2}(B^{n+1} + B^n)$$

and

$$\frac{1}{c\Delta t}\left(E_{m_{n+1}} - E_{m_n}\right) = \frac{1}{2}\int_0^\infty (KE_{n+1} + KE_n)d\nu$$
$$-\frac{1}{2}\int_0^\infty \frac{1}{c}(KB^{n+1} + KB^n)d\bar{\Omega}d\nu.$$

2.5.2 Second-Order Central Differencing in Space

The diffusion operator can be written in three-dimensional Cartesian coordinates as;

$$\bar{\nabla}\cdot D\bar{\nabla}E = \frac{d}{dx}D\frac{dE}{dx} + \frac{d}{dy}D\frac{dE}{dy} + \frac{d}{dz}D\frac{dE}{dz} \tag{31}$$

Though the discretization is in three dimensions, it is easiest to show the spatial discretization in one dimension. The other dimensions can be derived similarly. A second-order central differencing scheme is derived by integrating this operator over a finite volume, and applying the Gauss divergence theorem:

$$\int_V \frac{d}{ds}D\frac{dE}{ds}dV = \frac{A_{i+\frac{1}{2}}D_{i+\frac{1}{2}}}{\Delta s_{i+\frac{1}{2}}}\left(E_{i+1} - E_i\right) - \frac{A_{i-\frac{1}{2}}D_{i-\frac{1}{2}}}{\Delta s_{i-\frac{1}{2}}}\left(E_i - E_{i-1}\right) \tag{32}$$

where i, $i-1$, and $i+1$ denote the center cell and its neighbors, respectively. The remaining subscripts indicate variables ($i-\frac{1}{2}$ and $i+\frac{1}{2}$) located on the face that bound the cell. The variable A denotes the cell face area with a normal in the s direction.

2.5.3 Boundary Conditions

An albedo boundary condition will be sufficient for all the test cases that will be used in this work. We approach boundary conditions through the definition values of the dependent variable in *ghost cells*, cells outside the physical problem adjacent to the boundary surface. An albedo boundary condition specifies that the partial flux entering the problem through the boundary face (F_{bf}^-) is some fraction (α) of

the partial flux exiting the boundary face (F_{bf}^{+}).

$$F_{bf} = F_{bf}^{+} - F_{bf}^{-} = -F_{bf}^{-}(1-\alpha) \tag{33}$$

Using the P_1 approximation for the partial flux, the total flux can be written as;

$$F_{bf} = -\left(\frac{1}{4}E_{bf} - \frac{1}{2}F_{bf}\right)(1-\alpha). \tag{34}$$

Using Fick's Law, it is possible to express the total flux in terms of the cell-center energy density E_i, and the ghost cell energy density E_g

$$F_{bf} = -2D\frac{(E_i - E_g)}{\Delta s}. \tag{35}$$

Combining these equations yields a new expression for the total flux at the boundary face;

$$F_{bf} = -\frac{\frac{2D}{\Delta s_{bf}}\frac{(1-\alpha)}{(1+\alpha)}E_i}{\frac{(1-\alpha)}{(1+\alpha)} + \frac{4D}{\Delta s_{bf}}}. \tag{36}$$

From the equations above, the albedo boundary condition dictates that

$$-\frac{\frac{2A_{bf}D_{bf}}{\Delta s_{bf}}\frac{(1-\alpha)}{(1+\alpha)}E_i}{\frac{(1-\alpha)}{(1+\alpha)} + \frac{4D}{\Delta s_{bf}}} = 0. \tag{37}$$

The discretized equation for a cell adjacent to a boundary will be of the form

$$-\frac{A_{bf}D_{bf}}{\Delta s_{bf}}(E_i - E_g) + a_g E_g + a_n E_i - b_g = 0, \tag{38}$$

which means that the appropriate values for the ghost coefficients become

$$a_g = -\frac{A_{bf}D_{bf}}{\Delta s_{bf}}$$

$$b_g = 0$$

$$a_n = -\frac{\frac{2A_{bf}D_{bf}}{\Delta s_{bf}}\frac{(1-\alpha)}{(1+\alpha)}}{\frac{(1-\alpha)}{(1+\alpha)} + \frac{4D}{\Delta s_{bf}}} + \frac{A_{bf}D_{bf}}{\Delta s_{bf}}$$

3 Gas Models

3.1 Introduction

This chapter outlines the development of the opacity data and the two different opacity models used in this work: Line-by-Line (LBL) and Spectral-Line-Based Weighted Sum of gray gases (SLW). This chapter also includes the definition of the different parallel metrics that are used to compare the parallel efficiencies of these two models.

3.2 LBL Model and the Opacity Database

The LBL model development was based on the work performed by Wang and Modest [3]. The LBL gas model is, to date, the most accurate and robust gas model available. It directly interprets opacities, given the photon frequency, from either the line-by-line data or high resolution opacity functions generated from line-by-line data. This method typically employs the information obtained from line-by-line databases such as HITRAN and HITEMP. These databases provide individual line intensities, at a designated temperature and pressure, with their associated line broadening coefficients. The opacity (or absorption coefficient) can be constructed using the following equation [13]:

$$\sigma(\eta) = \sum_i \frac{S_i}{\pi} \frac{\gamma_i}{(\eta - \eta_i)^2 + \gamma_i^2} \tag{39}$$

where $\sigma(\eta)$ is the opacity at wave number η, η_i is the wave number of line i, and γ_i is the half-width-half-max of line i. The line half-width-half-max is defined as half the width at half the maximum absorption coefficient of the line [1]. The shape of these lines is greatly affected by two different types of line broadening; collision broadening and Doppler broadening. Collision broadening is attributed

to the frequency of collisions between molecules. Two parameters affect how often gas molecules collide: temperature - as the temperature of the gas increases the number of molecular collisions increases, and pressure - as the pressure increases the number of molecular collisions increases.

A code was developed to create binary files for the opacity data tables from either the HITRAN or HITEMP databases. This code can take any number of materials and construct a database that spans any range of material state variations requested. This includes variations in temperature, pressure, and partial pressure. A three-dimensional table is created that can be linearly interpolated for material states between evaluated opacities in the database. The code is also capable of producing mock opacity tables in an identical format to be read by the transport code.

The opacity tables were created in a manner similar to the previous work of Wang et al. [3] in which the opacity of each species and its probability of black body emission are stored for every wavenumber at the designated pressure and temperature. The cumulative emissivity is stored along with the opacity for every wavenumber. This is then used to construct the cumulative probability of emission (P_η) from 0 to a particular wavenumber (η)

$$P_\eta = \frac{\int_0^\eta \sigma(\eta)B(\eta,T)d\eta}{\int_0^\infty \sigma(\eta)B(\eta,T)d\eta} = \frac{\int_0^\eta \sigma(\eta)B(\eta,T)d\eta}{\sigma_p(T)} \tag{40}$$

where $\sigma(\eta)$ is the absorption opacity of the medium for wavenumber η, T is the temperature of the medium, $\sigma_p(T)$ is the Planck opacity of the medium at temperature T, and $B(\eta,T)$ is the Planck function at the wavenumber previously defined (in terms of frequency) in Equation 3. The Planck opacity would also be stored for every species at its designated pressure and temperature.

It is important to implement a very efficient table look-up algorithm for this

method. We have used a binomial search routine [3], to determine emission frequencies and linear interpolations between temperature, pressure, partial pressure, and wavenumber from a designated opacity database. The binomial search subroutine was found to take on the order of 20-25 iterations to converge to a discrete frequency range for 1.5 million opacity data points.

3.3 SLW model

In the SLW model, a quadrature of gray gases with associated weights is generated that represent the opacity distribution as a function of average opacities integrated over the entire frequency range [1]. This has been shown to be a coarse version of the full spectrum K-distribution method [1]. The full spectrum K-distribution reorganizes the opacity shape into a smooth function varying from the smallest opacity to the largest. For a purely homogeneous material with an infinite number of K groups (or gray gases), it will produce the exact answer. Reorganizing the opacity such that it is a smooth function makes it easy easier to sample, but it also masks the frequency dependence of the material. In the presence of strong heterogeneities this can produce significant errors.

The K-distribution equation is an outgrowth of the transformation of the intensity $I_\nu(\bar{r}, \nu, \bar{\Omega}, t)$ from a function of frequency to a function of opacity $I_K(\bar{r}, K, \bar{\Omega}, t)$. This is accomplished by multiplying the transport equation (Eq. 1) by $\delta(K' - K(\nu, \Theta_0))$ and integrating over the frequency variable ν. Here K' denotes some opacity value in the range $0 \leq K' \leq \infty$, and Θ_0 is some reference material state, generally consisting of volume averaged quantities, which is used to evaluate the opacity. The material state includes the material total pressure, partial pressure, and temperature. This operation is straightforward for a homogeneous case in that

the reference state, which is used to evaluate the opacity delta function, is equal to the true opacity for the material. This allows the opacity value to be removed from under the integral anywhere that it is encountered in the transport equation, because it would be evaluated as zero anywhere that $K' \neq K(\nu, \Theta_0))$. This implies that the K-distribution method would be exact in a truly homogeneous case. However, most cases of interest are not homogeneous. Therefore, it is necessary to make one of two assumptions in heterogeneous problems: 1) the individual opacity values are correlated between the true material state and the reference state or 2) they can be evaluated via a simple scaling relationship. These are known as the "Correlated-K" and "Scaled-K" distribution models [1]. In this research, we have chosen the "Correlated-K" distribution model. The correlation assumption can be mathematically represented as

$$\begin{aligned} g(T, \Theta, K_g) &= \int_0^{K_g} \frac{\int_0^\infty B(\nu, T)\delta(K' - K(\nu, \Theta))d\nu}{\int_0^\infty B(\nu, T)d\nu} dK' \\ &\approx \int_0^{K_0} \frac{\int_0^\infty B(\nu, T)\delta(K' - K(\nu, \Theta_0))d\nu}{\int_0^\infty B(\nu, T)d\nu} dK' \\ &= g(T, \Theta_0, K_0). \end{aligned}$$

Here $g(T, \Theta, K_g)$ is the cumulative K-distribution. This states that the two different opacity values (K_g and K_0) are correlated such that they are associated with the same frequencies. It is useful at this point to define the K-distribution ($f(T, \Theta, K')$) and K-intensity ($I_K(\bar{r}, K, \Theta, \bar{\Omega}, t)$):

$$f(T, \Theta, K') = \frac{\int_0^\infty B(\nu, T)\delta(K' - K(\nu, \Theta))d\nu}{\int_0^\infty B(\nu, T)d\nu}, \tag{41}$$

and

$$I_{K'_0} = I_{K(K', \Theta_0)} = \int_1^\infty I\delta(K' - K(\nu, \Theta_0))d\nu. \tag{42}$$

The multiplication of a delta function which uses a reference state opacity ($K(\nu,\Theta_0)$) that is different than the opacity it is being multiplied by ($K(\nu,\Theta)$) creates a new opacity value,

$$K(\Theta,\Theta_0,K') = \int_0^\infty K(\nu,\Theta)\delta(K' - K(\nu,\Theta_0))d\nu \tag{43}$$

that is dependent of its current material state(Θ), the reference material state(Θ_0), and the reference opacity of interest(K'). Applying the correlation assumption to the absorption term and integrating over frequency yields:

$$\begin{aligned} & \int_0^\infty K(\nu,\Theta)I\delta(K' - K(\nu,\Theta_0))d\nu \\ \approx \quad & K(\Theta,\Theta_0,K')\int_0^\infty I\delta(K' - K(\nu,\Theta_0))d\nu = K(\Theta,\Theta_0,K')I_{K'_0} \end{aligned} \tag{44}$$

Applying the same assumption to the emission term results in

$$\begin{aligned} & \int_0^\infty K(\nu,\Theta)B(\nu,T)\delta(K' - K(\nu,\Theta_0))d\nu \\ = \quad & \frac{\int_0^\infty B(\nu,T)d\nu\int_0^\infty K(\nu,\Theta)B(\nu,T)\delta(K' - K(\nu,\Theta_0))d\nu}{\int_0^\infty B(\nu,T)d\nu} \\ \approx \quad & K(\Theta,\Theta_0,K')\int_0^\infty B(\nu,T)d\nu f(T,\Theta_0,K') \end{aligned} \tag{45}$$

The heterogeneous radiative transfer equation can now be written as in terms of the K-distribution function as, assuming coherent scattering;

$$\begin{aligned} & \frac{1}{c}\frac{\partial I_{K'_0}}{\partial t} + \bar{\Omega}\cdot\bar{\nabla}I_{K'_0} + K(\Theta,K')I_{K'_0} \\ = \quad & K(\Theta,\Theta_0,K'))\int_0^\infty B(\nu,T)d\nu f(T,\Theta_0,K') \end{aligned} \tag{46}$$

The total frequency integrated intensity $I(\bar{r},\bar{\Omega},t)$ can now be evaluated as;

$$I = \int_0^\infty I_\nu d\nu = \int_0^\infty I_K dK \tag{47}$$

The K-distribution equations derived above are continuous in opacity. The SLW model simply creates a group structure in opacity space rather than treating the K-distribution directly as a continuous function. This is done using a change of variable for the integration of the opacity value. The derivative of the cumulative K-distribution function with respect to opacity is the original K-distribution function.

$$\frac{\partial g(T_0, \Theta_0, K_0)}{\partial K} = f(T_0, \Theta_0, K') \rightarrow \partial K = \frac{\partial g(T_0, \Theta_0, K_0)}{f(T_0, \Theta_0, K')} \tag{48}$$

This substitution creates an integral over the cumulative K-distribution function with the bounds $0 \leq K_g \leq 1$.

$$I = \int_0^\infty I_K dK = \int_0^1 I_K \frac{\partial g(T_0, \Theta_0, K_0)}{f(T_0, \Theta_0, K')} = \int_0^1 I_g \partial g(T_0, \Theta_0, K_0) \tag{49}$$

This integral can then be broken into a group summation of discreet integrations over cumulative K-distribution space such that the frequency integrated intensity is defined as;

$$I = \int_0^1 I_g \partial g(T_0, \Theta_0, K_0) = \sum_{i=0}^{N} \int_{g(T_0, \Theta_0, K_0^{i-1})}^{g(T_0, \Theta_0, K_0^i)} I_g \partial g(T_0, \Theta_0, K_0) = \sum_{i=0}^{N} I_i \tag{50}$$

One final approximation must be made to transform the cumulative K-distribution integrated transport equation into the SLW equations. That assumption is that the opacity $K(\Theta, \Theta_0, K')$ over cumulative K-distribution integration range can be represented with some mean value $\tilde{K}_i(\Theta, \Theta_0, T_0)$ that can be treated as a constant over the individual integration range;

$$\tilde{K}_i(\Theta, \Theta_0, T_0) = \frac{\int_{g(T_0, \Theta_0, K_0^{i-1})}^{g(T_0, \Theta_0, K_0^i)} K(\Theta, \Theta_0, K_0) B(\nu, T_0) \partial g(T_0, \Theta, K_0)}{\int_{g(T_0, \Theta, K_0^{i-1})}^{g(T_0, \Theta_0, K_0^i)} B(\nu, T_0) \partial g(T_0, \Theta, K_0)} \tag{51}$$

Using this assumption, the cumulative K-distribution integration of the emission

term can be simplified such that;

$$\int_0^\infty B(\nu,T)d\nu \int_{g(T_0,\Theta_0,K_0^{i-1})}^{g(T_0,\Theta_0,K_0^i)} K(\Theta,\Theta_0,K_0) f(T,\Theta_0,K') \partial g(T_0,\Theta_0,K_0)$$

$$= \tilde{K}_i(\Theta,\Theta_0,T_0) \int_0^\infty B(\nu,T)d\nu \int_{g(T_0,\Theta_0,K_0^{i-1})}^{g(T_0,\Theta_0,K_0^i)} \partial g(T,\Theta_0,K_0) \tag{52}$$

The final SLW equation can be written as;

$$\frac{1}{c}\frac{dI_i}{dt} + \bar{\Omega}\cdot\bar{\nabla} I_i + \tilde{K}_i(\Theta,\Theta_0,T_0) I_i$$

$$= \tilde{K}_i(\Theta,\Theta_0,T_0) \int_0^\infty B(\nu,T)d\nu \int_{g(T_0,\Theta_0,K_0^{i-1})}^{g(T_0,\Theta_0,K_0^i)} \partial g(T,\Theta_0,K_0) \tag{53}$$

The primary cost associated with the SLW model is the development of the cumulative K-distribution function($g(T,\Theta_0,K)$) and the gray gas mean opacity values ($\tilde{K}_i(\Theta,\Theta_0,T_0)$). It is well documented that this approach can be inaccurate for some heterogeneous materials [1]. The reference Planckian temperature and the reference material state are determined using volume-averaged quantities, as described by Modest [1]. These reference states are used to develop correlations (Eq. 52) between the frequency dependence of opacities for different material states. Even though a single reference material state is used for the entire problem, it is still necessary to determine the Planck-function-weighted K-distribution in each cell for different temperatures.

3.4 Parallel Metrics

Parallel metrics quantify the increase or decrease in computational efficiency as a function of the number of processors used to generate the solution. This section discuses the different scaling types used in this work and the information that can potentially be evaluated from them. This work only considers message passing parallelism and simple, volume-based domain decomposition.

3.4.1 Scaling

The strong scaling benchmark measures the scaling of a numerical model as the total problem domain is subdivided onto processors. Strong scaling is defined as;

$$\xi_s(N) = N\frac{t_N}{t_1}100, \tag{54}$$

where $\xi_s(N)$ is the strong scaling efficiency for N processors, t_N is the total calculation time for the solution with N processors, and t_1 is the calculation time for a serial (single processor) solution to the problem.

Weak scaling benchmarks determine the scaling of numerical model as the total problem domain is increased along with the number of processors used to solve the problem. This information provides insight as to how a larger problem will perform with a proportional increase in the number of processors. Weak scaling is defined as;

$$\xi_w(N) = \frac{t_1}{t_N}100 \tag{55}$$

where $\xi_w(N)$ is the weak scaling efficiency for N processors.

History scaling is not a typical parallel benchmark, but it is applicable when a problem is solved via Monte Carlo. In a Monte Carlo simulation, energy packets (or "Monte Carlo histories"), are tracked through a problem based on physical interaction probabilities. The number of histories used to resolve the solution directly correlates with the variance in the solution. Therefore, it is important to understand how the average calculation time per history will scale as the number of histories used to resolve the solution is increased. The average computation time per history (t_p) can be defined as;

$$t_p(N_{mc}) = \frac{t}{N_{mc}} \tag{56}$$

Where t is the total computation time and N_{mc} is the total number of Monte Carlo histories used to resolve the solution.

3.4.2 Load Imbalance

Load imbalance can significantly effect the solution times of parallel computations [43]. Therefore, it is necessary to quantify the sensitivity different solution algorithms are to load balancing issues. Load balance is defined as the ratio of total processor compute time to total run time. In a perfectly balanced system, there is zero idle processor time and the load would be 100% balanced. We use the average deviation in the load to represent the load imbalance, rather than the load balance described previously. The effective load imbalance is indicated by deviations in the average CPU time defined by:

$$t_{std}[\%] = \frac{\sqrt{\frac{1}{N}\sum_{i=1}^{N}(t_i)^2 - \left(\frac{1}{N}\sum_{i=1}^{N} t_i\right)^2}}{\frac{1}{N}\sum_{i=1}^{N} t_i} \times 100, \tag{57}$$

where $t_{std}[\%]$ is the percent deviation from the average cpu time, t_i is the cpu time for processor i, and N is the number of processors. The average deviation in a perfectly balanced system would be zero.

4 Turbulence Radiation Interactions in Particulate-Laden Flow

4.1 Introduction

This chapter derives the time averaged form of the transport equation and how particulate radiation interactions are accounted for. This includes discussions on how particulate can either be tracked geometrically through the system or can be accounted for statistically using the chord length method. This chapter also outlines the metrics that are used in this work to measure turbulent radiation interaction effects.

4.2 Governing Equations

Modeling a combustion system requires the solution of a set coupled non-linear, partial differential equations. These equations include; the continuity equation, the compressible/incompressible Navier-Stokes equations, mixture fraction equations, the radiative transfer equation, and the energy equation. Each of these equations presents its own difficulties; the significant difference in time scales makes these problems very difficult to solve efficiently and accurately.

The continuity equation (or conservation of mass) can be written as;

$$\frac{d\rho}{dt} + \bar{\nabla} \cdot \rho \bar{U} = 0, \tag{58}$$

and the compressible Navier-Stokes equations can be written as;

$$\rho \left(\frac{d\bar{U}}{dt} + \bar{U} \cdot \bar{\nabla} \bar{U} \right) = -\bar{\nabla} p + \bar{\nabla} \cdot \mu \bar{\nabla} \bar{U} + f. \tag{59}$$

Independent variables have been left out for brevity. Here $\rho(\bar{r}, t)$ $[cm^3/sec]$ is the material density, $U(\bar{r}, \bar{\Omega}, t)$ $[cm/s]$ is the fluid flow velocity, $p(\bar{r}, t)$ is the pressure,

τ is the stress tensor, and f represents the body forces. The energy equation can be written as;

$$\rho C_p \left(\frac{dT}{dt} + \bar{U} \cdot \bar{\nabla} T \right) = \bar{\nabla} \cdot k \bar{\nabla} T - \frac{dq_R}{dt} + \dot{Q}_{ch}^{'''} \tag{60}$$

The radiative transfer equation can be written as;

$$\frac{1}{c}\frac{dI}{dt} + \bar{\Omega} \cdot \bar{\nabla} I + KI = \frac{K}{4\pi} B \tag{61}$$

The material energy balance equation is written as

$$\frac{dq_R}{dt} = \int_0^{\infty} \int_0^{4\pi} K_a I d\bar{\Omega} d\nu - \int_0^{\infty} \int_0^{4\pi} \frac{K_a}{4\pi} B d\bar{\Omega} d\nu, \tag{62}$$

where q_R is the material energy density. The mixture fraction equation can be written as;

$$\rho \left(\frac{dY_i}{dt} + \bar{U} \cdot \bar{\nabla} Y_i \right) = \bar{\nabla} \cdot \rho D \bar{\nabla} Y_i + \dot{m}_i^{'''} \tag{63}$$

The mass source ($\dot{m}_i^{'''}$) and the heat source ($\dot{Q}_c^{'''} h$) are products of the chemical reaction;

$$O + F \rightarrow P + Q. \tag{64}$$

In this reaction O, F, and P denote the concentration of oxidizer, fuel, and the resulting product P. The variable Q represents the amount of energy created during the reaction.

4.3 Particulate

The inclusion of particulate in the system requires the addition of a model to account for fluid-particulate interactions. In this research, we use the discrete element model (DEM) [36] to account for these two-way interactions. An important parameter to classify the state of the particulate-laden flow is the Stokes number.

The Stokes number is a ratio of the particulate response time(τ_p) to the Kolmogorov time scale(τ_η) [44];

$$St = \frac{\tau_p}{\tau_\eta} = \frac{1}{18}\left(\frac{\rho_p}{\rho}\right)\left(\frac{d_p}{\eta}\right)^2 \tag{65}$$

The variables ρ and ρ_p are the fluid and particulate density, respectively. The remaining variables are the particulate diameter d_p and Kolmogorov length scale η. It is known that when $St \approx 1$ "preferential concentrations" occur. This is when the local vorticity is strong enough to force particulate out of fluid regions causing particulate clustering [44]. This is important to radiative transfer because it affects particle dispersal and the chord length method, which makes assumptions about the distribution of particulate in background media.

It is also necessary to account for particulate-radiation interactions. Particulate-radiation interactions can either be accounted for using Mei theory or geometric optics, depending on the particulate size parameter and optical thickness. Our focus is on larger coal particulate, where geometric optics is valid. All particulate in this work is considered to be perfect spheres.

4.4 Particulate Radiation Interactions

The complex index of refraction can be expressed as;

$$c = n + ki \tag{66}$$

where $n = c_0/c$ is the refraction index which describes the ratio of the speed of light in a vacuum (c_0) to the speed of light in the medium (c). Photons moving from one material to another with a different refraction index will cause a refraction event. A refraction event is a change in the polar angle of the photon and can be described by Snell's law [1]. In Equation 66, the variable k represents the absorptivity index

and dictates how rapidly a photon traversing a medium will be absorbed. The absorption opacity can be calculated from the absorptivity index as [1].

$$K = \frac{4\pi k\nu}{c_0}. \tag{67}$$

The interaction of radiation with particulate is very sensitive to the size, shape, and material composition of the particulate. For large particulate, diffraction can be neglected allowing for the evaluation of particulate interactions using geometric optics [1]. Large particulate is quantified as $x >> 1$, where x is the non-dimensional size parameter defined by;

$$x = \frac{\pi D_p}{\lambda} > 2, \tag{68}$$

and D_p is the diameter of the particulate and λ is the photon wavelength. If $x \approx 1$ then diffraction can no longer be neglected and Mie theory is applied to determine interaction probabilities.

There are four different particulate-radiation interactions that must be considered: reflection, refraction, diffraction, and absorption. For large thick particulate, diffraction and refraction can be neglected because for large particles diffraction generally scatters in the forward direction [1]. For smaller particulate, however, diffraction can become more isotropic and must be modeled [1]. Diffraction is generally modeled using Mie theory [1]. If the particulate is reasonably optically thick ($xk >> 1$) and all photons that enter the particulate are assumed to be absorbed, their refraction events can be neglected. However, for optically thin or relatively small particulate, this assumption cannot be made because photons will travel though the particulate without being absorbed.

For geometric optics, the probability of a ray intersecting a particulate can be evaluated one of two ways; stochastically or geometrically using direct tracking.

Stochastic methods include atomic mixing and the chord length method [45]. Direct tracking simply includes the particulate either directly in the mesh or on a submesh which is overlaid on the cell mesh. Any of these approaches can be easily incorporated into the Monte Carlo method which is used in this work.

4.4.1 Geometric Optics

Geometric optics was implemented in the following fashion: particulate is tracked on a submesh which is overlaid on the cell mesh. This list of particulates contains their sizes, locations, and material properties. The easiest way to check for Monte Carlo ray intersections with particulate is to iterate through the particulate list for the entire problem during every surface interaction check. However, this can be very expensive for even trivial packing fractions. As a result, we employ a cell-wise linked-list of particulate that can be precomputed at the beginning of the time step and then used on a cell-wise basis to check for particulate surface interactions. The geometric optics process, illustrated in Figures 2 and 3), begins by choosing a random interaction location using Equation 9, where the material opacity K is determined according to the current Monte Carlo particle frequency and the material composition at the current particle location. After a random interaction location is chose all faces in the current cell are looped over to check if the particle remains in the cell. This includes the faces which compose the current cell and the faces of any particulate which has mass that resides in the domain of the cell. The equation for a point on a sphere can be defined by

$$(p - c) \cdot (p - c) = r^2 \tag{69}$$

where p is some location of the sphere and c is the center point of the sphere. A point p on a ray some length l from the starting location p_0 in the direction of the

ray d can be defined as;

$$p = p_0 + ld \tag{70}$$

putting these equations together yields a second order polynomial.

$$(d \cdot d)l^2 + 2(p_0 - c) \cdot dl + (p_0 - c) \cdot (p_0 - c) = r^2 \tag{71}$$

The roots l of this polynomial, as determined by the quadratic formula are

$$l = \frac{-B \pm \sqrt{B^2 + 4AC}}{2A}, \tag{72}$$

where

$$A = d \cdot d, \tag{73}$$

$$B = 2(p_0 - c) \cdot d, \tag{74}$$

$$C = (p_0 - c) \cdot (p_0 - c), \tag{75}$$

These roots represent the distance to the two intersections that any ray should have with the sphere. If the determinant is negative ($B^2 + 4AC < 0$) there is no interaction with the sphere. If the photon is inside the sphere, the intersection occurs at the closest positive root. If the particle is inside the particulate the exit location occurs at the only positive root. If there are no positive roots, there is no intersection with the sphere.

If a Monte Carlo photon crosses a face which separates materials with different complex indices of refraction, it is necessary to account for reflection and refraction events at that surface. The probability of reflecting off of a surface as compared to being refracted into it can be determined from generalized Snell's Law [1];

$$p^2 = \frac{1}{2}\sqrt{(n_2^2 - k_2^2 - n_1^2 \sin^2(\theta_1))^2 + 4n_2^2k_2^2} + (n_2^2 - k_2^2 - n_1^2 \sin^2(\theta_1)) \tag{76}$$

$$q^2 = \frac{1}{2}\sqrt{(n_2^2 - k_2^2 - n_1^2 \sin^2(\theta_1))^2 + 4n_2^2k_2^2} - (n_2^2 - k_2^2 - n_1^2 \sin^2(\theta_1)) \tag{77}$$

$$\rho_{\parallel} = \frac{(p - n_1 \sin(\theta_1)\tan(\theta_1))^2 + q^2}{(p + n_1 \sin(\theta_1)\tan(\theta_1))^2 + q^2}\rho_{\perp} \tag{78}$$

$$\rho_{\perp} = \frac{(n_1 * \cos(\theta_1) - p)^2 + q^2}{(n_1 \cos(\theta_1) + p)^2 + q^2} \tag{79}$$

If Monte Carlo histories are not tracked completely through the particulate, it is necessary to assure that the particulate is sufficiently optically thick. In our approach, we fully track particles through the particulate to increase the range of particulate sizes for which our simulation tool is applicable.

4.5 Chord Length Method

The chord length method accounts for photon-particulate surface interactions using the same interaction physics described in Section 4.4.1. However, particulate surface interaction distances are determined with a stochastic approach. This is done by creating chord length probability distribution functions, where a chord length is the distance a ray travels before interacting with a new material. To implement this approach, we must calculate two different chord length probability distribution functions; one pertaining to the chord lengths through the background material and one pertaining to the chord lengths traveled in the particulate contained in the background material.

It has been shown by Olson et al. [32] that the chord length distribution in the background material of a binary stochastic mixture is truly exponential and Torquato et al. [46] derived the distribution for solid non-overlapping spheres;

$$p_b(z) = \frac{\pi\rho_n \langle R^2 \rangle}{1 - \eta} \exp\left(\frac{-\pi\rho_n z \langle R^2 \rangle}{1 - \eta}\right) \tag{80}$$

where $p_b(z)$ is the probability of a ray traveling a distance z in the background before interacting with a sphere, $\langle R^2 \rangle$ is the mean square of the particulate radii that are in the volume (for constant radii, this is simply the square of the radius),

ρ_n is the number density of the spheres, and η is the volume fraction of the spheres. The cumulative probability density function can then be evaluated by integrating this equation from zero to some chord length l. Given this CPDF, it is possible to select a random chord length through the material using a random number $0 \leq \xi \leq 1$;

$$l = -\log(\xi)\frac{(1-\eta)}{\pi\rho_n \langle R^2 \rangle} \tag{81}$$

It has also been shown that the chord length probability distribution for the distance traveled within the particulate is never exponential. Rather, these distributions are greatly dependent upon the distribution of particulate radii in the material volume. Olson et al. [32] have shown that for a constant particulate radii distribution, the chord length probability distribution will have the form;

$$p_p(z) = \frac{z}{2R^2} \tag{82}$$

where $p_p(z)$ is the probability of a ray traveling some distance z through the particulate before exiting. Integrating this equation from zero to some chord length l results in a cumulative probability distribution for the chord lengths through the particulate. This CPDF can then be used to select a random chord length through the particulate using a random number $0 \leq \xi \leq 1$;

$$l = \sqrt{(4R^2\xi)} \tag{83}$$

Upon entering a particulate, a new distance to material collision is selected. If the chord length through the material is greater than this collision distance, a collision event in the particulate occurs. Otherwise, the Monte Carlo particle exits the particulate.

This makes the selection of chord lengths very straightforward for particulate materials with identical complex indices of refraction. It is more complicated,

however, when it is necessary to account for refractions and reflections. In this situation, a random collision location is chosen for a Monte Carlo photon that starts in the background material using Equation 9. Then, a random chord length is selected for the background material using Equation 81. If the chord length is less than the distance to the next interaction location, then a photon-particulate interaction occurs. For this interaction, it is necessary to randomly select a sphere normal to given the current chord length with the particulate radius. For a distribution of particulate radii, the selection of the random normal becomes increasingly more complicated because of the coupling between the sphere radius and the chord length selection. Our algorithm considers only particulate with constant radii. In this case, it is simple to calculate the angle of intersection for the ray and the surface normal given the chord length. Consder a ray passing through a projection of a sphere (i.e. a circle). The chord length traveled through the material will be directly correlated to the radius on the projection that the ray will pass through. This determines the polar angle between the normal and the ray intersecting with the sphere. The azimuthal angle, however, must be randomly sampled because there is an equal probability that the ray passed through any point on the radius of the projected circle determined from the chord length. A triangle can be constructed using half the chord length l and the particulate radius R in which the cosine of the intersection angle θ as compared to the normal is determined from

$$\cos(\theta) = \frac{l}{2R}. \tag{84}$$

Given that the polar angle is known and that the azimuthal angle can be any random angle defined by $0 \leq \phi \leq 2\pi$, it is possible to generate a random normal that can be used to calculate any refraction event that might occur at the particulate face. Given the incident direction and the newly formed random sphere normal, it

is possible to determine either a refraction or reflection event from the generalized Snell's law, (Equation 76 through Equation 79). If a refraction event occurs, it is possible to determine the true refracted chord length traveled through the sphere and the change in the ray direction given the refraction angel θ_r determined from Snells law and the randomly selected sphere normal. Given that, for a perfect sphere, the incident angle between the entrance normal and the exit normal is identical we can then determine the refracted chord length l_r

$$l_r = 2R\cos(\theta_r), \tag{85}$$

and the exit normal. The polar angle between the exit and entrance normal, θ_n, can be determined from the refraction angle as $\theta_n = \pi - 2\theta_r$. The particle is then moved to the next exit location and Snell's law is again applied. This procedure is continuously iterated until the photon either exits the particulate or a material interaction occurs.

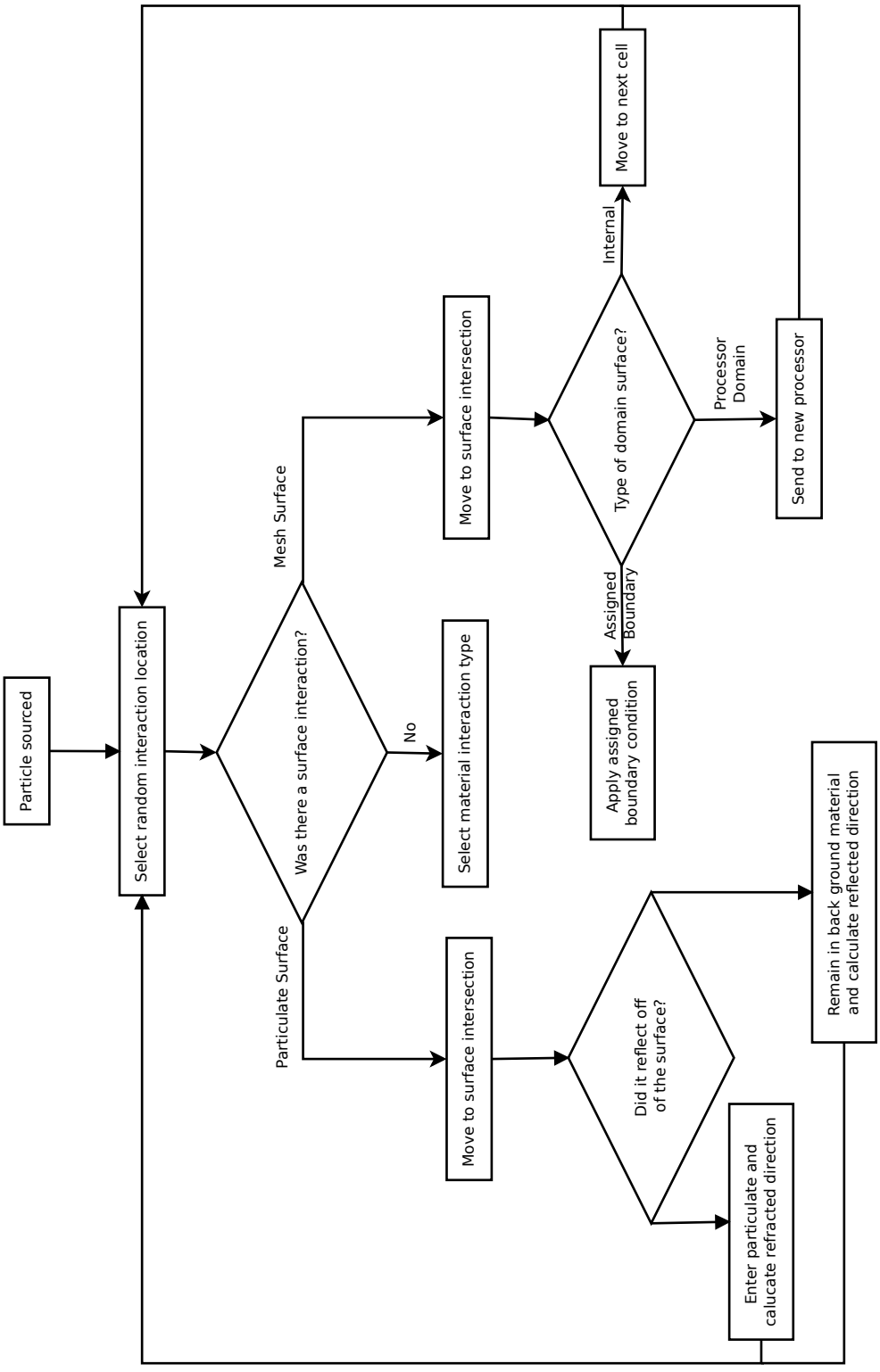

Figure 2: Flow chart showing the Monte Carlo procedure for geometric tracking

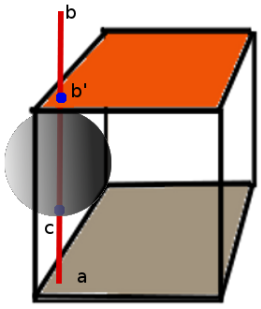

Figure 3: The intersection of a Monte Carlo particle with a plane

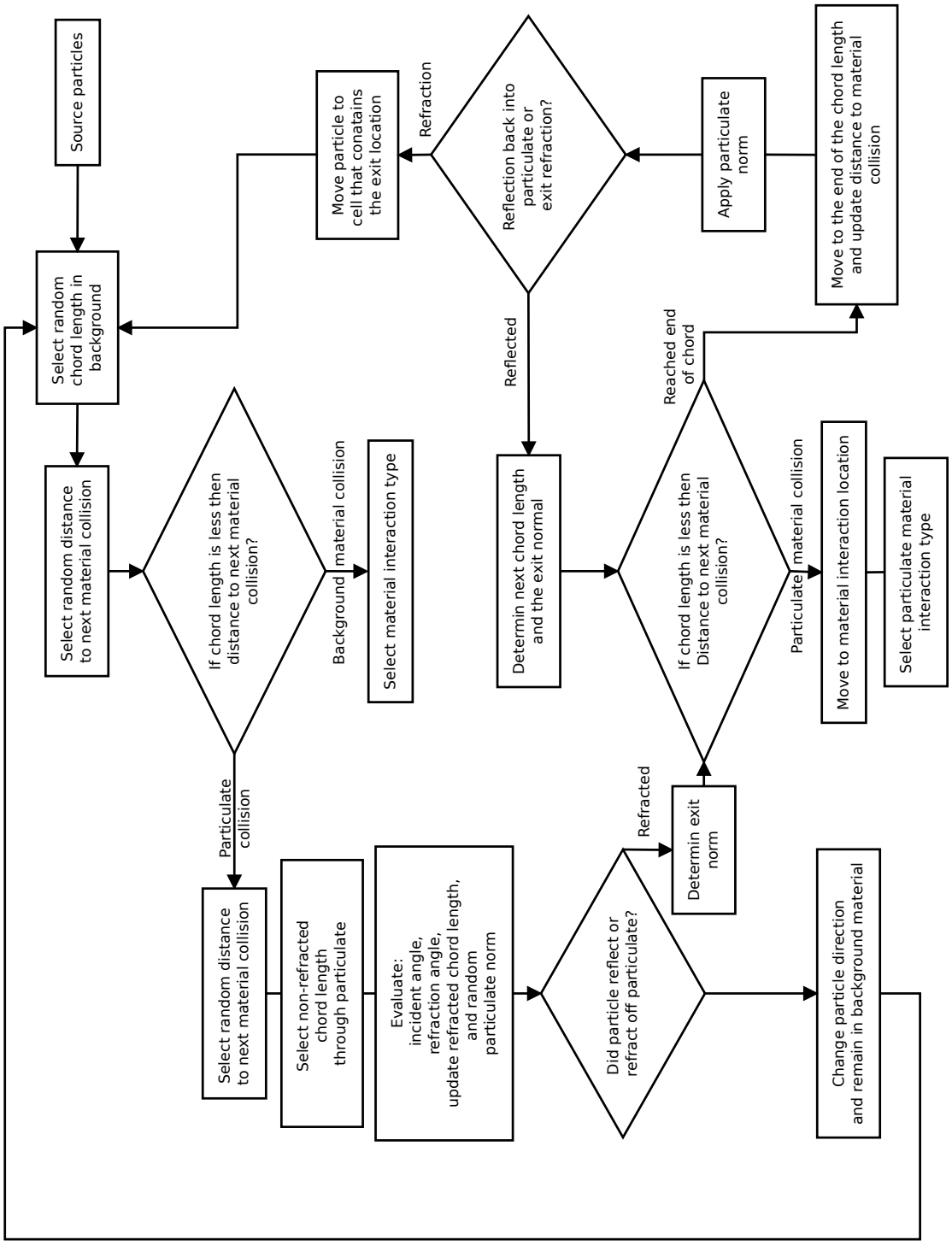

Figure 4: Flow chart showing the Monte Carlo procedure for the chord length method

Tallies are cell-based, rather than particulate-based, as in geometric optics. This requires an added assumption in the equation of state (Eq. 2): the energy determined from the particulate absorption tallies is distributed according to volume fractions;

$$E_p^a = E_c^a \frac{V_p}{\sum_{p=1}^{N_p} V_p}, \tag{86}$$

where E_p^a is the energy absorbed in particulate p, E_c^a is the energy absorbed by all particulate in the cell (or the cell-based particulate absorption tally), V_p is the volume of particulate p, and N_p is the total number of particulate. Similar assumptions are made for the particulate census tallies.

4.6 Turbulence Radiation Interactions

The significant difference in time scales for the radiative transfer equation and the turbulent flow equation can create a unique numerical phenomenon known as Turbulence Radiation Interactions (TRI). The time scale of the flow equations is on the order of the speed of sound for the working fluid whereas the time scale of the radiation equation is on the order of the speed of light. Comparing the temporal operator of the transport equation (Equation 1) to that of the fluid equations (Equation 58, 59, 60, and 63), we find that unless the time step size is on the order of the speed of light, the transport equation will quickly approach the steady state solution. If the equations are evaluated over a conventional fluid time step (some reasonable fraction of the speed of sound) a certain amount of material fluctuation will occur in cells that are turbulent or not fully developed. These material fluctuations will be felt instantaneously, locally and globally, by the radiative transfer equations. Though it is possible to resolve these numerical differences by resolving the material fluctuations on the order of the radiative transfer equation, for most

real applications the computational cost of this is prohibitively expensive. To account for these interactions, the equations are typically rewritten and solved for time averaged quantities[1].

$$\overline{f(r)} = \frac{1}{\delta t}\int_{\delta t} f(r,t)dt \tag{87}$$

The transport equation is written in the time-averaged form as;

$$\frac{1}{c\delta t}(I_{n+1} - I_n) + \bar{\Omega}\cdot\bar{\nabla}\overline{I} + \overline{KI} = \frac{1}{4\pi}\overline{KB}, \tag{88}$$

and the equation of state becomes

$$\frac{dq_R}{dt} = \int_0^\infty\int_0^{4\pi}\overline{KI}d\bar{\Omega}d\nu - \int_0^\infty\int_0^{4\pi}\frac{1}{4\pi}\overline{KB}d\bar{\Omega}d\nu. \tag{89}$$

Evaluating these time-averaged quantities requires at least one more assumption, known as the optically thin eddy approximation. The optically thin eddy approximation assumes that the time averaged opacity multiplied by the time averaged intensity is equivalent to the time averaged absorption operator ($\bar{K}\bar{I} \approx \overline{KI}$) [1]. This implies that the opacity multiplied by the turbulence length scale is small ($Kl_t << 1$). This condition is typically violated in some frequency regions for gas opacities. However, this assumption has been made in all TRI work to date [1].

There are commonly four different approaches to deal with TRI effects [1]. Using the time averaged material properties to evaluate the radiation field, referred to as "no TRI" , implies

$$\overline{K_\nu} = K_\nu(\overline{\phi}); \quad \overline{K_\nu b(\nu,T)} = K_\nu(\overline{\phi})b(\nu,\overline{T}). \tag{90}$$

The variable $\bar{\phi}$ refers to the time averaged material state. The next approach attempts to account for the non-linear correlation between the material properties

and the opacity by using the mean opacity rather than the mean material properties. This is commonly referred to as "absorption coefficient self-correlation",

$$\overline{K_\nu}; \quad \overline{K_\nu b(\nu, T)} = \overline{K_\nu} b(\nu, \overline{T}). \tag{91}$$

It is also possible to account for the non-linearities of the opacity values and the Planck emission spectrum using "Planck function self-correlation"

$$\overline{K_\nu}; \quad \overline{K_\nu b(\nu, T)} = K_\nu(\overline{\phi})\overline{b(\nu, T)}. \tag{92}$$

Finally, it is possible to combine the absorption coefficient and Planck function self-correlations. This is referred to as "full TRI", even though this approach is still approximate as a result of the optically thin eddy approximation:

$$\overline{K_\nu}; \quad \overline{K_\nu b(\nu, T)}. \tag{93}$$

It is obvious that there is non-linear feedback between the radiation field and the material properties. This correlation is generally neglected because of the computational cost of evaluating both the radiative transfer equations and the turbulent flow. Treating the material fluctuations as a separate uncorrelated event from the radiative transfer equation allows for the development of material fluctuation probabilities for the individual cells. These material fluctuation models can be used to directly evaluate the time averaged emission source and cell opacities (full TRI).

A statistically homogeneous, turbulent, idealized, gas combustion flame is modeled in this work, as described by [4], such that every cell in the domain represents a single probable state of the material at that instant in time. In this simplified test case, the radiative transfer equation is not coupled to the material energy balance equation and all material properties are directly related to the combustion product

concentration. As a result, the material properties are directly determined from the gas combustion process, circumventing the need to resolve the non-linearities between the equations. The radiative properties of the background gas are determined from an idealized representation of water vapor;

$$K = C_k(Y_P - \epsilon)\left[c_0 - c_1\left(\frac{A}{T}\right) - c_2\left(\frac{A}{T}\right)^2 - c_3\left(\frac{A}{T}\right)^3 - c_4\left(\frac{A}{T}\right)^4 - c_5\left(\frac{A}{T}\right)^5\right],$$

where the coefficients are defined as [47];$A = 8$, $c_0 = -0.23093$, $c_1 = -1.12390$, $c_2 = 9.41530$, $c_3 = -2.99880$, $c_4 = 0.51382$, and $c_5 = -1.86840E - 05$. The coefficient Y_P is the mass fraction of product present in the cell and ϵ is some small tolerance that prevents the opacity from being zero when no product is present. The combustion of the gas is idealized in such a way that the reaction between product and oxidizer occurs instantaneously:

$$Y_p = \begin{cases} \frac{\xi}{\xi_{st}} & \text{if } \xi \leq \xi_{st}, \\ \frac{1-\xi}{1-\xi_{st}} & \text{if } \xi > \xi_{st}. \end{cases} \tag{94}$$

and ξ and ξ_{st} are the fuel mixture fraction and the stoichiometric proportions of the reaction equation

$$F + O = P \tag{95}$$

F, O, and P denote the fuel, oxidizer, and product, respectively, making the stoichiometric proportions $\xi = 0.5$. Rather then directly solving the energy equation, which would require the solution of the conduction and convection equations, the process is idealized such that the mass fraction of product directly determines the material temperature.

$$T = T_{min} + (T_{max} - T_{min})Y_p \tag{96}$$

These approximations allow for the creation of system that can approximately represent a combustion material while still providing insightful quantitative results to analyze the impact of the TRI phenomenon on the solution.

The main TRI parameters that will be investigated in this work are the following three normalized means;

$$R_{T^4} = \frac{\overline{T^4}}{\overline{T}^4}, \tag{97}$$

$$R_{KI_b} = \frac{K'_p I'_b}{\bar{K}_p \bar{I}_b}, \tag{98}$$

and

$$R_{KG} = \frac{K'G'}{\bar{K}\bar{G}}. \tag{99}$$

These means demonstrate the errors associated with using the mean material properties, the Planck self-correlation, and the thin eddy approximation (Equations 97, 98, and 99 respectively). The primed coefficients represent the difference in the true average from the approximate average;

$$K'G' = \overline{KG} - \bar{K}\bar{G}. \tag{100}$$

and G is the scalar radiative intensity ($G = \int_0^{4\pi} I d\bar{\Omega}$).

5 Approximate Second Order Temporal Integration

5.1 Introduction

This chapter describes the application of the coarse mesh finite difference (CMFD) method to the radiative transfer equations. This approach provides a framework for approximately resolving the non-linearities found in the radiative transfer equations, and a second-order temporal integration scheme for the total photon energy density and material temperature.

5.2 Coarse Mesh Finite Difference

The coarse mesh finite difference (CMFD) method relies on the solution of a low-order problem to accelerate the convergence of a high-order problem. The best way to demonstrate the implementation of this method is to consider the solution of two separate problems, one a coarse representation of the other. The exact coarsening does not need to be accounted for immediately to illustrate the implementation of the method. The coarse and fine representations of the radiative transfer equation can be written as;

$$\frac{1}{c}\frac{\partial I_f}{\partial t} + \bar{\Omega}\cdot\bar{\nabla} I_f = -K_f I_f + K_f B_f(\nu, T), \tag{101}$$

and

$$\int \frac{1}{c}\frac{\partial I_f}{\partial t} dh + \int \bar{\Omega}\cdot\bar{\nabla} I_f dh = -\int K_f I_f dh + \int K_f B_f(\nu, T) dh, \tag{102}$$

where the subscript f indicate a fine variable and h is a homogenization parameter.

CMFD is an iterative scheme. As such, it is necessary to indicate the current iterate l of individual variables. In this work, there is also a non-linear iteration performed over the coarse mesh solution whose iteration index is j.

Consider some homogenization parameter h such that

$$I_c = \int I_f dh \qquad J_c = \int \bar{\Omega} I_f dh. \tag{103}$$

The subscript c indicates a newly defined coarse variable. This parameter represents any combination of coarsening parameters such as space, angle, or frequency. The following coarse mesh transport quantities are computed such that reaction rates are preserved:

$$K_c = \frac{\int K_f I_f dh}{\int I_f dh}, \tag{104}$$

$$B_c = \frac{\int K_f B_f dh}{\int K_f dh}. \tag{105}$$

Typically in CMFD, the coarse mesh and fine mesh models are coupled using the leakage operator [17] such that

$$\int \bar{\Omega} I_f^{l+\frac{1}{2}} dh = \int \bar{\Omega} I_f^{l+\frac{1}{2}} dh - \alpha^{l+\frac{1}{2}} \int \tilde{I}_f^{l+\frac{1}{2}} dh, \tag{106}$$

and

$$J_c^{l+\frac{1}{2}} = J_c^{l+\frac{1}{2}} - \alpha^{l+\frac{1}{2}} \tilde{I}_c^{l+\frac{1}{2}}, \tag{107}$$

where $\tilde{I}_c$ is the average face photon intensity evaluated from the cell centers associated with the cells on either side of the face. The correlation parameter, α, is evaluated from the fine mesh half step correlation equation (Eq. 106). The standard implementation of the CMFD would first require the solution of the fine mesh solution at the half step.

$$\frac{1}{c}\frac{\partial I_f}{\partial t}^{l+\frac{1}{2}} + \bar{\Omega} \cdot \bar{\nabla} I_f^{l+\frac{1}{2}} = -K_f^{l+\frac{1}{2}} I_f^{l+\frac{1}{2}} + K_f^{l+\frac{1}{2}} B_c^l(\nu, T), \tag{108}$$

The energy densities and material temperatures between the coarse and fine problems are then correlated as;

$$\int I_f^{l+1} dh = \frac{\int I_f^{l+\frac{1}{2}} dh}{I_c^{l+\frac{1}{2}}} I_c^{l+1} \tag{109}$$

$$\int T_f^{l+1} dh = \frac{\int T_f^{l+\frac{1}{2}} dh}{T_c^{l+\frac{1}{2}}} T_c^{l+1} \tag{110}$$

Using the cell face fluxes and the cell energy densities from the fine mesh, the correlation parameter at the half step is evaluated.

$$\alpha^{l+\frac{1}{2}} = \frac{\int \bar{\Omega} I_f^{l+\frac{1}{2}} dh - \int \bar{\Omega} I_f^{l+\frac{1}{2}} dh}{\int \tilde{I}_f^{l+\frac{1}{2}} dh} \tag{111}$$

The correlation parameter at the half step $\alpha^{l+\frac{1}{2}}$ is then added to the coarse mesh equations and the non-linear emission source is converged.

$$\frac{1}{c} \frac{\partial I_c}{\partial t}^{j+1} + \bar{\nabla} J_c^{j+1} - \bar{\nabla} \cdot \alpha^{l+\frac{1}{2}} \tilde{I}_c^{j+1} = -K_c I_c^{j+1} + K_c B_c^j(\nu, T) \tag{112}$$

$$\int \frac{\partial E^m}{\partial t}^{l+1} dh = \int \int d\nu d\bar{\Omega} K_c I_c^{j+1} - \int \int d\nu d\bar{\Omega} K_c B_c^j(\nu, T). \tag{113}$$

The material energy density is then used to update the material temperature and therefore the emission source term $B^{j+1}(\nu, T)$. This iteration is performed until the material temperature converges. Upon temperature convergence the coarsened values are translated back to the fine mesh using Equations 109 and 110. The CMFD iteration is performed until the homogenized parameters converge. This is a true acceleration scheme, in that the CMFD method converges to the unaccelerated solution, assuming the same non-linear iteration was also performed on the fine mesh problem.

5.3 Approximate Second Order Temporal Integration via CMFD

Coarse mesh finite differencing, applied as outlined in the previous section, is only a true acceleration method if the CMFD iteration is converged and the final iteration consists of a converged non-linear fine mesh result. In the application of a Monte Carlo method, this is generally too expensive. However, Park et al. have

shown that CMFD can accurately resolve the non-linear emission source associated with the RHT equations[5]. In this research, we propose a second order temporal integration scheme applied only to the coarse mesh equations, with the objective of obtaining better than first-order time integration of the radiative heat transfer equation. The time-integration of the derivative of the function f can be expressed as

$$\int_{t_n}^{t_{n+1}} f'(x,t)dt = f(x,t_{n+1}) - f(x,t_n) \approx \frac{\Delta t}{2}(f'(x,t_{n+1}) + f'(x,t_n)). \tag{114}$$

Using the Taylor expansion of $(f(x,t_{n+1}))$ about t_n where the second time derivative $(f_{tt}(x,t_n))$ is approximated by its Taylor expansion about the point t_{n+1}, it is possible to write;

$$f(x,t_{n+1}) = f(x,t_n) + \frac{\Delta t}{2}(f'(x,t_{n+1}) + f'(x,t_n)) + O(\Delta t^3) \tag{115}$$

The approximate time integration in Eq. (114) matches the newly defined Taylor series expansion up to $O(\Delta t^3)$ which makes this locally a second-order method. We define the approximate integral for the temporal integration scheme more generally as

$$\int_{t_n}^{t_{n+1}} f'(x,t)dt = \xi f'(x,t_{n+1})\Delta t + (1-\xi)f'(x,t_n)\Delta t. \tag{116}$$

This equation is such that the integration parameter can be defined $\xi = 0.5$ or $\xi = 1$ and return Crank-Nicholson or Backward Euler integration schemes. The Backward Euler integration is first order accurate locally, which can easily be shown using the Taylor expansion of $(f(x,t_n))$ about t_{n+1}.

We consider a multigroup transport problem that is coarsened in both angle and frequency ($dh = \frac{d\bar{\Omega}d\nu}{c}$) creating a grey diffusion equation for the coarsened problem. Using the newly-defined integration parameters and the frequency integrated

energy density E

$$E = I_c = \int I_f dh = \frac{1}{c}\int_0^\infty \int_0^{4\pi} I d\bar{\Omega} d\nu \tag{117}$$

yields the following form for the correlation parameter

$$\alpha^{l+\frac{1}{2}} = \frac{F_f^{l+\frac{1}{2}} + D\bar{\nabla}E_f^{l+\frac{1}{2}}}{\tilde{E}_f^{l+\frac{1}{2}}}. \tag{118}$$

Local thermodynamic equilibrium is assumed at the start of the initial time step. This makes the initial correction value equal to zero ($\alpha^0 = 0$) for any problem in global equilibrium (or with a spatially constant photon energy density). If the initial material state is not in global thermodynamic equilibrium, it is necessary to perform a steady state coarse mesh calculation to determine the initial correction coefficient α^0.

From the Crank-Nicholson temporal discretized diffusion equation (Eq. 31), it is possible to write a corrected coarse step as;

$$\begin{aligned}\frac{1}{c}\frac{E^{j+1}-E^n}{\Delta t} - \frac{1}{2}\bar{\nabla}\cdot(D^{j+1}\bar{\nabla}E^{j+1} + D^n\bar{\nabla}E^n) + \frac{1}{2}(\bar{\nabla}\alpha^{l+\frac{1}{2}}\tilde{E}_c^{j+1} + \bar{\nabla}\alpha^n\tilde{E}_c^n) \\ + \frac{1}{2}\left(K_a E^{j+1} + K_a E^n\right) = \frac{K_a}{c}\frac{1}{2}(B^j + B^n),\end{aligned} \tag{119}$$

and

$$\begin{aligned}\frac{1}{c\Delta t}\left(E_m^{j+1} - E_m^n\right) = \frac{1}{2}\int_0^\infty (K_a E^{j+1} + K_a E^n) d\nu \\ - \frac{1}{2}\int_0^\infty \frac{1}{c}(K_a B^j + K_a B^n) d\bar{\Omega} d\nu.\end{aligned} \tag{120}$$

These equations are iterated until the equation of state converges: $T^j \approx T^{j+1}$. Upon convergence the final material properties (at $j+1$) are set to the CMFD half step material properties ($l + \frac{1}{2}$). For the grey case presented in this work, this is only the material temperature. Then, the fine mesh solution is generated via the Monte Carlo method;

$$\frac{1}{c}\frac{\partial I_f}{\partial t}^{l+\frac{1}{2}} + \bar{\Omega}\cdot\bar{\nabla}I_f^{l+\frac{1}{2}} = -K_f I_f^{l+\frac{1}{2}} + K_f B_f^{l+\frac{1}{2}}(\nu, T), \tag{121}$$

The Monte Carlo method in this work is only approximately first order accurate in time because the non-linear relationship between the photon intensity and the emission source term (in the equation of state) is not fully resolved.

The correction coefficient is then evaluated using Equation 118. Using the new coefficient, Equation 112 is used to converge the non-linear emission source;

$$\frac{1}{c}\frac{E^{j+1}-E^{n}}{\Delta t}-\frac{1}{2}(\bar{\nabla}\cdot D\bar{\nabla}E^{j+1}+\bar{\nabla}\cdot D\bar{\nabla}E^{n})+\frac{1}{2}(\bar{\nabla}\alpha^{l}\tilde{E}_{c}^{j+1}+\bar{\nabla}\alpha^{n}\tilde{E}_{c}^{n})$$
$$+\frac{1}{2}\left(K_{a}E^{j+1}+K_{a}E^{n}\right)=\frac{1}{2}\left[\frac{1}{c}(K_{a}B^{j}+K_{a}B^{n})\right], \tag{122}$$

and

$$\frac{1}{c\Delta t}(E_{m}^{j+1}-E_{m}^{n})=\frac{1}{2}\int_{0}^{\infty}(K_{a}E^{j+1}+K_{a}E^{n})d\nu$$
$$-\quad\frac{1}{2}\int_{0}^{\infty}\frac{1}{c}(K_{a}B^{j}+K_{a}B^{n})d\bar{\Omega}d\nu. \tag{123}$$

Upon convergence, the final coarsened material properties (at $j+1$) are adjusted using Equation 110 and set as the material properties for the next fine solution $(l+1)$. The final coarse mesh radiation properties E_{c}^{j+1} are then used to adjust the coarse radiation properties of the fine result (E_{f}^{j+1}) using Equation 109. At this point, the iteration would continue until the corrected coefficients converge. This would would fully resolve the non-linearities. However, in this work the iteration will stop at a fixed number of CMFD iterations and continue to the next time step. Figure 5 shows how the CMFD iteration process generally works.

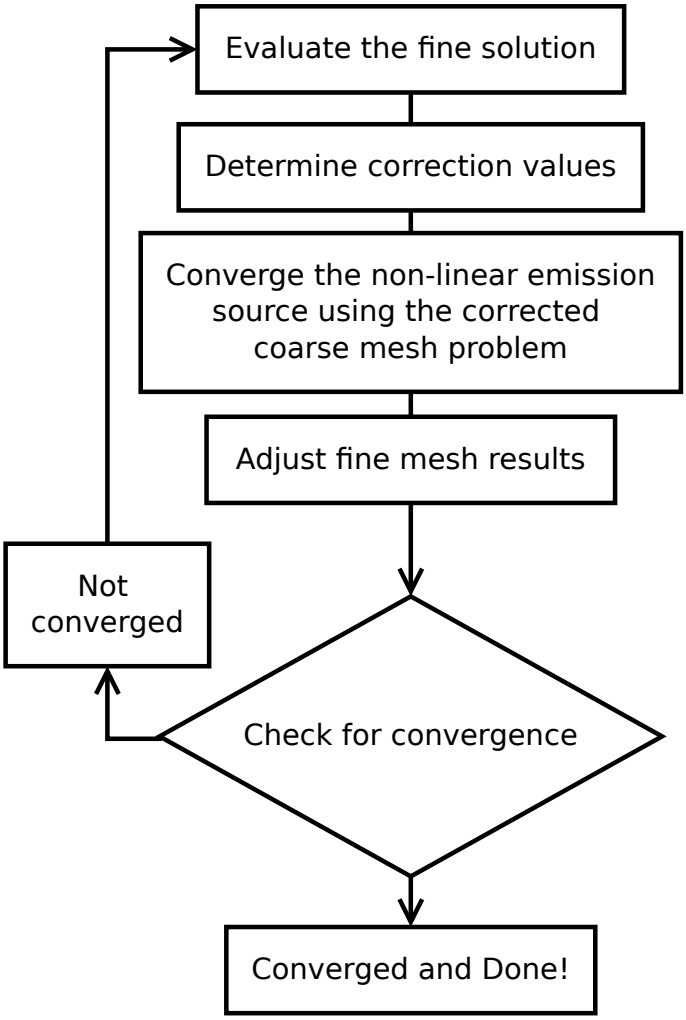

Figure 5: CMFD flow chart

6 Results

6.1 Introduction

This chapter contains the results obtained from numerical simulations supporting the three avenues of research investigated in this dissertation: the parallel performance of gas opacity models, the turbulent radiation interaction effects in particulate laden flows, and the coarse mesh finite difference acceleration of the radiative heat transfer equations.

6.2 Parallel Performance of Gas Opacity Models

The Su and Olson test problem [48] is a frequency-dependent, one-dimensional, semi-infinite benchmark with a semi-analytic solution. The opacity has a "picket fence" distribution involving two different values, each with a given probability of existing anywhere in the frequency domain. The temperature and radiation field are driven with a volumetric radiation source applied near the reflecting boundary. This problem was chosen specifically because the opacities are homogeneous over the entire physical domain, avoiding any errors associated with the correlation assumption of the SLW model. This problem was also chosen because it has a semi-analytic solution providing a basis for comparison with numerical results. Also, the opacity model can be modified to be representative of realistic gas opacities. This allows problems to be compared primarily on the calculation efficiency without being concerned with changes in the accuracy of the solution.

6.2.1 Numerical Test Case

A mock opacity database was developed with 1.5 million microscopic opacity values (k_i $[cm^2]$) in the wavenumber range between 0 and 30000 [1/cm]. The opacities alternate between two values ($K_1 = \frac{2}{11}$ $[1/cm]$ and $K_2 = \frac{20}{11}$ $[1/cm]$) as necessary for the semi-analytic solution created by Su and Olson [48]. The working material is assumed to be an ideal gas to make the database more realistic. This makes it possible to express the opacity as a function of pressure and temperature using the ideal gas equation;

$$k_i = K_i \left(\frac{RT}{P} \right). \tag{124}$$

The total pressure P is constant throughout the problem and R is the ideal gas constant. This microscopic opacity database is used in both opacity models. The specific heat has been set to aT^3, where a denotes the radiation constant [48].

One advantage of the Su and Olson problem is that the spectral resolution using the SLW opacity model is equivalent to that of the line-by-line model. This implies that all other errors associated with the solution are related to spatial resolution, temporal resolution, and other underlying assumptions independent of the opacity models. Figure 6 shows the non-dimensionalized numerical results for the material temperature (lines) compared to the semi-analytic results published by Su and Olson (points) [48]. The initial temperature was specified as 10 $[K]$ and the external radiation source, defined in the region $0 < x < 0.5 \times 10^{-2}$ $[m]$, has an emission temperature of 2000 $[K]$. The y and z boundary faces are periodic and the x boundary faces are perfectly reflecting. The excessive heating at the front of the wave (approximately 20% greater than the analytic solution) and under heating at the tail is related to large time steps with an explicit discretization[6].

All problems are solved using an explicit time discretization with 10 time steps and the material temperature lagged from the previous time step.

Three different scaling studies are performed in this work; strong scaling, weak scaling, and history scaling. Each variant of the problem was solved three times and the results presented are the mean solutions. The simulations were all performed on the Oregon State University High Performance Computing (HPC) Cluster. All nodes used in this work are dual processor 3.0 GHz Intel Xeons with 1024 KB cache and 2GB SDRAM.

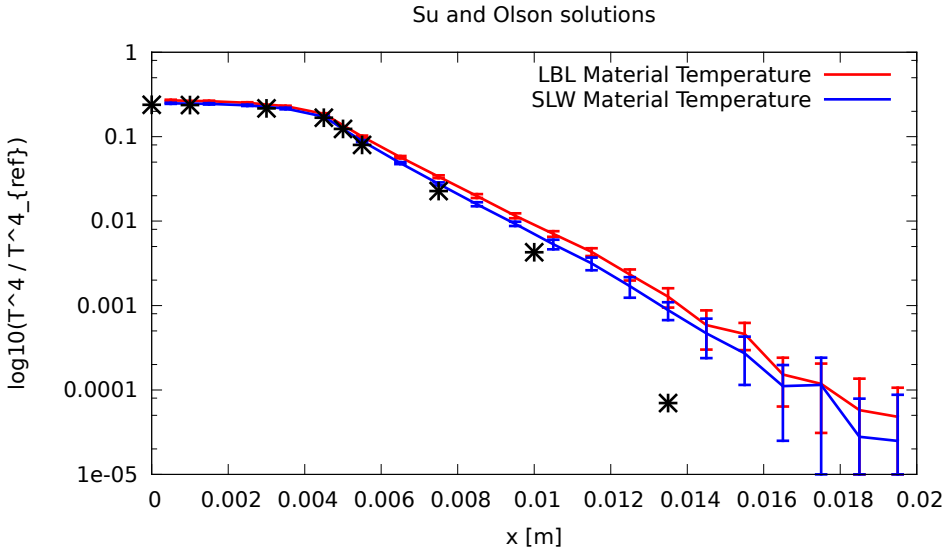

Figure 6: SLW and LBL opacity model solutions compared to the Su and Olson benchmark

Total Run Time		
# of CPUs	LBL	SLW
1	8.019e-1 ± 2.6e-2 [h]	49.33 ± 3.8e-2 [h]
2	8.047e-1 ± 2.0e-2 [h]	26.19 ± 1.1e-1 [h]
4	4.975e-1 ± 4.2e-2 [h]	13.13 ± 7.6e-2 [h]
8	4.158e-1 ± 1.2e-2 [h]	6.781 ± 4.4e-2 [h]
16	2.664e-1 ± 2.1e-2 [h]	3.483 ± 1.4e-2 [h]

Table 1: Strong scaling total run time evaluations for each opacity model

Avg. CPU Time		
# of CPUs	LBL	SLW
1	8.014e-1 ± 3.4e-3 [s]	119.3 ± 4.0e-1 [s]
2	3.954e-1 ± 6.6e-4 [s]	48.42 ± 1.5e-1 [s]
4	1.994e-1 ± 1.9e-3 [s]	24.47 ± 6.7e-2 [s]
8	9.943e-2 ± 5.5e-4 [s]	12.39 ± 1.1e-2 [s]
16	4.970e-2 ± 2.3e-4 [s]	6.235 ± 1.6e-2 [s]

Table 2: Strong scaling average CPU run time for each opacity model

6.2.2 Strong Scaling

All simulations in the strong scaling study used the same mesh ($20 \times 8 \times 8$) to discretize the physical domain $0.02 \times 0.08 \times 0.0$ $[m]$. We have employed a volumetric domain decomposition in which every processor receives approximately the same number of cells. The number of processors varied from 1 to 16 by multiples of 2 to perform the scaling study. The solver used 10 time steps reach the non-dimensionalized final time ($\tau = c\bar{K}t$) of 0.1.

Tables 1 and 2 show the computational costs of the two different opacity models in the strong scaling study. In Table 2, "Avg. CPU Time" refers to the average CPU time used per processor. Figure 7 shows the strong scaling efficiencies for both the SLW and LBL opacity models. The scaling efficiency is determined using

Avg. Load Imbalance		
# of CPUs	LBL	SLW
1	0.0 ± 0.0 [%]	0.0 ± 0.0 [%]
2	87.28 ± 5.1e-2 [%]	61.89 ± 9.7e-2 [%]
4	87.61 ± 1.1e-1 [%]	59.40 ± 3.1e-1 [%]
8	104.4 ± 9.9e-2 [%]	59.30 ± 2.4e-1 [%]
16	120.1 ± 9.4e-2 [%]	59.91 ± 2.0e-1 [%]

Table 3: Strong scaling average average load imbalance for each opacity model

Equation 54.

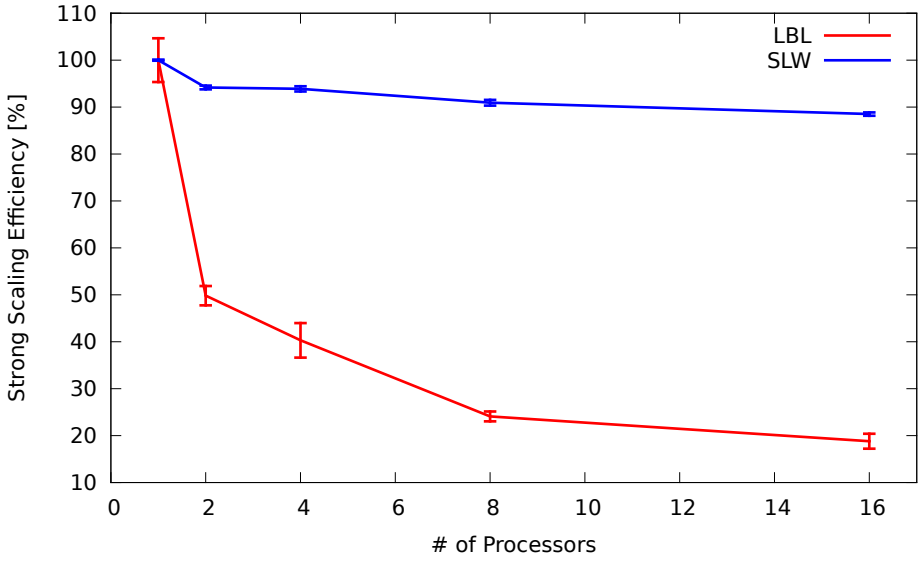

Figure 7: SLW and LBL opacity strong scaling for the Su and Olson benchmark

Weak Scaling Run Parameters			
# of CPUs	mesh dimensions	problem size [m]	# of MC particles
1	$20 \times 2 \times 2$	$0.02 \times 0.02 \times 0.02$	10,000
4	$20 \times 4 \times 4$	$0.02 \times 0.04 \times 0.04$	40,000
15	$20 \times 8 \times 8$	$0.02 \times 0.08 \times 0.08$	160,000

Table 4: Parameters used for run cases in the weak scaling study

Total Run Time		
# of CPUs	LBL	SLW
1	4.972e-2 ± 2.3e-3 [h]	3.153 ± 3.9e-2 [h]
4	1.614e-2 ± 7.2e-3 [h]	3.389 ± 3.6e-3 [h]
16	2.600e-1 ± 2.1e-2 [h]	3.483 ± 1.4e-2 [h]

Table 5: Weak scaling total run time evaluations for each opacity model

6.2.3 Weak Scaling

The weak scaling study was composed of three variants of the Su and Olson benchmark. The parameters in these variants are listed in Table 4. The problem size was only increased in the direction of the periodic boundaries because the solution varies only in the x direction. This helps ensure that the resolution of the problem is increased in a meaningful way. It is also necessary to scale the number of particle histories as the size of the problem is increased to achieve an accuracy and statistical error comparable to that of the serial calculations.

Tables 5 and 6 show the average run times and the average CPU times of the weak scaling study, respectively. Figure 8 shows the weak scaling efficiencies for each opacity model. The weak scaling efficiencies were calculated using Equation 55. The error bars on the plot show the standard deviation from the averaged results.

Avg. CPU Time		
# of CPUs	LBL	SLW
1	4.532e-2 ± 3.7e-4 [s]	7.384 ± 9.4e-2 [s]
4	4.532e-2 ± 1.0e-4 [s]	7.025 ± 6.5e-3 [s]
16	4.970e-2 ± 2.3e-4 [s]	6.235 ± 1.6e-2 [s]

Table 6: Weak scaling average CPU run time for each opacity model

Avg. Load Imbalance		
# of CPUs	LBL	SLW
1	0.0 ± 0.0 [%]	0.0 ± 0.0 [%]
4	139.5 ± 1.5e-1 [%]	50.73 ± 3.1e-2 [%]
16	120.1 ± 9.4e-2 [%]	59.91 ± 2.0e-1 [%]

Table 7: Weak scaling average load imbalance for each opacity model

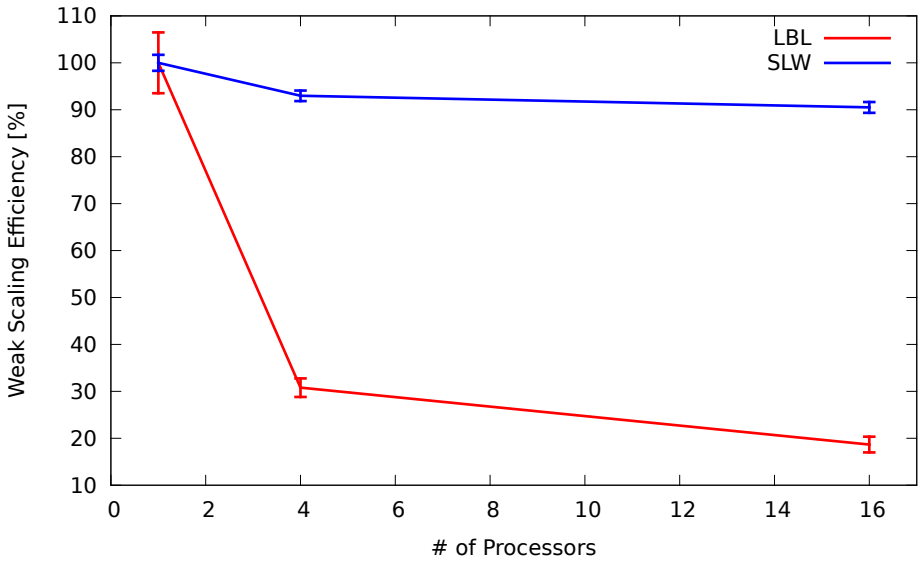

Figure 8: SLW and LBL opacity strong scaling for the Su and Olson benchmark

Total Run Time		
# pre time step ($\times 40,000$)	LBL	SLW
1	1.614e-1 ± 7.2e-3 [h]	3.389 ± 3.6e-3 [h]
2	3.397e-1 ± 6.4e-3 [h]	3.486 ± 9.7e-2 [h]
4	6.894e-1 ± 1.4e-2 [h]	3.475 ± 9.2e-3 [h]
8	1.473 ± 1.1e-2 [h]	3.581 ± 2.8e-2 [h]
16	2.889 ± 1.7e-2 [h]	3.844 ± 1.1e-2 [h]

Table 8: History scaling total run time evaluations for each opacity model

Avg. CPU Time		
# per time step ($\times 40,000$)	LBL	SLW
1	4.532e-2 ± 1.0e-4 [s]	7.035 ± 6.5e-3 [s]
2	9.127e-2 ± 2.0e-4 [s]	7.346 ± 9.1e-2 [s]
4	1.851e-1 ± 1.1e-4 [s]	7.623 ± 7.3e-2 [s]
8	3.921e-1 ± 5.1e-3 [s]	8.149 ± 1.3e-2 [s]
16	8.537e-1 ± 4.2e-3 [s]	8.673 ± 2.2e-2 [s]

Table 9: History scaling average CPU run time for each opacity model

6.2.4 History Scaling

The history scaling study is composed of five different variations of the Su and Olson problem. The same mesh ($20 \times 4 \times 4$), decomposed onto 4 processors in the domain $0.02 \times 0.04 \times 0.0$ $[m]$, was used for every variation of the history scaling problems. The histories increased by factors of two ranging from 40,000 to 640,000 particles per time step.

The total run times and average CPU times are presented in Tables 8 and 9, respectively. Figure 9 shows how the average history CPU time (Eq. 56) varies as a function of the number of histories used for both the SLW and LBL models.

Avg. Load Imbalance		
# per time step ($\times 40,000$)	LBL	SLW
1	139.5 ± 1.5e-1 [%]	50.73 ± 3.1e-2 [%]
2	139.6 ± 5.6e-2 [%]	48.41 ± 4.9e-1 [%]
4	140.2 ± 6.2e-2 [%]	46.28 ± 1.7e-1 [%]
8	142.0 ± 3.2e-1 [%]	41.15 ± 1.3e-1 [%]
16	143.6 ± 3.8e-1 [%]	40.58 ± 6.5e-2 [%]

Table 10: History scaling average load imbalance for each opacity model

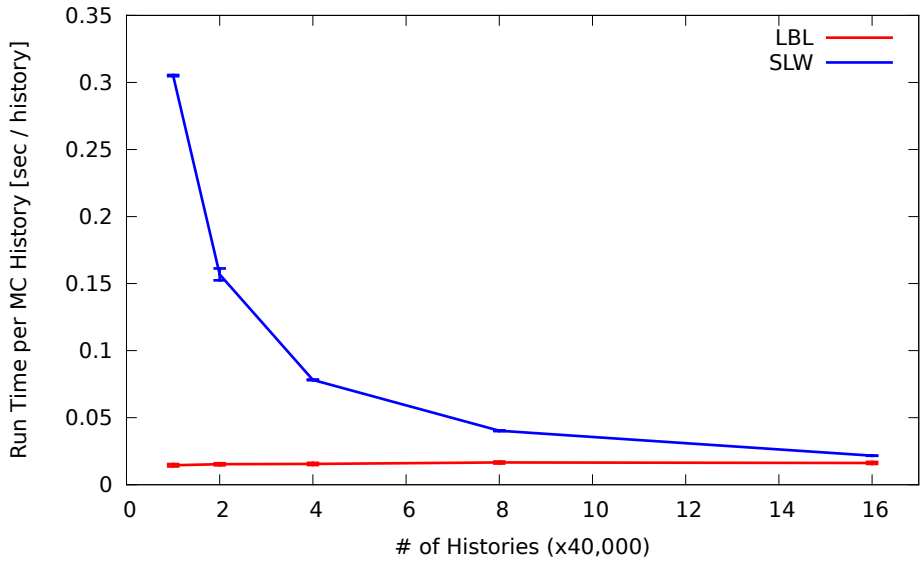

Figure 9: SLW and LBL opacity history scaling for the Su and Olson benchmark

6.2.5 Load Balance

The load imbalance is represented by the percent deviation (Eq. 57) of the average CPU times found in Tables 3, 7, and 10. Figures 10 and 11 show how the load imbalance is affected in all three scaling studies. Note that the x-axis in these figures is the scaling factor, rather than the number of histories or the number of processors used.

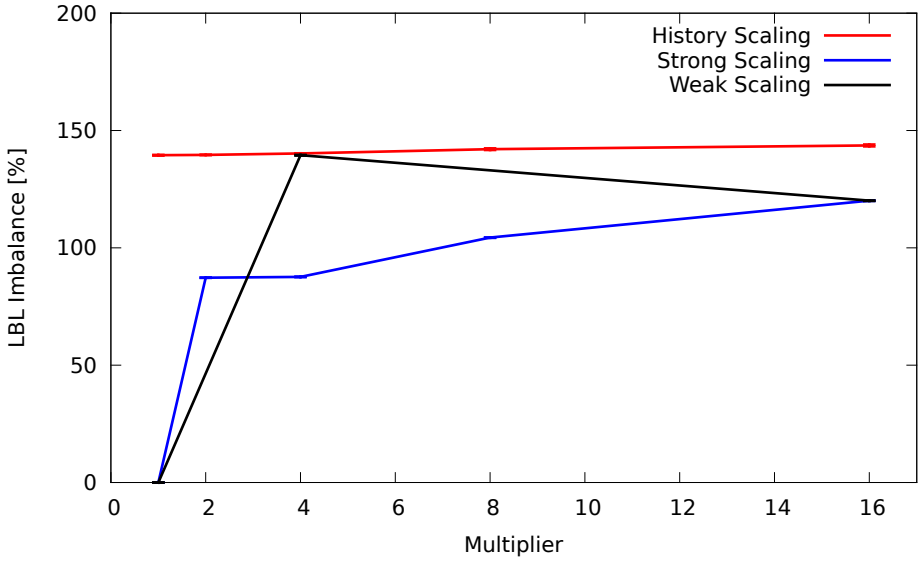

Figure 10: LBL model load imbalance for the Su and Olson benchmark

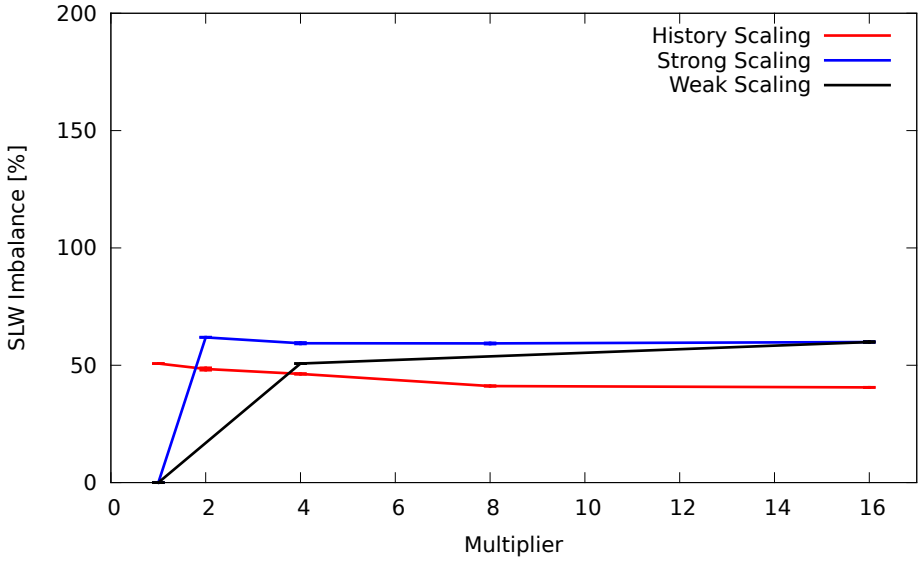

Figure 11: SLW model load imbalance for the Su and Olson benchmark

6.2.6 Opacity Results Summary

The numerical results for both the SLW and LBL opacity models were compared to the Su and Olson frequency dependent benchmark [48]. These results show the performance of these opacity models with respect to three different scaling approaches; strong scaling, weak scaling, and history scaling. The short CPU times, as compared to the large total run time, are indicative of the amount of IO operations and processor communication that occurs in both methods. These algorithms could be improved by reducing the IO operations for both methods which would change the magnitude of the results. It can be assumed, however, that these changes in magnitude should have little effect on the overall trends associated with the scaling. These trends are primarily a function of the number of mathematical operations and the problem size. A more in-depth discussion of this can be found in the conclusions section.

6.3 Turbulence Radiation Interaction Effects

We have modified the test problem developed by Deshmukh et al. [4] to include particulate in a statistically homogeneous non-premixed system. Two different particulate tracking procedures were implemented for the coal particulate; the chord length method and geometric tracking. These test problems illustrate the changes in the TRI effects associated with different treatments of the particulate in the system. This includes an investigation of the following phenomena: treating the particulate temperature as a constant or the mean cell temperature, using the chord length method versus geometric tracking, variations in the particulate thickness, and variations in the particulate flow distribution (Stokes number).

6.3.1 Chord Length vs Geometric Optics

To compare the results of the geometric tracking procedure to the chord length method, the problem presented by Olson [49] is evaluated using both methods. This problem does not have an analytic result. This is a frequency-independent transient problem consisting of a cubic domain which is one mean free path in optical thickness of the background medium. The spheres that populate the domain are equally sized and have an opacity 100 times greater than the background medium. The specific heat is defined as $4T^3$. The x-direction boundary faces are vacuum with a face source applied to one side of the cube and the exiting heat flux computed at the at the opposite face. The remaining boundary surfaces are treated as reflecting boundaries. Figure 12 compares the normalized heat flux at the exit face ($\frac{F_{exit}}{F_0}$) found using the chord length method, geometric tracking, and a single harmonic mean opacity. The harmonic mean is defined as;

$$K_h = \frac{1}{\frac{f_p}{K_p} + \frac{f_b}{K_b}} \tag{125}$$

where f_p and f_b are the volume fractions of the particulate and background media, respectively. The harmonic mean, rather than the atomic mixing, was suggested by Olson [49] because of the poor performance of the atomic mix model in light particle loading.

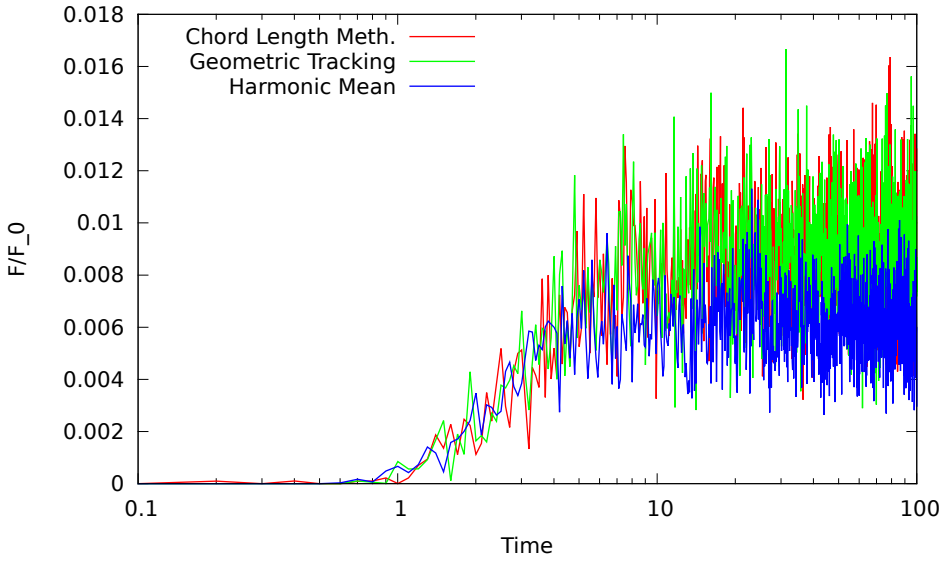

Figure 12: Average normalized exit heat flux F_{exit}/F_0

6.3.2 Particulate Properties

The material properties for the particulate are chosen to represent properties that would be expected in pulverized coal combustion systems. There are three main classifications of coal; anthracite (greater than 86% fixed carbon, less than 14% volatile matter), bituminous (greater than 86% fixed carbon, less than 14% volatile matter, greater than 10,500 Btu), and lignite (less than 8,300 Btu) [50]. Each of these classifications reflect generalized composition and potential energy parameters. We have chosen bituminous coal properties in this research.

Manickavasagam et al.[7] found that the refraction index n (see Eq. 66) in a specific type of bituminous coal, Kentucky coal #9, was relatively insensitive to photon frequency. This has been previously discussed[7, 1]. Given the definition of the material opacity, K is proportional to the absorptive index (see Eq. 67) and the photon frequency. It is possible to develop an approximate opacity that is independent of frequency by fitting the absorptive index, as a function of frequency, with a linear function that is inversely proportional to the frequency: $k \approx k_f = \frac{k_0}{\nu}$.

$$K = \frac{4\pi k \nu}{c_0} = \frac{4\pi k_0}{c_0} \tag{126}$$

We have used a least-squares fit of the polynomial representation of the bituminous coal (Kentucky coal #9) absorptive index provided by Manickavasagam et al.[7]. A graphical representation of the fit can be found in Figure 13. The least-squares fit was found such that the derivative of the sum of the squares is zero;

$$R^2 = \sum_{i=1}^{N} (k(\nu_i) - k_f(\nu_i))^2 \tag{127}$$

$$\frac{dR^2}{dk_f} = 0 = 2.0 \sum_{i=1}^{N} (k(\nu_i) - k_f(\nu_i)) \frac{1}{\nu_i} \tag{128}$$

This sum can be directly evaluated and solved for k_0;

$$k_0 = \sum_{i=1}^{N} \frac{\frac{k(\nu_i)}{\nu_i}}{\frac{1}{\nu_i^2}} \tag{129}$$

using 100 data points in the wavelength range $3 \leq \lambda \leq 19$ $[\mu m]$ results in a fitted coefficient of $k_0 = 1.4806e-2$ $[\frac{1}{\mu m}] = 4.4388e12$ $[1/s]$.

The Stokes number as defined in Equation 65 indicates the amount of particulate clustering in the system. This equation can be used to determine an effective particulate density that will yield a desired Stokes number, given the particulate properties, the fluid properties, and the Kolmogorov length scale indicative of the fluid flow profile:

$$\tilde{\rho_p} = 18St\rho_f \left(\frac{\eta}{d_p}\right)^2 \tag{130}$$

Both the fluid field and the radiation field are directly proportional to the particle diameter as indicated by Equations 65 and 68, respectively. In order to keep the radiation field insensitive to the fluid flow, (as in the work of Deshmukh et al.[4]), the radiation properties of the coal are scaled such that they match properties typically found in pulverized coal systems. The bulk of coal particulate found in pulverized coal is on the scale of $d_p = 5.8$ $[\mu m]$ [7]. Note that this is not the bulk from a mass perspective, but rather from the perspective of the total number of particles. In this work, all particulate are assumed to be of equal size. Using this particulate size and the fitted gray opacity value K, it is possible to determine the effective opacity $\tilde{K}$ such that the diameter in number of mean free paths is equivalent $\frac{d_p}{M_{fp}} = \frac{\tilde{d_p}}{\tilde{M_{fp}}}$. A mean free path is defined as;

$$M_{fp} = 1/K, \tag{131}$$

and the particle diameter as a function of mean free paths can be defined as;

$$N_{mfp} = \frac{d_p}{M_{fp}}. \tag{132}$$

TRI run cases			
Test Case ID	Stokes #	$\tilde{\rho_p}$[kg/m^3]	Packing fraction
TRI_1	0.0	0.0	0.0
TRI_2	0.2	80	9.6e-2 %
TRI_4	2.3	900	9.6e-2 %
TRI_5	2.3	900	1.9e-1 %

Table 11: Variations of the TRI test problem

Given these definitions the effective opacity can be evaluated as;

$$\tilde{K_p} = \frac{N_{mfp}}{\tilde{d_p}} \tag{133}$$

6.3.3 TRI test cases

In the test problem developed by Deshmukh et al., a fully periodic three dimensional domain is defined. A velocity forcing function [51] initiates statistically homogeneous turbulence in the system. After the system reaches a statistically steady state flow regime, as determined from the fluctuations in the turbulent kinetic energy;

$$\frac{\partial < \bar{u} \cdot \bar{u} >}{\partial t} \approx 0. \tag{134}$$

Seven different variations of the Deshmukh problem were considered: one without particulate and three different particulate-laden problems. The particulate-laden problems use various Stokes numbers and different packing fractions. Specific details of these problems can be found in Tables 11 and 12.

All particulate runs were started from the same initial restart problem. The turbulent kinetic energy (Eq. 134) was monitored to verify that the problem had reached a statistically steady state flow pattern (Figure 14). Figures 15, 16, and 17 show particulate distributions in a thin slice (1/64 of the total length) of the domain

Consistent Run Parameters		
Parameter	Value	Units
Reynolds #	77	N/A
Prandtl #	0.75	N/A
Lewis #	1.0	N/A
Fluid Density	1.0	kg/m^3
Particle Diameter	0.012	m
T_min	750	K
T_max	3000	K

Table 12: Flow solver run parameters used for all test cases

for each of the different Stokes numbers at the initialized turbulent state. In these figures, the dots indicate the particulate center locations. The variable *Npar* in the title of Figure 17 refers to the number of particulate spheres represented by each point; in this case one point is representative of two particulate spheres. A larger *Npar* allows for a reduction in computational resources while still being able to account for larger packing fractions. After the steady-state flow pattern is achieved, the simulation is paused and populated randomly with fuel and oxidizer via the approach described by Eswaran et al. [52]. This initialization relies on the use of a Fourier transform in which the Fourier amplitudes are randomly selected and then inversely transformed back to physical space and used to populate the material properties. This helps smooth the random double-δ distribution in space. [Every cell is either pure fuel or oxidizer.] This defines the initial material distribution in a manner consistent with Deshmukh et al. [4]. Our research does not use the wavenumber filter originally described in the Eswaran paper. This results in a significantly faster build-up of combustion products. Figures 18 and 19 are example slices of the fuel concentration after the first time step and the final time step of a single TRI run. These plots show that after the first time step a significant amount

of the fuel has reacted with the oxidizer and at the final time step nearly all of the fuel has reacted.

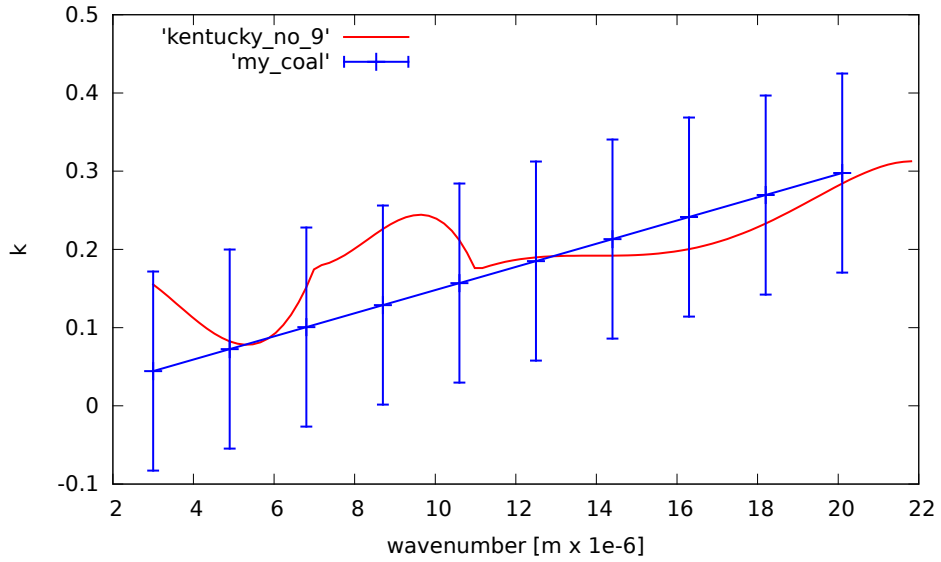

Figure 13: Least-squares fit of the coal data provided by Manickavasagam et al. [7]

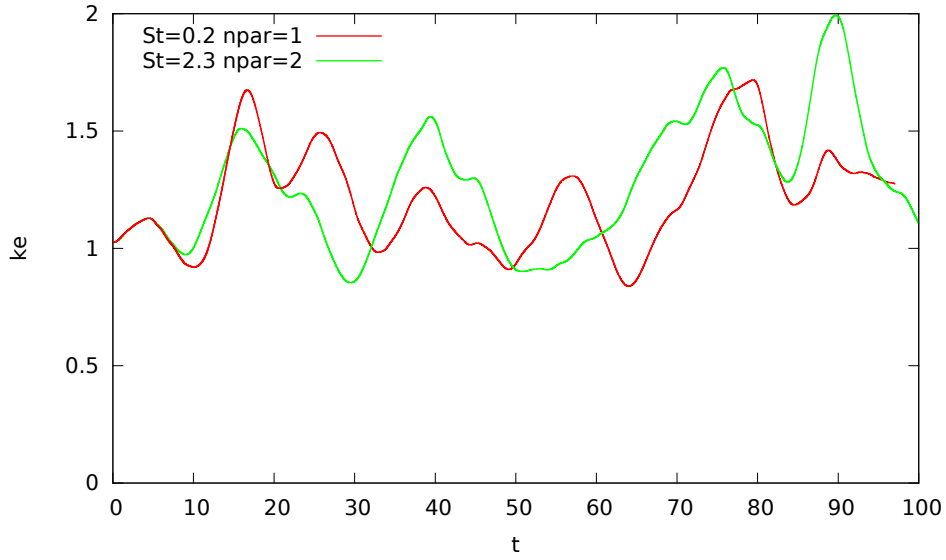

Figure 14: Kinetic energy as function of time for particulate problem initialization

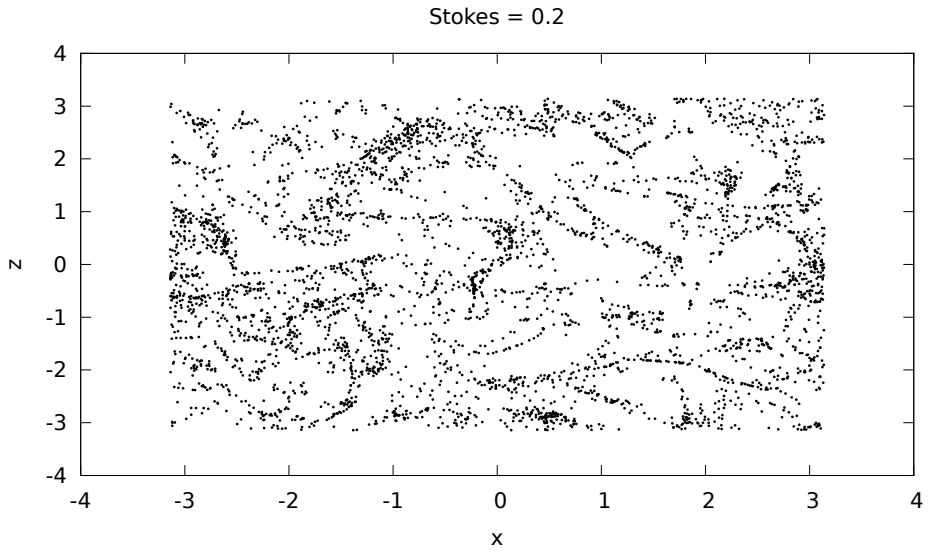

Figure 15: Particulate clustering for a Stokes number of 0.2

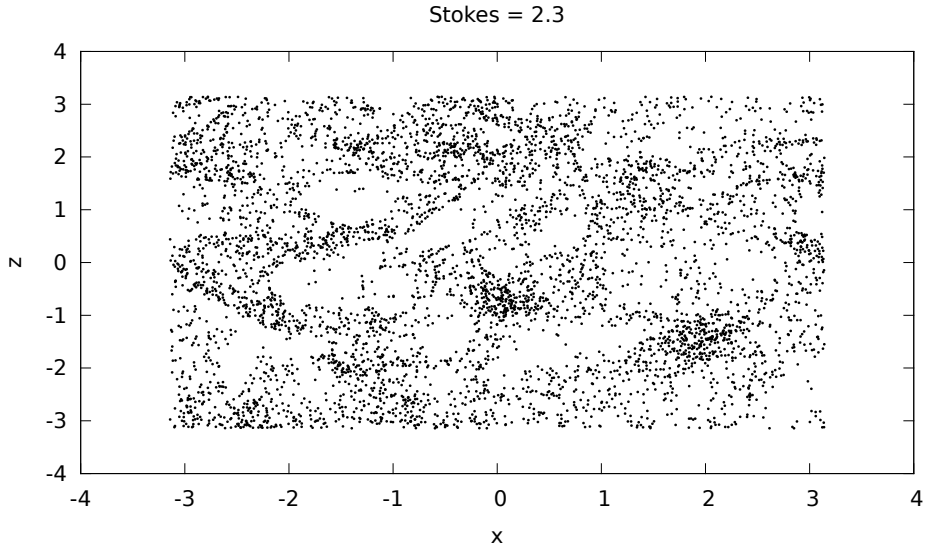

Figure 16: Particulate clustering for a Stokes number of 2.3

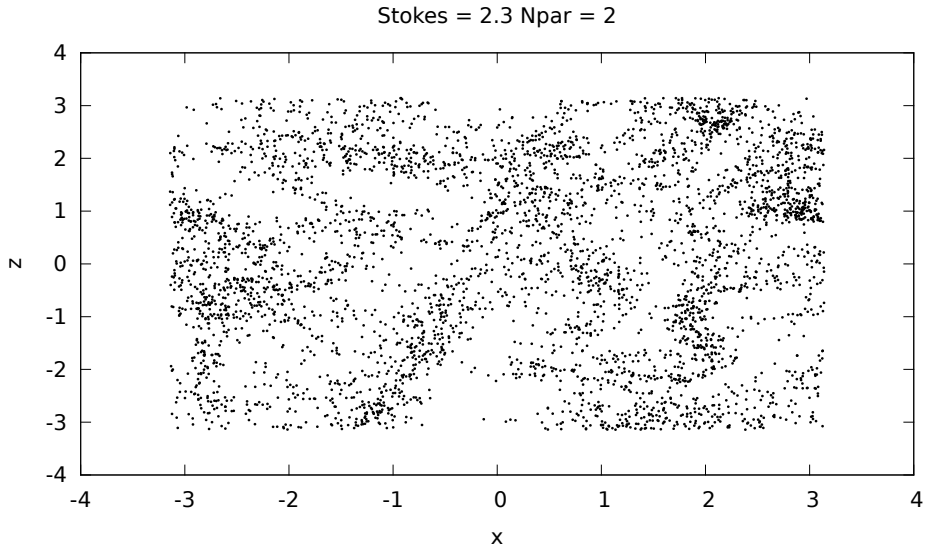

Figure 17: Particulate clustering for a Stokes number of 2.3 at twice the packing fraction used in Figure 16

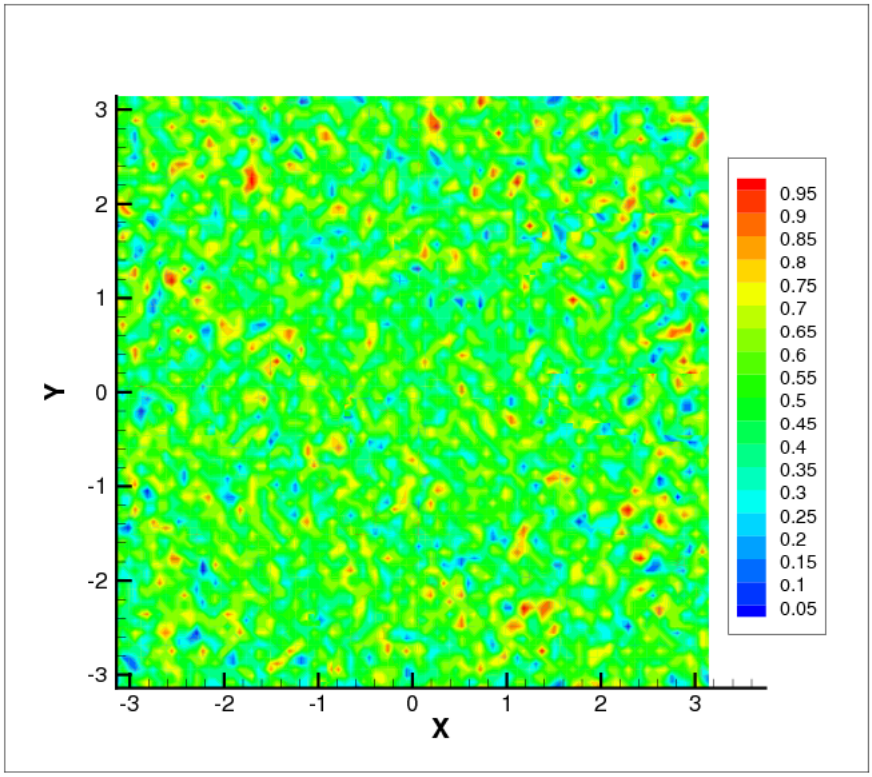

Figure 18: Fuel concentration after a single time step

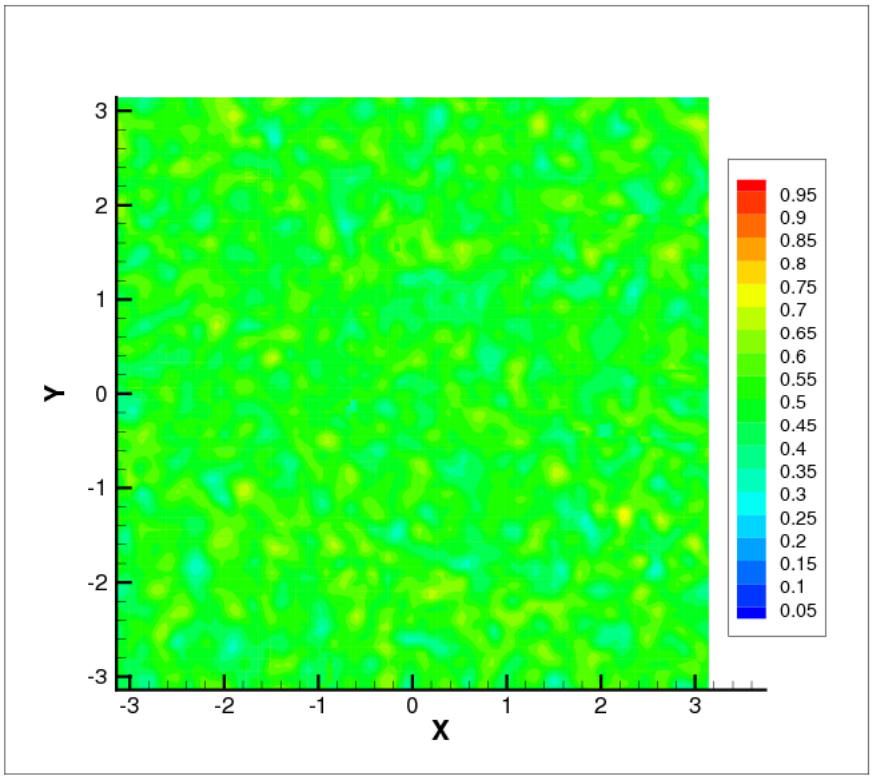

Figure 19: Fuel concentration after the final time step

6.3.4 TRI test results

The mixture fraction is the driving parameter in these simulations because it specifies all material properties. This completely drives the radiation solution. Figure 20 plots the variance of the mixture fraction as a function of non-dimensional time for the different problem initializations presented in Table 11.

There are two common ways to treat the particulate temperature: constant, equal to the initial temperature, or equal to the mean cell temperature in which it resides. Fly ash and char are typically treated at the mean cell temperature because of their size. Coal particulate on the other hand is considerably larger and therefore is less sensitive to the cell temperature. The difference in the normalized mean of the temperature (Equation 97) for the different Stokes numbers and packing fractions is plotted in Figures 21, 22, and 23.

Figure 24 shows the normalized temperature mean (R_T^4) for all four different cases. In all the cases shown in this figure, the mean cell temperature was used for the temperature of the particulate. Variations in these curves are strongly correlated to the variations in the mixture fraction (Figure 20).

The normalized emission mean (Equation 98) is also strongly driven by variations in the mixture fraction and particulate opacity. Figures 25, 26, and 27 show the difference in the means when using a constant particulate temperature versus the cell mean temperature.

The normalized emission mean (R_{KI_b}) depends on not only the temperature treatment of the particulate, but also the opacity. To determine the sensitivity, three different opacity values were chosen ($K_p = 9.2, K_p = 92$, and $K_p = 920$). Figure 28 shows the difference in the normalized emission mean for the three different

opacities with St=2.3 and $Npar$=1.

Figure 29 shows all the normalized emission mean values for the various problem initializations outlined in Table 11. The differences in these curves correlate with the differences in the material mixture fraction variance, shown in Figure 20.

The normalized absorption mean (Equation 99) is strongly dependent on both the radiation source term and opacity distribution. The statistical noise in these results make them difficult to evaluate. Changes can best be illustrated by comparing the normalized means of the cases that should have the greatest differences. The problem is most sensitive to the mixture variance. The second most sensitive variable is the particulate thickness. Figure 30 shows the normalized absorption mean (R_{KG}) for the test case without particulate and the test case with St=2.3, $Npar = 1$, $K_p = 920$, and the particulate temperature defined as cell mean temperature. These cases should have the greatest difference because of the sensitivity to mixture variance and particulate thickness.

To observe the effect of particulate thickness, Figure 31 shows the thin test problem ($K_p = 9.2$) and the thick test problem ($K_p = 920$). Figure 32 shows the dependence on the particulate temperature definition using the St=2.3 and $Npar = 2$ test case.

All results to this point have been evaluated using the chord length method. Figures 33 and 34 show the normalized absorption means as calculated by geometric optics versus the chord length method. The solution for problems with $Npar > 1$ cannot be evaluated using geometric optics because realizations are not created for all particulate. The geometric optics cases were only evaluated for half the time of the chord length runs because of memory allocation requirements and computation time limitations.

The volume averaged intensity as a function of non-dimensional time is plotted in Figures 35, 36, and 37. Figures 35 and 36 show the average intensity as determined from the chord length method as compared to the geometric optics method. Figure 37 show the results for all simulation parameters outlined in Table 11.

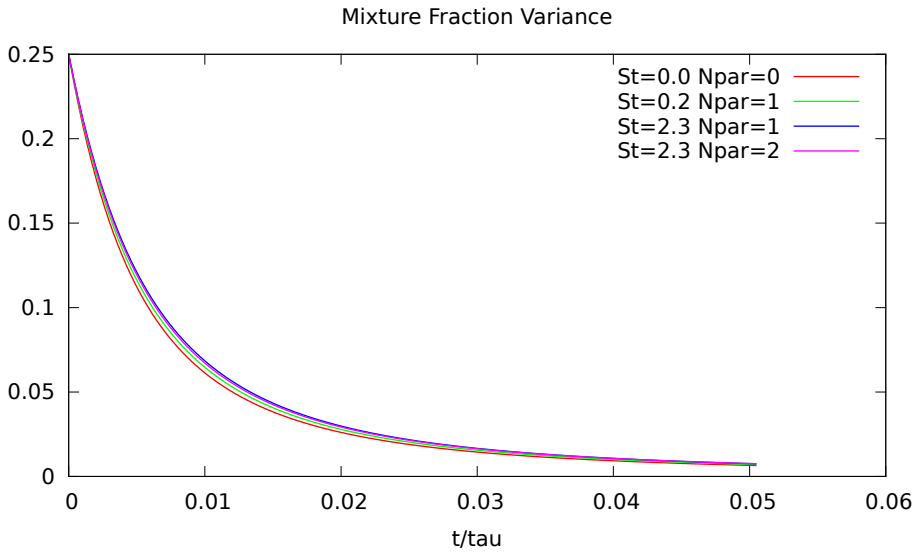

Figure 20: Variance of the mixture fraction for the different run parameters

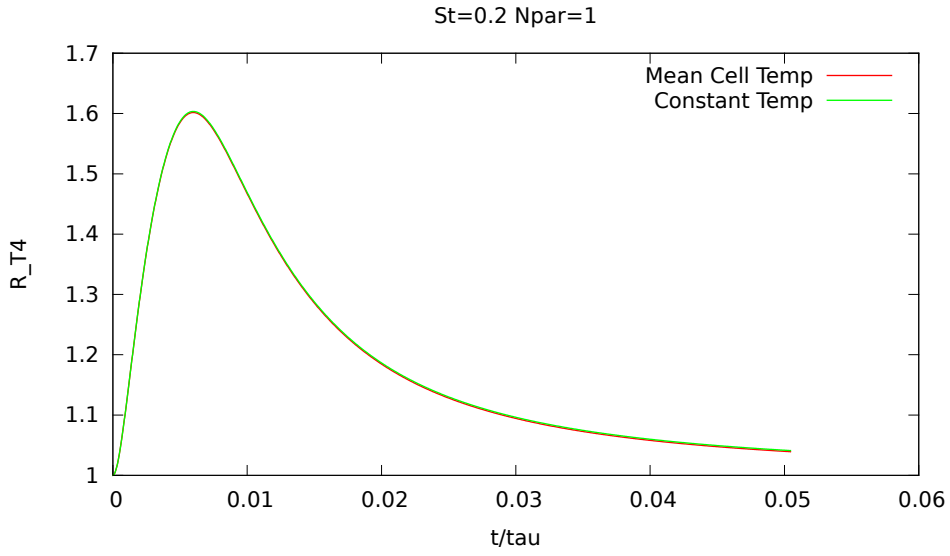

Figure 21: Constant temperature versus mean cell temperature treatments for St=0.2

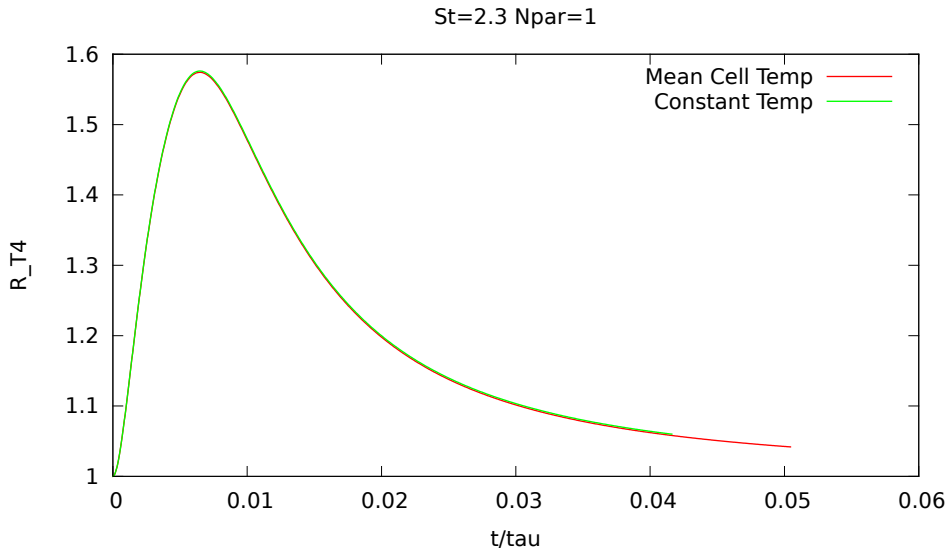

Figure 22: Constant temperature versus mean cell temperature treatments for St=2.3

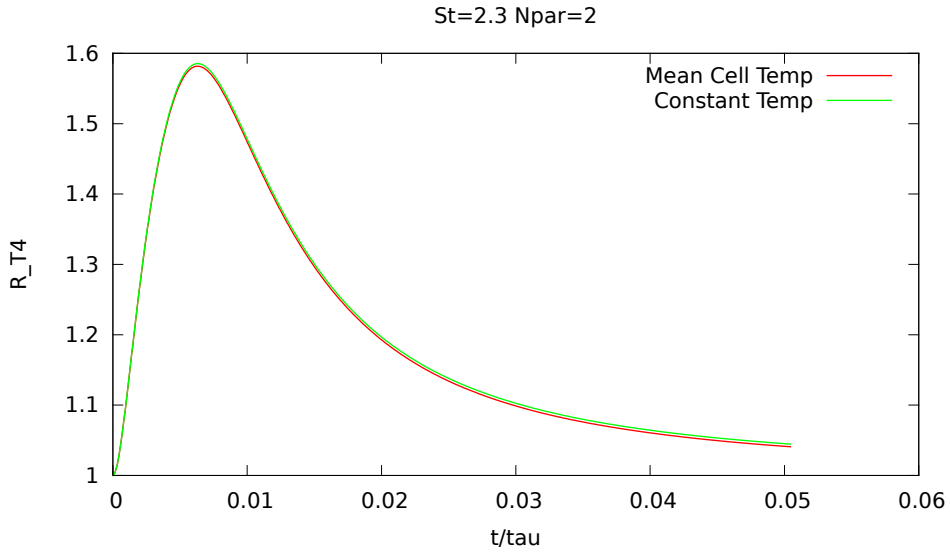

Figure 23: Constant temperature versus mean cell temperature treatments for St=2.3 with twice the packing fraction ($Npar = 2$) used in Figure 22

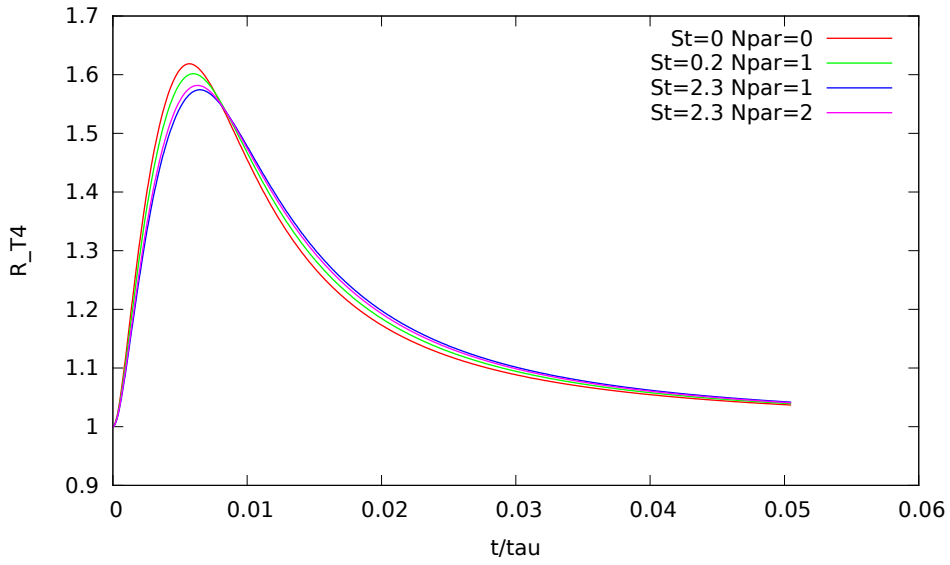

Figure 24: The normalized temperature means (R_{T^4}) for the four different problem initializations outlined in Table 11

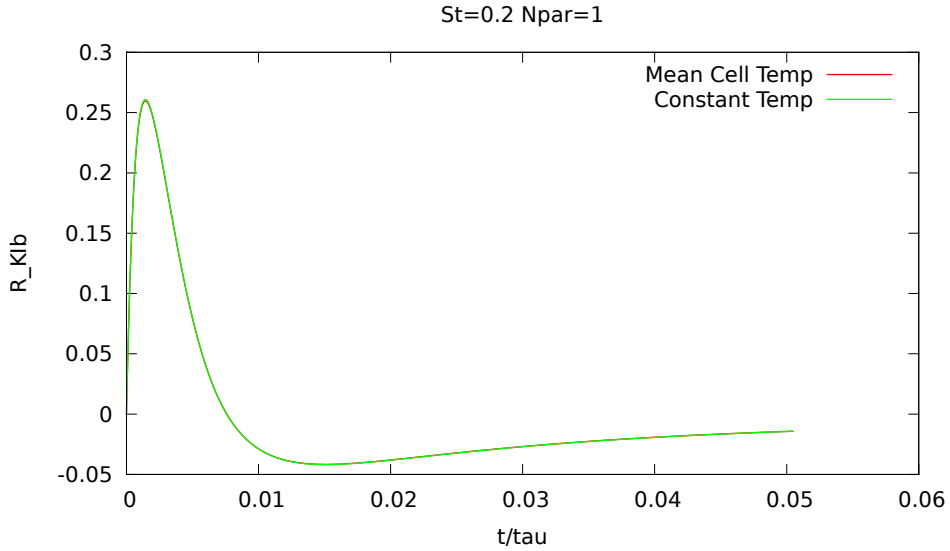

Figure 25: Constant temperature versus mean cell temperature treatments for St=0.2

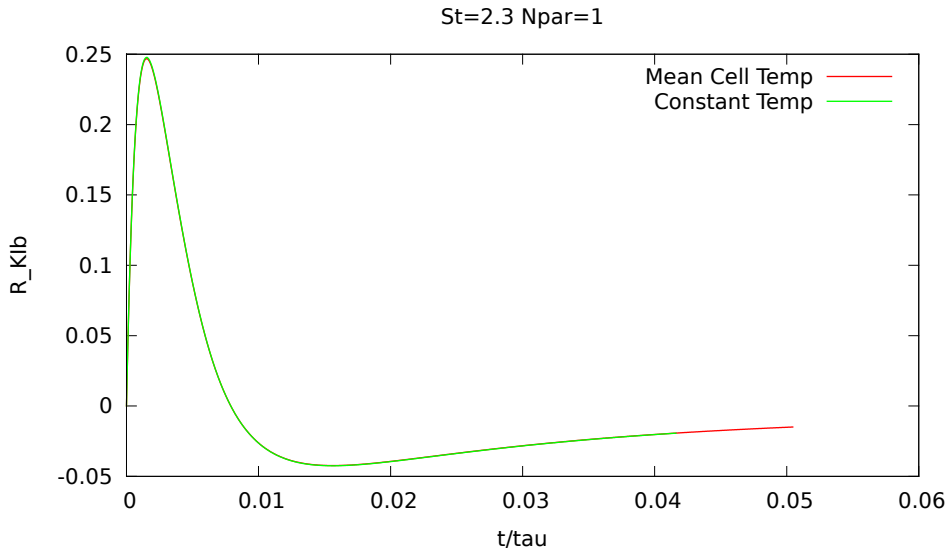

Figure 26: Constant temperature versus mean cell temperature treatments for St=2.3

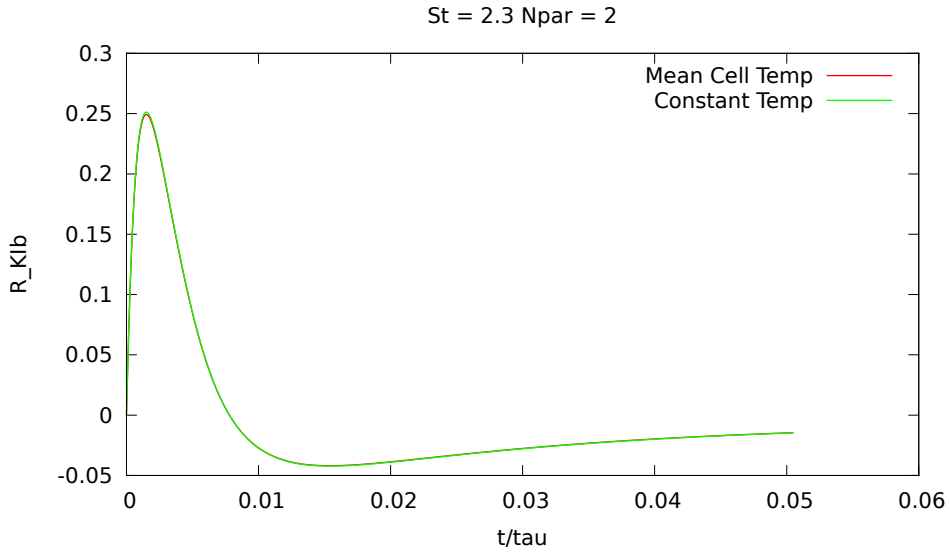

Figure 27: Constant temperature versus mean cell temperature treatments for St=2.3 with twice the packing fraction ($Npar = 2$) used in Figure 26

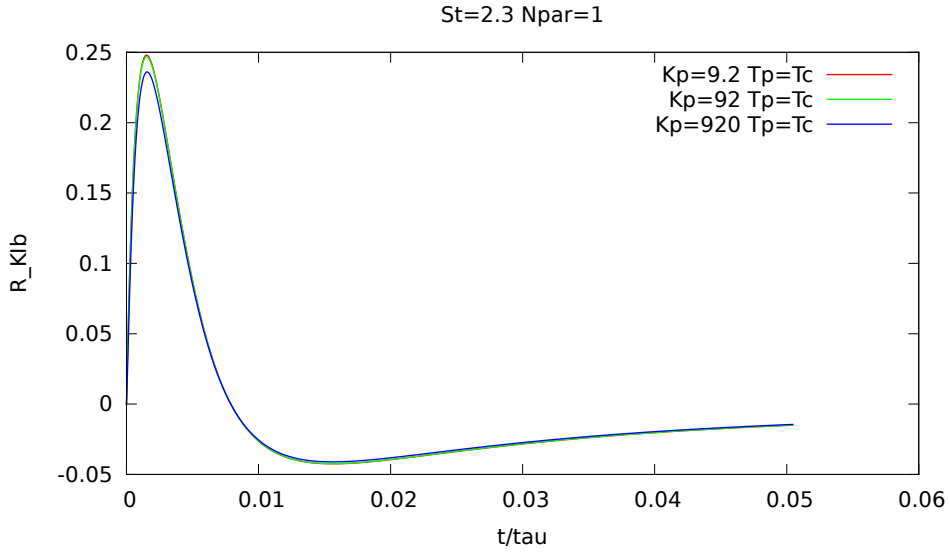

Figure 28: Constant temperature versus mean cell temperature treatments for St=2.3 with twice the packing fraction (Npar=2) used in Figure 26

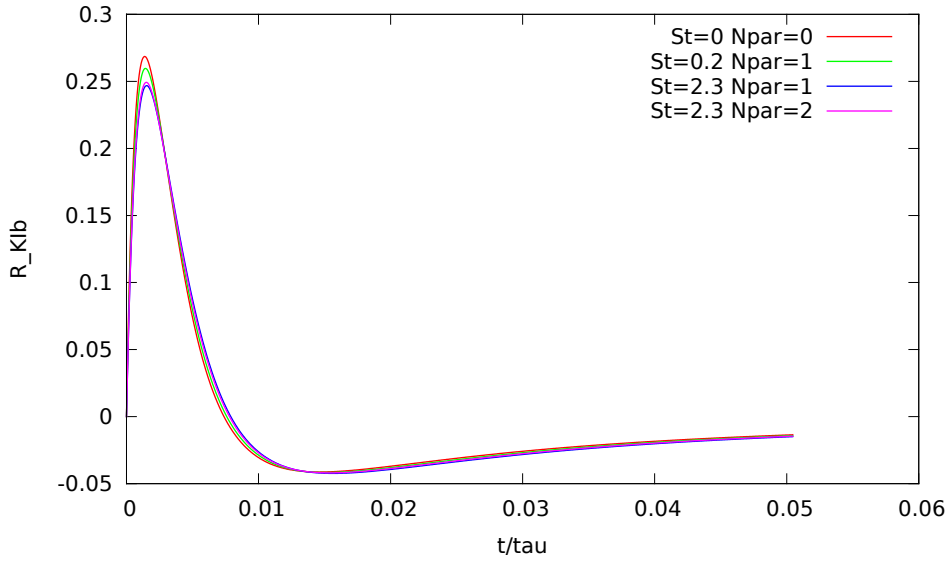

Figure 29: Normalized emission means for all four different cases.

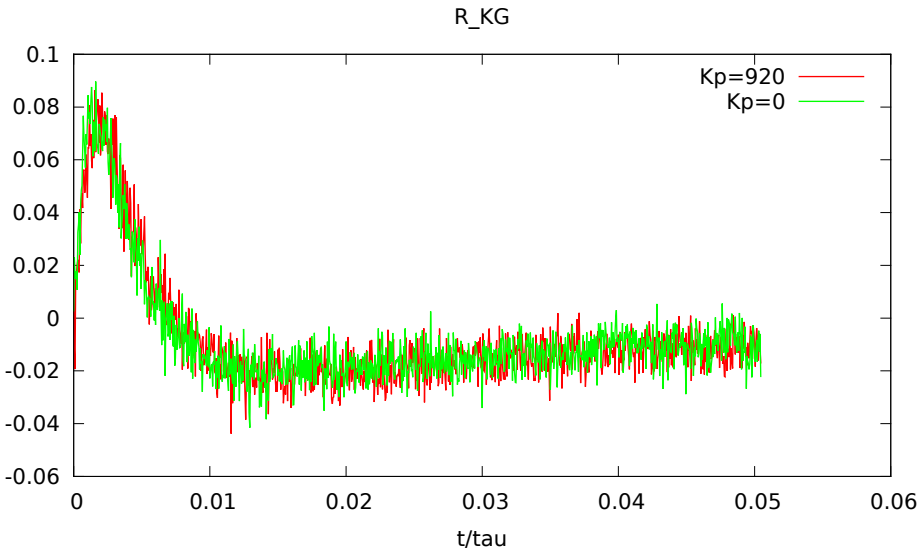

Figure 30: Normalized absorption means for the cases with the greatest difference in other means

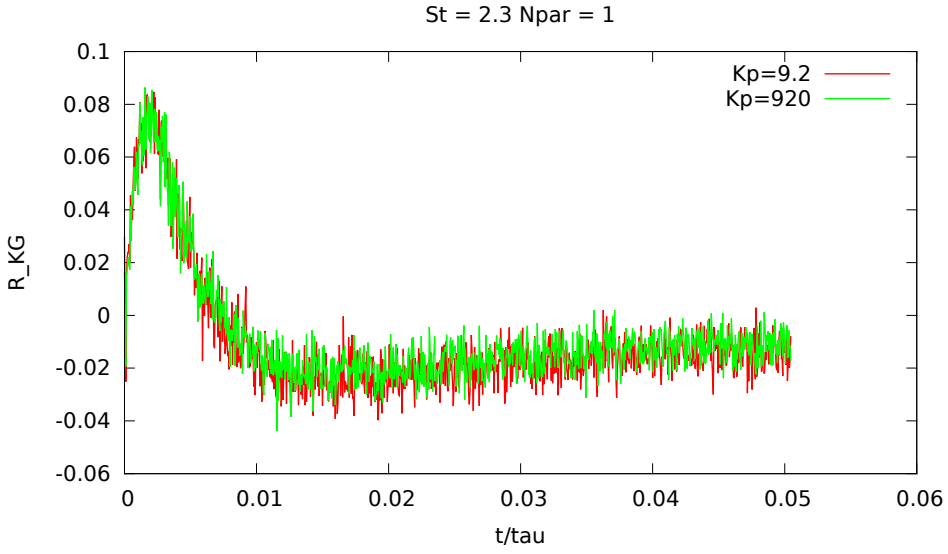

Figure 31: Normalized absorption means for thick versus thin particulate

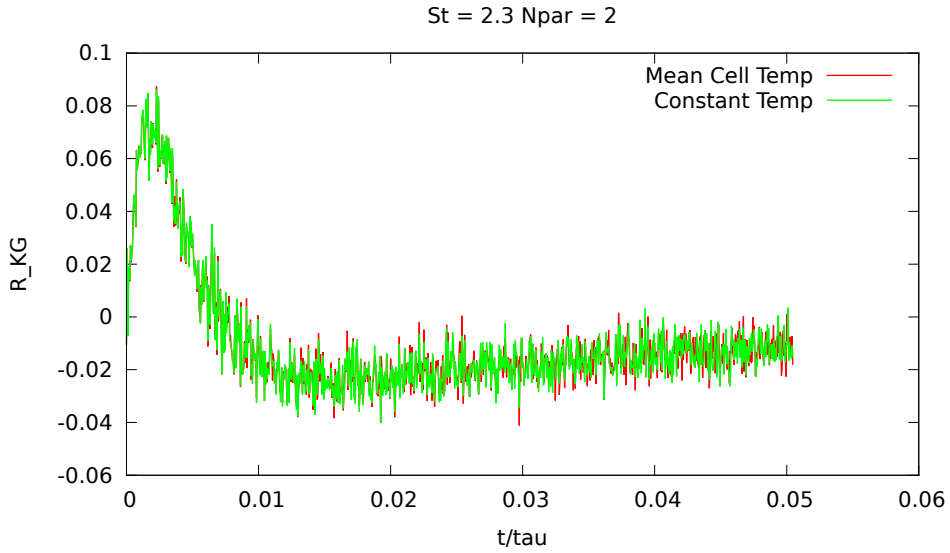

Figure 32: Normalized absorption means for constant particulate temperature versus particulate temperatures at the mean cell temperature

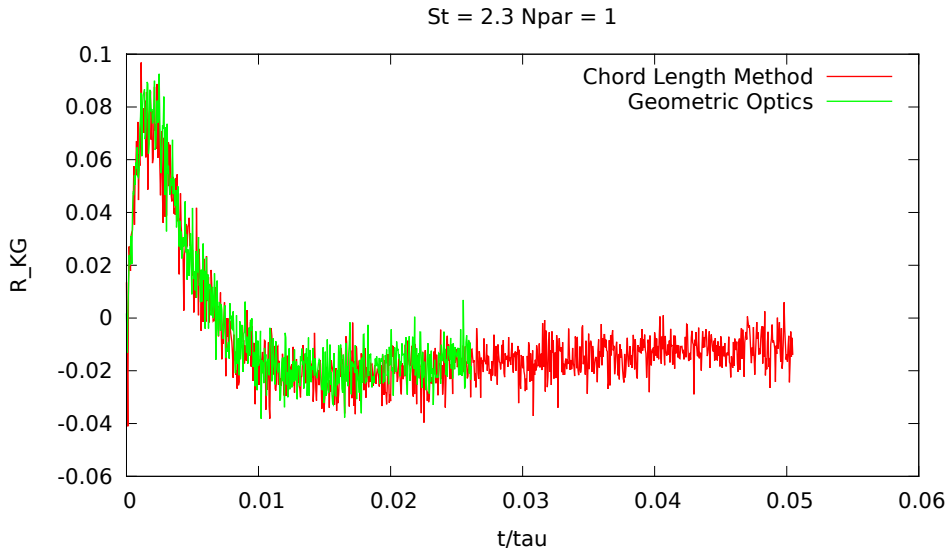

Figure 33: Normalized absorption means for constant particulate temperature versus particulate temperatures at the mean cell temperature

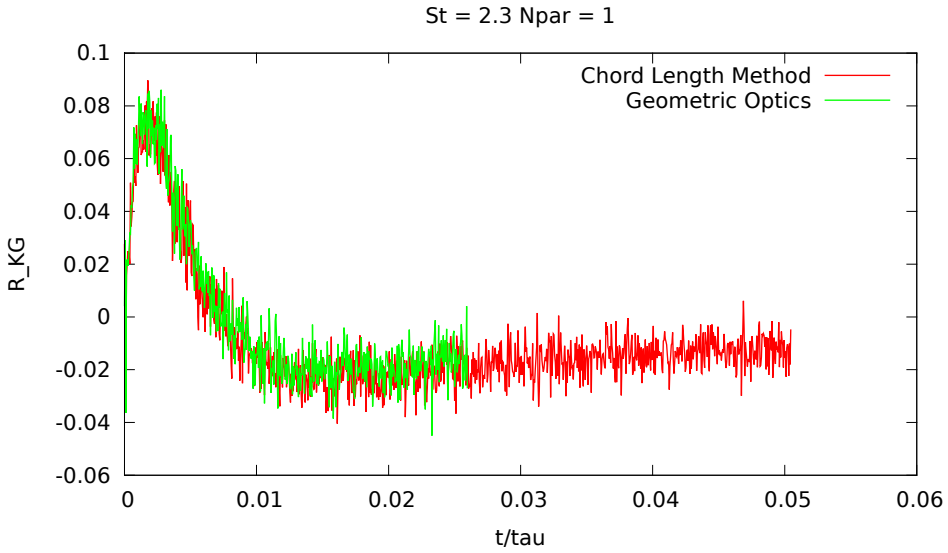

Figure 34: Normalized absorption means for constant particulate temperature versus particulate temperatures at the mean cell temperature.

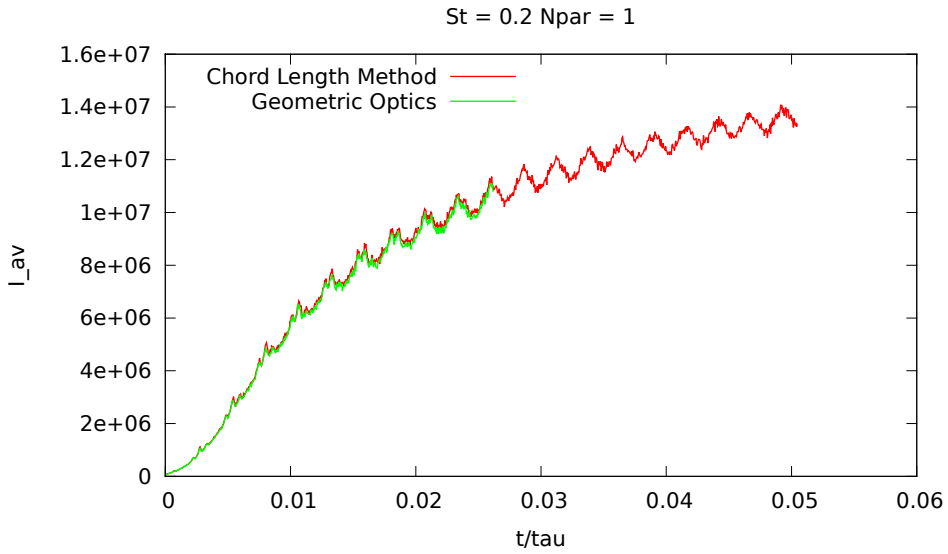

Figure 35: Mean photon intensity obtained using geometric optics versus the chord length method for St=0.2

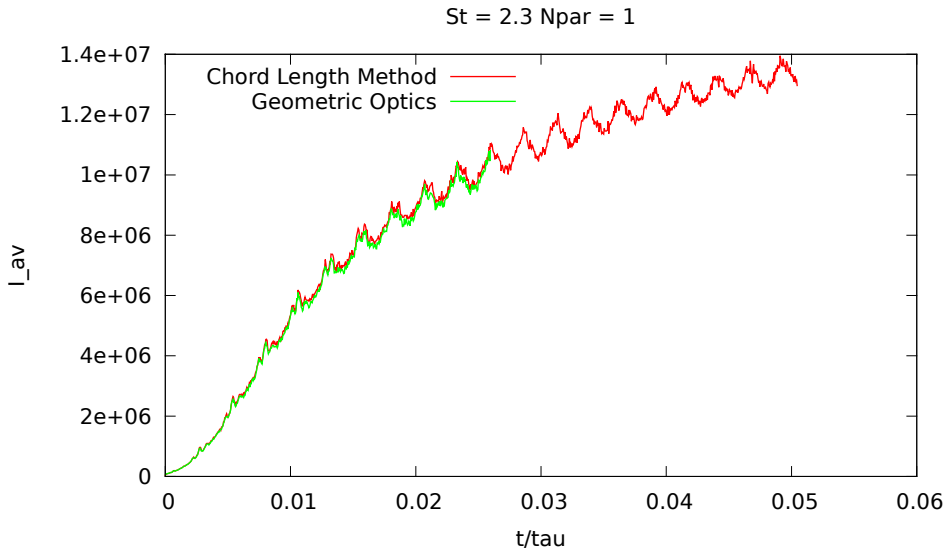

Figure 36: Mean photon intensity using geometric optics versus the chord length method for St=2.3

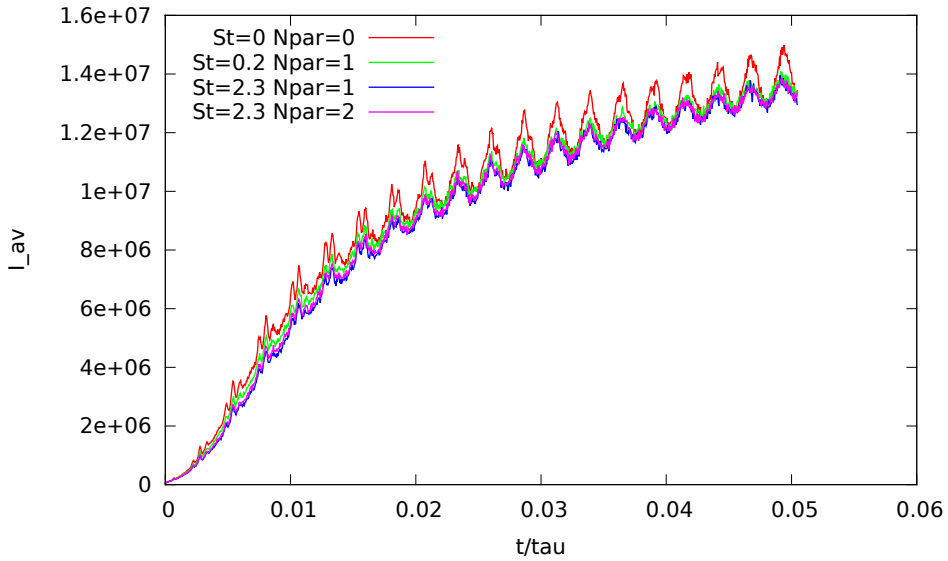

Figure 37: Mean photon intensity for all for problem initializations

6.3.5 TRI conclusions

This section shows the dependence of TRI effects on the addition and treatment of coal particulate. It should be noted that the pure gas TRI effects shown in this work do not match the scales shown by Deshmukh et al. [4]. This is related to the process used to initially populate the domain, and the overall larger spatial domain (96^3 vs. 64^3). This will be discussed in greater detail in the conclusions section.

6.4 Approximate Second Order Temporal Integration

The problem used to test the coarse mesh finite differencing scheme is the same Su and Olson test problem previously used to compare the parallel efficiencies of the two different opacity models. This benchmark was chosen because it is a transient and frequency dependent problem that requires the solution of the equation of state. This test problem also has a semi-analytic diffusion and transport solution that can be used to verify both portions of the CMFD scheme separately.

6.4.1 CMFD test case

The test problem is a cube with a non-dimensional length of 10. A reflecting boundary is placed on the x-coordinate boundary surface nearest the volume emission source, and a vacuum boundary is placed at opposite x-coordinate boundary surface. All other faces are treated as periodic boundaries. The mesh ($80 \times 2 \times 2$) contains 80 equally spaced cells in the x direction and the final results are averaged over other two dimensions.

The general transport solution was generated at 10 specified grid points (see Table 13) via a Maple subroutine, originally created and used by Nick Myers [53], that solves the semi-analytic integral provided by Su and Olson [48].

Su Olson Benchmark	
Non-Dimensional Length	Non-Dimensional Material Energy
0.0625	2.0332
1.0625	0.67392
2.0625	0.21326
3.0625	0.08604
4.0625	0.04137
5.0625	0.02094
6.0625	0.01027
7.0625	0.00457
8.0625	0.00165
9.0625	0.00034

Table 13: The semi-analytic non-dimensional material energy (T^4/T_0^4) at 10 different grid points at non-dimensional time $\tau = 10$

The order of convergence of the diffusion solver is tested for both temporal integration schemes - Backward Euler and Crank-Nicholson. A base solution was generated via the Crank-Nicholson method using 64 time steps. This will be used as the base case to determine the order of accuracy.

Diffusion via backward Euler			
# of Time Steps	L_∞	L_1	L_2
1	5.938e-1 ± 1.71e-6	3.616e-1 ± 1.33e-7	4.497e-2 ± 1.43e-9
2	4.542e-1 ± 1.62e-6	2.563e-1 ± 1.26e-7	3.262e-2 ± 2.62e-9
4	3.097e-1 ± 1.45e-6	1.624e-1 ± 1.16e-7	2.114e-2 ± 5.73e-9
8	1.903e-1 ± 1.19e-6	9.451e-1 ± 9.87e-8	1.251e-2 ± 1.38e-8
16	1.085e-1 ± 9.64e-7	5.224e-1 ± 8.34e-8	6.984e-3 ± 3.65e-8
32	5.815e-2 ± 9.13e-7	2.743e-1 ± 7.92e-8	3.690e-3 ± 1.24e-7

Table 14: The L_∞, L_1 and L_2 norms of the relative error for the diffusion solution using a backward Euler time discretization

Diffusion via Crank-Nicholson			
# of Time Steps	L_∞	L_1	L_2
1	1.878e-1 ± 2.33e-7	8.797e-2 ± 9.52e-8	1.161e-2 ± 8.05e-9
2	7.440e-2 ± 9.48e-7	4.248e-2 ± 7.57e-8	4.922e-3 ± 5.87e-8
4	2.766e-2 ± 6.56e-7	1.193e-2 ± 5.62e-8	1.453e-3 ± 5.56e-7
8	6.316e-3 ± 5.05e-7	3.549e-3 ± 4.55e-8	4.273e-4 ± 4.98e-6
16	1.867e-3 ± 4.43e-7	1.244e-3 ± 4.10e-8	1.467e-4 ± 3.69e-5
32	1.124e-3 ± 4.60e-7	8.808e-4 ± 4.03e-8	1.032e-4 ± 7.44e-5

Table 15: The L_∞, L_1 and L_2 norms of the relative error for the diffusion solution using a Crank-Nicholson time discretization

6.4.2 CMFD test results

Tables 14 and 15 show the different norms associated with the backward Euler and Crank-Nicholson time discretizations, respectively. The standard deviations are associated with numerical roundoff errors that occur in the simulation and, in this case, are well below values of interest.

Figure 38 shows the diffusion solution with 64 time steps (the base case). The lines represent the solution obtained from the scalar solver and the points represent the semi-analytic diffusion solution provided by Su et al. [48].

An Implicit Monte Carlo solver was implemented as described by Fleck et al.

Transport via IMC			
# of Time Steps	L_∞	L_1	L_2
1	4.443 ± 1.12e-1	1.203 ± 2.68e-2	5.449e-1 ± 3.59e-4
2	2.901 ± 7.98e-2	8.906e-1 ± 2.19e-2	3.669e-1 ± 5.70e-4
4	1.283 ± 7.67e-2	5.833e-1 ± 2.37e-2	2.144e-1 ± 1.52e-3
8	8.951e-1 ± 1.18e-1	4.318e-1 ± 2.85e-2	1.563e-1 ± 3.54e-3
16	8.142e-1 ± 1.33e-1	2.518e-1 ± 2.92e-2	1.103e-1 ± 9.48e-3
32	7.273e-1 ± 1.33e-1	2.295e-1 ± 7.22e-2	9.702e-2 ± 1.82e-2

Table 16: The L_∞, L_1 and L_2 norms of the relative errors for the transport solution solved via Implicit Monte Carlo

[6]. This solver was implemented to compare the rate of convergence obtained via the linearized first order approximation of the emission source with that of the new CMFD approach. Figure 39 shows the results from the IMC solver (lines) using 32 time steps as compared to the results presented by Su et al. [48] (points).

Table 16 shows the norms of the relative errors (evaluated against the points in Table 13) for various time step sizes. Note the standard deviation is significantly larger for than that observed from the scalar solver. This is a result the numerical noise associated with the Monte Carlo method. These runs used 1000 particle histories per time step with a minimum of 5 Monte Carlo particles per cell source term.

Table 17 shows the norms of the relative error for various numbers of particle histories. For all of these runs 32 time steps were used and a minimum of 5 Monte Carlo particles were assigned per cell source term.

Four outer CMFD iterations were used for all simulations presented in Tables 18 and 21. These simulations also used 1000 histories per time step with a minimum of five per cell source term. The only exception is the "32_fine" simulation presented in Table 21 which used 5000 particle histories per time step with a minimum of 10

Transport via IMC			
# MC Histories	L_∞	L_1	L_2
1000	7.273e-1 ± 1.33e-1	2.295e-1 ± 7.22e-2	9.702e-2 ± 1.82e-2
5000	7.492e-1 ± 3.27e-1	2.264e-1 ± 5.32e-2	9.950e-2 ± 2.73e-2
10000	6.595e-1 ± 1.64e-1	2.001e-1 ± 5.05e-2	8.785e-2 ± 2.06e-2

Table 17: The L_∞, L_1 and L_2 norms of the relative error for the transport solution solved via Implicit Monte Carlo with varying number of Monte Carlo histories

Transport via CMFD with Euler			
# of Time Steps	L_∞	L_1	L_2
1	9.525e-1 ± 2.58e-1	5.591e-1 ± 9.98e-2	1.950e-1 ± 8.98e-3
2	8.981e-1 ± 1.27e-1	4.031e-1 ± 4.00e-2	1.623e-1 ± 5.26e-3
4	8.620e-1 ± 5.41e-2	3.371e-1 ± 3.77e-2	1.389e-1 ± 5.85e-3
8	7.909e-1 ± 7.61e-2	2.516e-1 ± 3.40e-2	1.112e-1 ± 7.18e-3
16	6.995e-1 ± 1.00e-1	1.750e-1 ± 2.66e-2	8.581e-2 ± 1.21e-2
32	6.624e-1 ± 2.17e-1	1.701e-1 ± 6.06e-2	7.751e-2 ± 3.48e-2

Table 18: The L_∞, L_1 and L_2 norms of the relative error for the transport solution solved via CMFD with a backward Euler discretization

per cell source term. Table 18 shows the results for the CMFD method evaluated using the backward Euler discretization. Table 21 shows the results for the CMFD method evaluated with the Crank-Nicholson discretization.

Tables 19 and 22 show the norms for different numbers of histories per time step. A total of 32 time steps were used for all simulations in these tables with 1 CMFD iteration and a minimum of 5 particle histories per cell source term.

Tables 20 and 23 show the norms for different numbers of CMFD iterations. A total of 1000 histories per time step were used with 32 time steps and a minimum of 5 particle histories per cell source term.

Tables 24 and 25 show the figure of merit (one over the total calculation time multiplied by mean relative error) associated with the Monte Carlo history and

Transport via CMFD with Euler			
# MC Histories	L_∞	L_1	L_2
1000	7.834e-1 ± 1.43e-1	2.644e-1 ± 5.98e-2	1.182e-1 ± 1.67e-2
5000	6.687e-1 ± 1.86e-1	1.802e-1 ± 5.39e-2	9.027e-2 ± 3.00e-2
10000	7.503e-1 ± 3.66e-1	2.235e-1 ± 5.08e-2	1.012e-1 ± 2.91e-2

Table 19: The L_∞, L_1 and L_2 norms of the relative error for the transport solution solved via CMFD and the backward Euler discretization

Transport via CMFD with Euler			
# CMFD Iter.	L_∞	L_1	L_2
1	7.834e-1 ± 1.43e-1	2.644e-1 ± 5.98e-2	1.182e-1 ± 1.67e-2
2	6.930e-1 ± 1.73e-1	2.039e-1 ± 5.94e-2	9.199e-2 ± 2.40e-2
4	6.624e-1 ± 2.17e-1	1.701e-1 ± 6.06e-2	7.751e-2 ± 3.48e-2
8	7.212e-1 ± 1.96e-1	2.132e-1 ± 5.52e-2	9.396e-2 ± 2.03r-2

Table 20: The L_∞, L_1 and L_2 norms of the relative error for the transport solution solved via CMFD and the backward Euler discretization

Transport via CMFD with Crank-Nicholson			
# of Time Steps	L_∞	L_1	L_2
1	7.637e-1 ± 1.61e-1	2.727e-1 ± 4.52e-2	1.098e-1 ± 1.32e-2
2	7.019e-1 ± 2.83e-1	1.746e-1 ± 5.35e-2	8.452e-2 ± 3.53e-2
4	6.543e-1 ± 5.21e-2	1.482e-1 ± 2.80e-2	7.483e-2 ± 1.13e-2
8	4.806e-1 ± 8.32e-2	1.314e-1 ± 2.38e-2	5.771e-2 ± 2.46e-2
16	4.662e-1 ± 1.54e-1	1.454e-1 ± 3.71e-2	6.442e-2 ± 3.35e-2
32	2.823e-1 ± 1.44e-1	1.126e-1 ± 7.59e-2	4.714e-2 ± 1.48e-1
32_fine	2.371e-1 ± 1.44e-1	6.182e-2 ± 3.66e-2	2.877e-2 ± 1.63e-1

Table 21: The L_∞, L_1 and L_2 norms of the relative error for the transport solution solved via CMFD using the Crank-Nicholson discretization

Transport via CMFD with Crank-Nicholson			
# MC Histories	L_∞	L_1	L_2
1000	3.039e-1 ± 3.90e-1	9.877e-2 ± 9.06e-2	4.14e-2 ± 2.12e-1
5000	3.749e-1 ± 3.53e-1	1.187e-1 ± 5.12e-2	4.91e-2 ± 1.17e-1
10000	3.731e-1 ± 2.07e-1	9.633e-2 ± 4.33e-2	4.74e-2 ± 8.58e-2

Table 22: The L_∞, L_1 and L_2 norms of the relative errors for the transport solution solved via CMFD using the Crank-Nicholson discretization

Transport via CMFD with Crank-Nicholson			
# CMFD Iter.	L_∞	L_1	L_2
1	3.039e-1 ± 3.90e-1	9.877e-2 ± 9.06e-2	4.144e-2 ± 2.12e-1
2	4.689e-1 ± 1.84e-1	8.666e-2 ± 6.30e-2	5.120e-2 ± 7.57e-2
4	2.823e-1 ± 1.44e-1	1.126e-1 ± 7.59e-2	4.714e-2 ± 1.49e-1
8	2.579e-1 ± 3.51e-1	1.112e-1 ± 6.70e-2	4.521e-2 ± 1.28e-1

Table 23: TheL_∞, L_1 and L_2 norms of the relative errors for the transport solution solved via CMFD with the Crank-Nicholson discretization

CMFD iteration refinements, respectively.

Figure 40 shows the 32 time step CMFD solution and the Su and Olson results. This includes both the analytic values determined at the grid points shown in Table 13 and the original data presented by Su et al. [48].

Figures 41 and 42 show the refinement cases for the diffusion solver using the backward Euler and the Crank-Nicholson discretizations, respectively. Figure 43

Figure of Merit for CMFD Iterations		
# CMFD Iter.	Crank	Euler
1	4.0e-3	1.5e-3
2	2.3e-3	9.4e-4
4	9.0e-4	5.7e-4
8	4.5e-4	2.3e-4

Table 24: Figure of merit for CMFD iteration refinement

Figure of Merit for MC Histories			
# MC Histories	CMFD-CN	CMFD-Euler	IMC
1000	4.0e-3	1.5e-3	1.8e-3
5000	1.5e-3	9.7e-4	7.9e-4
10000	9.9e-4	4.3e-4	4.8e-4

Table 25: Figure of merit for number of Monte Carlo History refinement

shows the temporal refinement cases for the IMC transport solver. Figures 44 and 45 show the temporal refinement results for the CMFD solver using the backward Euler and Crank-Nicholson discretizations, respectively. Each figure plots the normalized material energy (T^4/T_0^4) evaluated by the respective solvers (lines) compared to the analytic results (points). The base time step used in these refinements is $dt = 10$. The time step sizes in the refinement study are indicated by dt/N where N is some integer value defining the number of time steps used during the simulation.

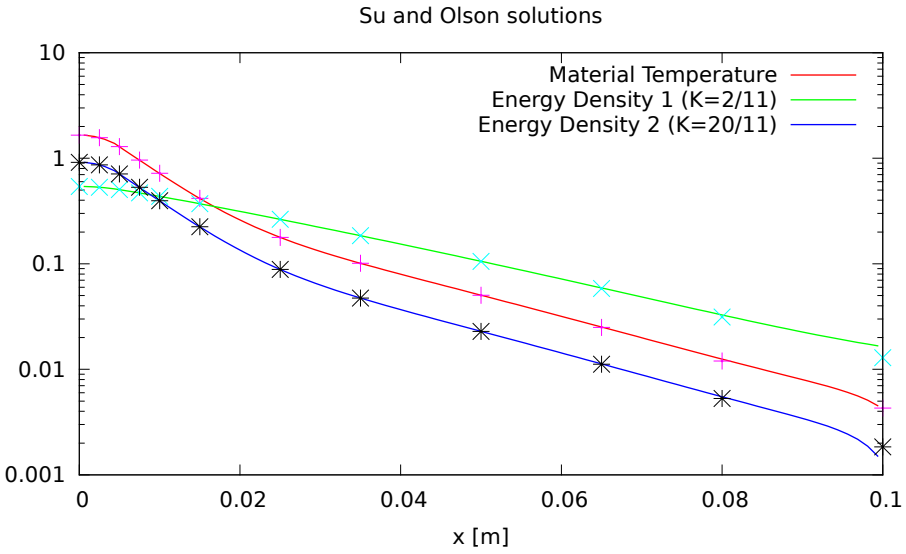

Figure 38: Scalar diffusion solver compared to Su and Olson's semi-analytic result.

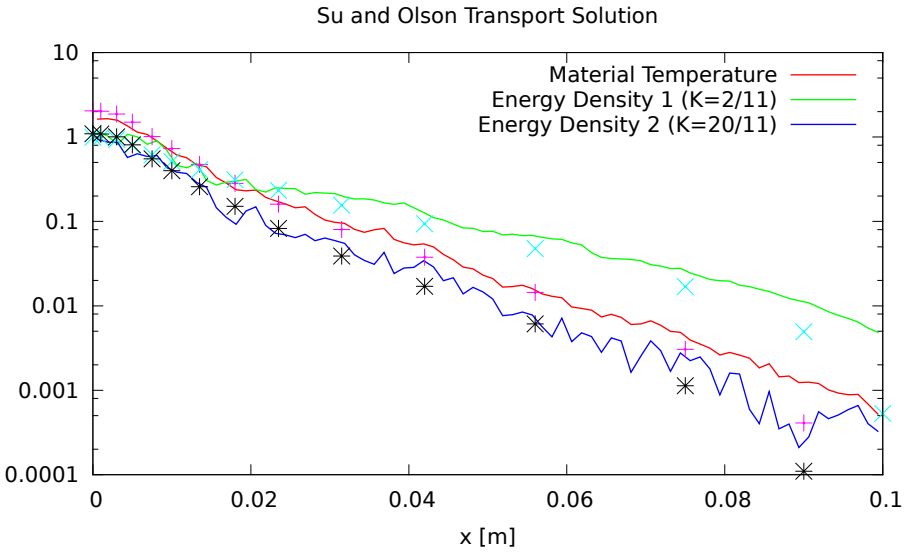

Figure 39: IMC solution using 32 time steps compared to Su and Olson's semi-analytic result.

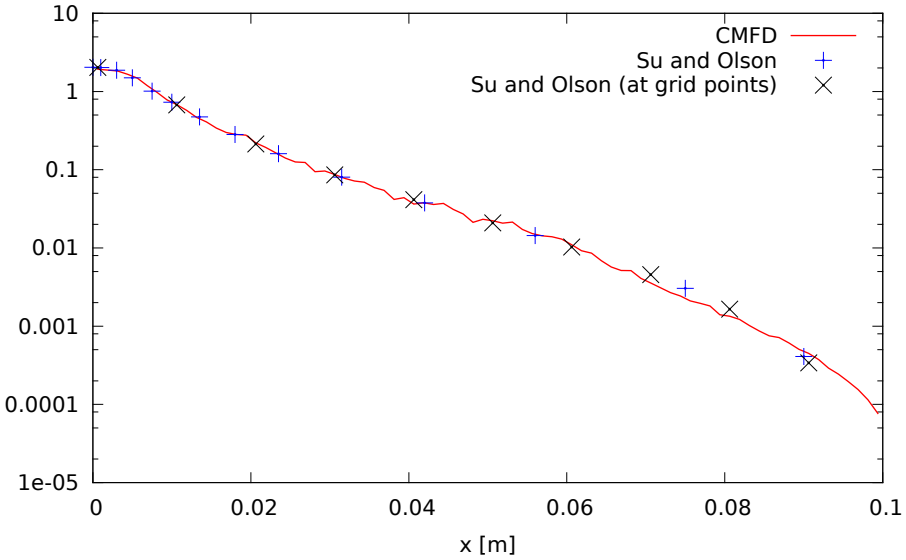

Figure 40: Normalized material energy (T^4/T_0^4) evaluated using 32 time steps with the CMFD solver compared against the Su and Olson analytic data

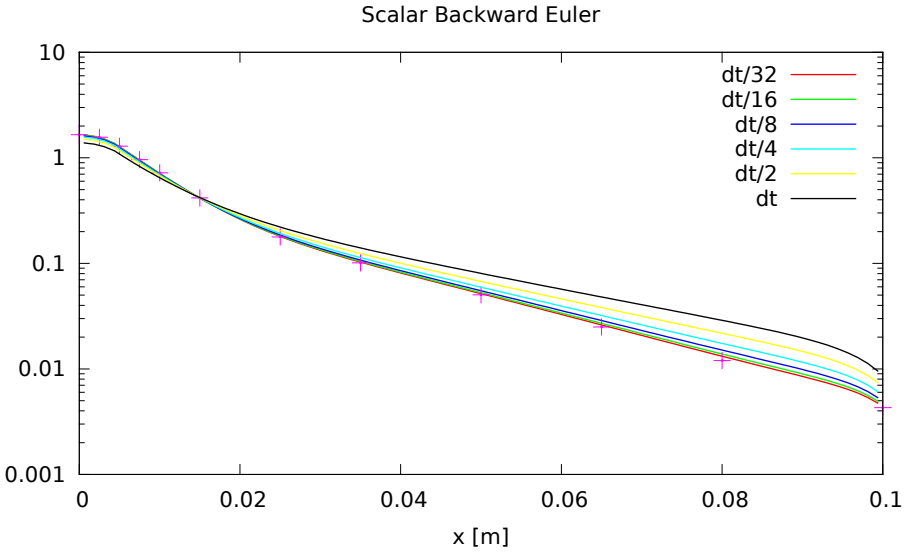

Figure 41: Normalized material energy (T^4/T_0^4) evaluated using different time steps with the diffusion solver using the backward Euler temporal integration scheme compared against the Su and Olson analytic data

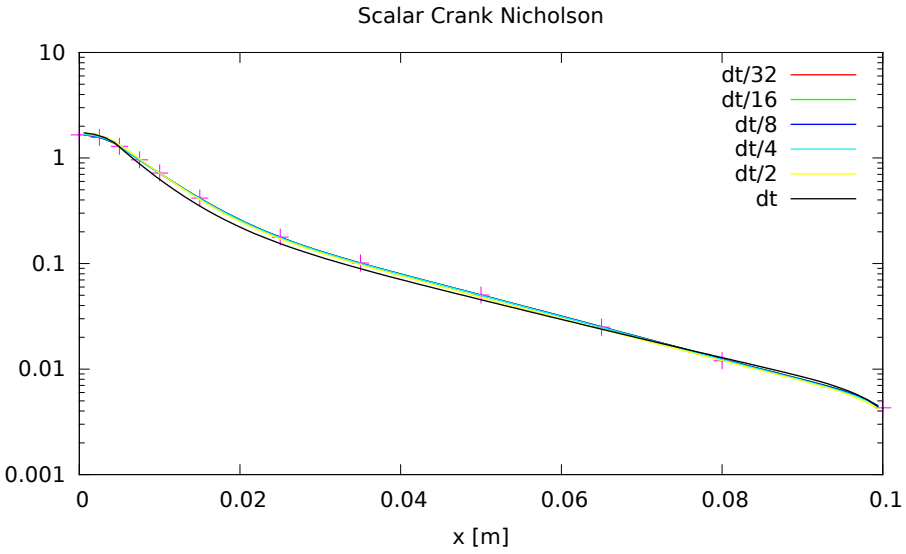

Figure 42: Normalized material energy (T^4/T_0^4) evaluated using different time steps with the diffusion solver using the Crank-Nicholson temporal integration scheme compared against the Su and Olson analytic data

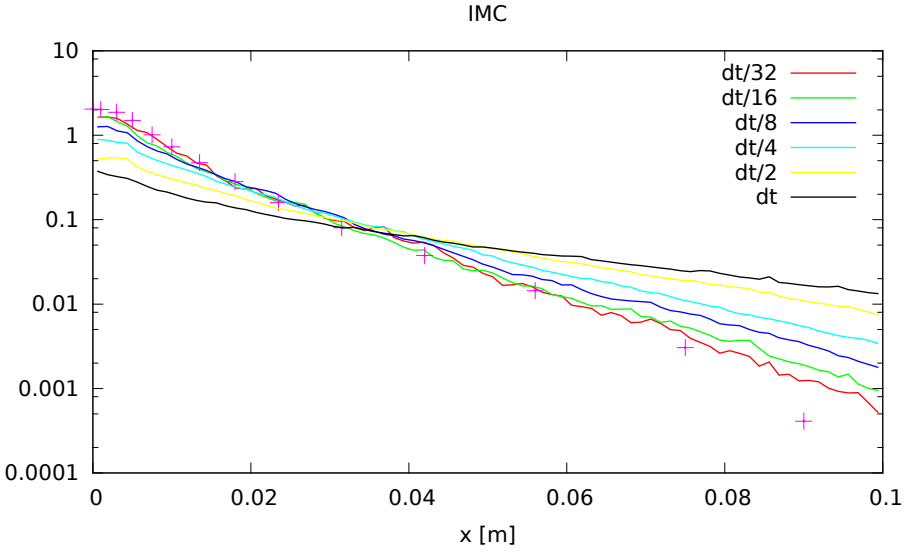

Figure 43: Normalized material energy (T^4/T_0^4) evaluated using different time steps with the IMC solver compared against the Su and Olson analytic data

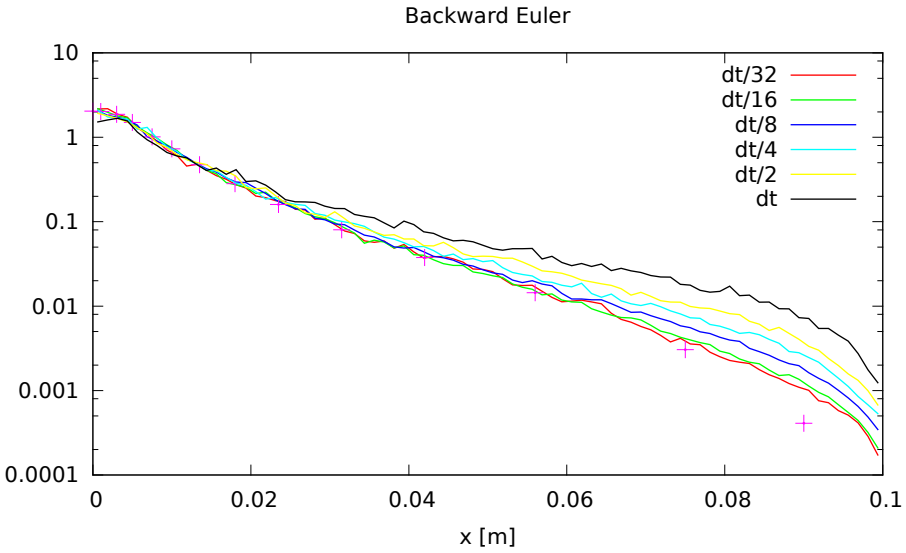

Figure 44: Normalized material energy (T^4/T_0^4) evaluated using different time steps with the CMFD solver using the backward Euler temporal integration scheme compared against the Su and Olson analytic data

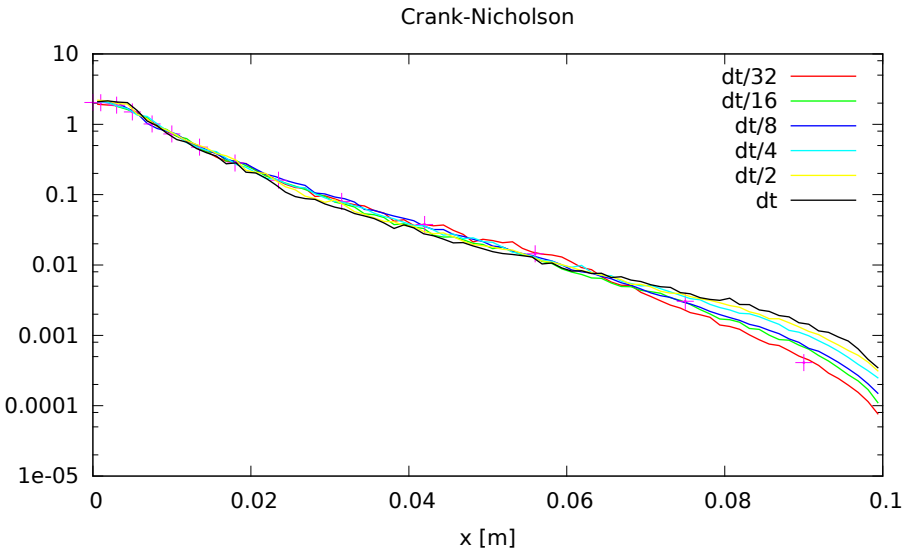

Figure 45: Normalized material energy (T^4/T_0^4) evaluated using different time steps with the CMFD solver using the Crank-Nicholson temporal integration scheme compared against the Su and Olson analytic data

Figure 46 is a log-log plot of the infinity norms of the relative errors ($|\epsilon(x)|_\infty$)associated with the different temporal refinements. The log-log plot shown in Figure 47 shows the L_1 norms ($|\epsilon(x)|_1$) of the relative errors for the different temporal refinement methods. The L_2 norms ($|\epsilon(x)|_2$), Figure 48, are shown on a log-log plot for the different methods.

Figure 49, 50, and 51 show the standard deviations associated with the means listed in the tables of norms.

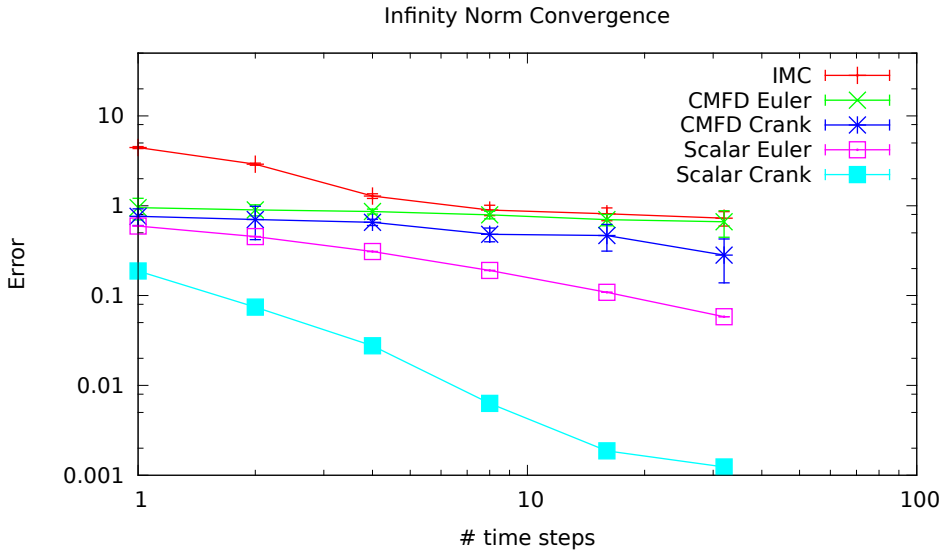

Figure 46: The L_∞ norms at different numbers of time steps for the different temporal integration approaches

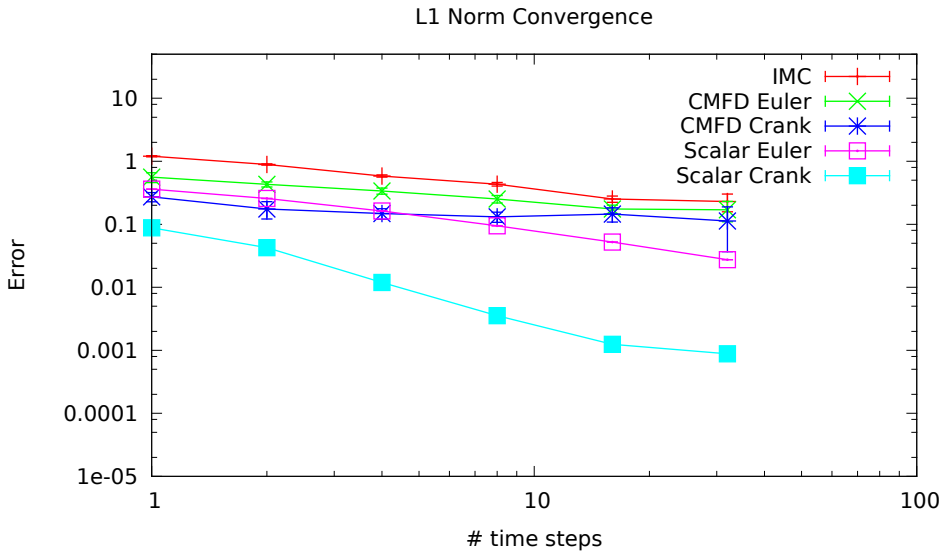

Figure 47: The L_1 norms at different numbers of time steps for the different temporal integration approaches

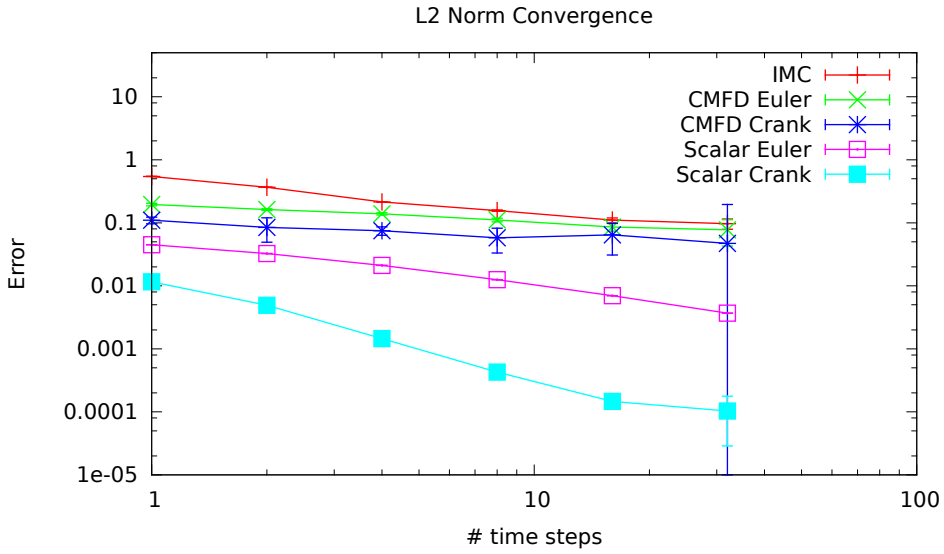

Figure 48: The L_2 norms at different numbers of time steps for the different temporal integration approaches

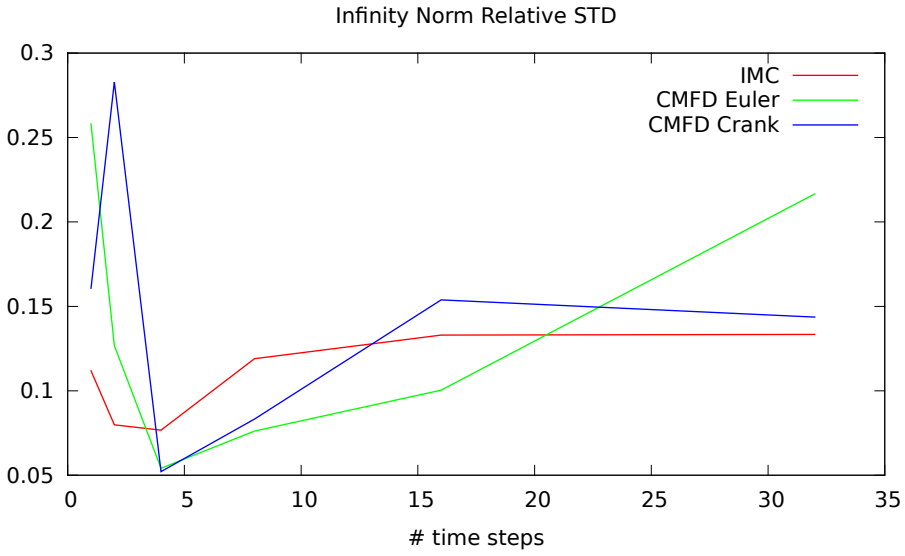

Figure 49: Standard deviations of the L_∞ norms

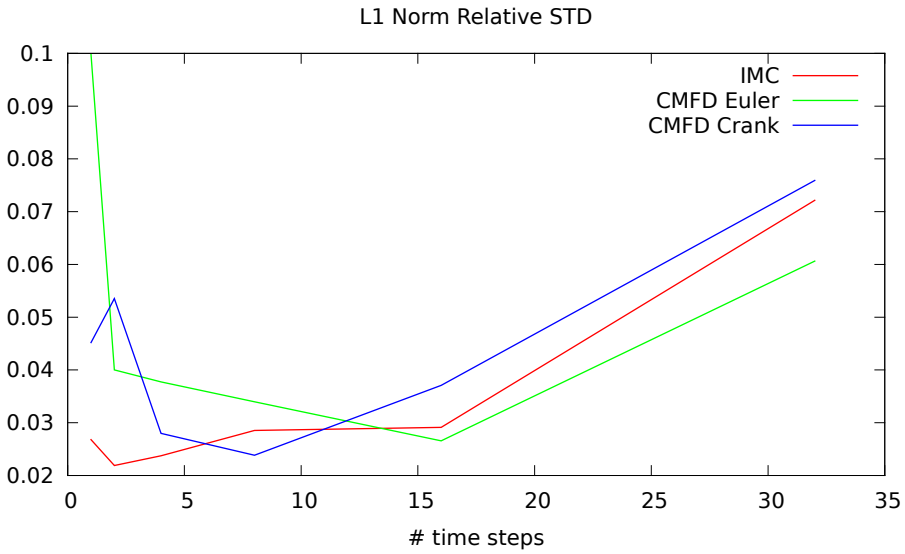

Figure 50: Standard deviations of the L_1 norms

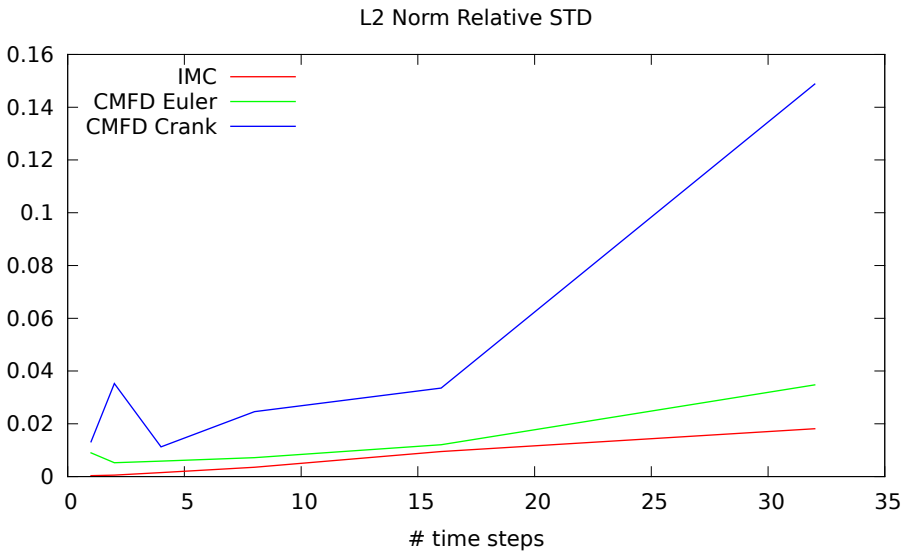

Figure 51: Standard deviations of the L_2 norms

6.4.3 CMFD results summary

This section shows the convergence rates, as measured in three different norms, for the different approaches to evaluating the non-linear emission source term. The standard deviation associated with the norms of the error is also calculated. These norms and their associated standard deviations will be used to draw conclusions about the accuracy and convergence of the CMFD approach, with both the backward Euler and the Crank-Nicholson temporal discretizations, as compared to the standard Implicit Monte Carlo approach.

7 Conclusions

7.1 Gas Opacity Model Comparisons

We have investigated the solution of the frequency dependent Su and Olson problem using two different opacity models. The two chosen in this work are the Spectral-Line-Based weight sum of grey gasses and the Line-by-Line opacity models. These models were chosen because the Line-by-Line model is the most accurate and robust model available to date and the SLW model is a coarse representation of a broad spectrum of K-distribution methods commonly used in combustion applications. Figure 6 shows good agreement between the SLW and LBL models. The overheating is most likely associated with the large explicit time steps.

The parallel efficiency of these models was determined using the Su and Olson frequency dependent test problem [48]. This test problem was chosen because it can be modified to be representative of a realistic gas system, while still providing an analytic solution to verify the results. This test problem is also advantageous because the SLW model will be just as accurate as the LBL model. This is because the mock picket fence opacity employed can be represented exactly with two opacities and the correlated K-distribution assumption is exact. The correlated K-distribution assumption specifies that the frequencies associated with the opacities in one cell can be correlated to frequencies associated with a different opacity in all the other cells. This assumption is true for this test problem because the opacity associated with a particular frequency is the same in all cells. As a result, all remaining differences between the methods are likely associated with numerical differences and roundoff errors.

The first and most obvious conclusion that can be drawn from the comparison of the two opacity models is that the overall speed of the LBL opacity model is faster than the SLW model in all cases. This has been documented and evaluated by Wang and others [14, 2]. The work of Pal et al. even shows that the LBL model out-performs the K-distribution method in evaluation time for a single parallel run [2].

Scaling studies are important because they provide information about how a method is expected to perform as it is used in an increasingly parallel computing environment. A good example of this is the results of the history scaling study. All cases in the history study use the same number of processors. For the 1x run (4.0e4 particle histories), the LBL model is $\tilde{5}3\%$ faster than the SLW model, as compared to the 16x run (6.4e5 particle histories) which is only 25% faster. In fact, because the computational time associated with a particle history should be shorter for the SLW model than the LBL model, the SLW model will eventually overtake the LBL model in overall computational efficiency. The calculation time of a particle history for the LBL model is longer than the SLW model because of the need to interpolate the opacity tables each time a particle enters a new cell. The SLW model, on the other hand, reduces this evaluation time during the particle history by pre-computing the gray-gas opacity tables, which can easily be stored in memory for quicker access. This is evident in Figure 9, which shows the total run time divided by the total number of histories per time step. As the number of histories increases, the associated cost per history of the SLW model rapidly decreases. This is not the case for the LBL method, which stays relatively constant. This pre-computation step is very expensive and its cost can be directly correlated to the number of cells in the system. The SLW model, and other global models like it, are often used in

conjunction with a deterministic solver. In this research, we used a Monte Carlo solver to avoid the need to evaluate the differences in numerical accuracy between the two approaches. Other potential tradeoffs could may exist between these two opacity methods with the use of deterministic solvers. Deterministic solvers are less sensitive to parallel load imbalance, and are generally considered to be faster than Monte Carlo solvers. This would require a more rigorous comparison of accuracy to determine the overall figure of merit.

Weak scaling efficiency demonstrates the effect on computational cost of a numerical method as the number of processors is scaled with the size of the problem. We expect that the SLW model should perform better with this scaling than the LBL model. This is because it is less sensitive to load imbalance, as the majority of calculation time occurs during the preprocessing step and scales as the number of cells in the problem. The LBL method, where the majority of computational cost is history-based, is more sensitive to load balancing issues which drive down the weak scaling efficiency. Figure 8 shows how weak scaling efficiency of the LBL model rapidly declines as compared to the SLW model which stays relatively flat.

Strong scaling efficiency shows how the computational cost is affected as more processors are added to the same problem size. It would be expected that the SLW model will out perform the LBL model again, because changing the number of processors does not change where the majority of the computational time will be performed. The SLW model, however, should scale very well because the associated cost is based on the number of cells, not where the particle histories take place. This is verified in Figure 7 which shows that the strong scaling efficiency of the SLW model is relatively flat compared to the LBL model.

The relative load imbalance, shown in Figures 10 and 11, is the driving factor

which affects the scaling efficiency for these methods. The imbalance shown in this work is sensitively dependent on the physics of the chosen test problem. In the Su and Olson picket fence problem, the majority of the heating occurs in a small portion of the problem. The Monte Carlo solver randomly selects particles based on the relative weight of the source in each cell. This results in many particle histories in the hot region of the problem and only a few in the cold. This non-uniform heating is commonly found in coal furnaces that can have large gradients in temperature between the combusting flame and the burner wall. Domain replication can greatly improve the scaling performance of the LBL method. Because of memory limitations, however, some domain decomposition must be performed in almost all problems of interest. Beyond domain replication, there are other load balancing approaches that could be applied to help improve the parallel scaling of the LBL model. Any of these approaches could also be applied to the SLW model to help increase performance. Domain replication for the SLW model could potentially assign individual processors to compute only a portion of the domain, which is shared amongst them. A more efficient table lookup procedure could greatly improve the performance of the LBL model. A more efficient method of computing the gray gas properties during the preprocessing step could also be investigated for the SLW model.

7.2 Turbulent Radiation Interactions in Particulate Laden Flows

Deshmukh et al. [4] developed a numerical test case that could be used to evaluate the sensitivity of turbulent radiation interactions to a variety of parameters. We have expanded upon this test case to determine the sensitivity of TRI to the addition of coal-type particulate. Other particulate, such as fly ash and char,

have been extensively studied and have been shown to strongly affect mean flame temperatures and radiative heat fluxes [16, 34].

Coal particulate is more sensitive to flow regimes than smaller particulate, such as fly ash and char, because of its relative size and momentum. To evaluate the effect of the presence of coal particulate on overall TRI, two simulations with different Stokes numbers were performed (St=2.3 and St=0.2). Because the particulate density will also vary in combustion applications, two packing fractions were considered (9.6e-2% and 1.9e-1%). The initial particle clustering in each of these simuations is evident in Figures 15, 16, and 17. These figures show thin slices of the spatial domain, and every dot represents a single particle location, with the exception of Figure 17, where every dot represents two particulate spheres. At low Stokes numbers, clustering begins to occur and as the Stokes number is increased beyond 1, collisions begin to push the particulate back into the eddies which originally pushed them out.

Because the smoothing filter was not applied to the initialization of the material distribution, the rate of product build-up is much faster than in the work of Deshmukh et al. [4]. This is evident from a plot of the fuel distribution after one time step (Figure 18). In fact, the fuel is almost completely combusted after the non-dimensional time of 0.05 (see Figure 19). The mixture fraction is the driving parameter for the radiative transfer equations in this problem. Figure 20 shows a slightly different progression of the mixture variance as a function of time for each of the initializations. This likely relates directly to the initial kinetic energy in the system before it is populated with fuel, and before the turbulence is allowed to decay. The differences in the decay rates of the mixture variance are observed in two of the normalized TRI means (Figures 24 and 29). This is by far

the most influential parameter in the system. Therefore, any variations associated with varying Stokes numbers and packing fractions are difficult to discern from a direct comparison.

To illustrate the influence of the definition of the particulate temperature, each simulation was performed once using a constant particulate temperature (of 750[K]) and once assuming the particulate temperature is equal to the mean background medium cell temperature. Figures 21, 22, and 23 compare the normalized temperature mean (R_{T^4}) for the two different definitions of the particulate temperature. These figures show that the TRI normalized temperature mean is relatively insensitive to the particulate temperature definition. The evolution of the packing fraction is most sensitive to the definition of the particulate temperature. It is expected that as the number density and/or size of the particulate is increased, the problem will become increasingly more sensitive to the definition of particulate temperature. This is because larger and/or more clustered particulate will likely maintain lower temperatures, increasing TRI effects. Figures 25, 26, and 27 show the normalized emission mean (R_{KIb}) for all three particulate initializations with both the constant particulate temperature and mean cell particulate temperatures. This mean is even less sensitive to the definition of the particulate temperature.

Figure 28 shows the dependence of the normalized emission mean on the particulate optical thickness. This figure shows that as the particulate becomes more optically thick, the TRI effects associated with the emission term decrease. As the influence of the particulate becomes more prominent, its smoother (in this case constant) opacity means that the emission source distribution will be more consistent throughout the problem.

Statistical variance in the normalized absorption mean (R_{KG}) makes it very

difficult to quantify the effect of parameter variations. Therefore, only the simulations which should have the most significant differences (as determined by the differences in the other means) are plotted. The two most significant differences associated with the other means are the rate of reduction in mixture variance and particulate optical thickness. Figure 30 compares the normalized absorption means for the two cases that are the most different in opacity and mixture variance. Even in these cases, it is difficult to make any conclusions about the differences in the results because of the significant statistical noise in the solutions. Figures 31 and 32, comparing the differences associated with particulate thickness and temperature treatment, show some discernible differences. Making the problem thicker or treating the particulate as a constant temperature appears to reduce the statistical noise. This does show that the influence of the particulate on the optically thin eddy approximation is relatively mild. Even for the thickest particulate, the overall maxima and minima of the curves remain relatively unaffected.

Figures 33, 34, 35, and 36 compare the results using the chord length method versus geometric tracking. These show that the chord length method can reproduce the normalized means within the accuracy of the statistical noise associated with the solutions. These results also show that the chord length method slightly over-predicts the mean intensity as compared to geometric tracking. The results for geometric tracking were computed for half the number of iterations of those using the chord length method because of the increased memory requirements and computational time associated with geometric tracking.

This work shows that TRI effects are relatively insensitive to non-combusting coal-type particulate for low mass loadings. The least sensitive TRI parameter is the normalized absorption mean (or optically thin eddy approximation). As

mass loading increases and coal combustion processes are included, the TRI effects will likely be amplified. This is because the source term in the radiative transfer equation will be tightly coupled to the location and density of the particulate.

7.3 Increasing Monte Carlo Temporal Convergence Using CMFD

CMFD has been shown to be an effective source convergence acceleration technique for deterministic methods[19] and a variance reduction tool for Monte Carlo solvers [41] applied the k-eigenvalue neutron transport equations. We investigate the use of Coarse Mesh Finite Difference (CMFD) with Monte Carlo as the high-order solver applied to the radiative heat transfer equations. Our interest is in assessing the temporal order of convergence using standard IMC, CMFD using a backward Euler temporal discretization, and CMFD using a Crank-Nicholson temporal discretization.

To verify the Monte Carlo and diffusion solvers, the Su and Olson diffusion and transport solutions were generated with the appropriate solver independently. Figure 38 shows the diffusion solution with 64 time steps using Crank-Nicholson. The variation between the numerical solution and the analytic diffusion solution at the point $x = 10$ occurs because the domain is not large enough in the x direction to fully capture the semi-infinite assumption made in the analytic derivation. The domain is large enough, however, to capture the full transport solution as shown in Figure 39 with the IMC solver using 32 time steps. Both agree within the specified convergence tolerance.

The solutions from each of the transport solvers (IMC, CMFD-Euler, CMFD-CN) as a function of temporal refinement are compared against ten reference points that were evaluated with the semi-analytic integral given by Su and Olson [48]. The

temporal refinement of the diffusion solver is simply compared to a highly resolved numerical evaluation using the diffusion solver (64 time steps). The diffusion solver was evaluated using both backward Euler and Crank-Nicholson temporal integration schemes. Figures 41 and 42 compare the numerical results for the diffusion equations using different time step sizes (points represent the analytic solutio [48]) for the two different integration schemes. As expected, the second order Crank-Nicholson scheme approaches the analytic solution more rapidly than the first order backward Euler scheme. Figure 43 shows the temporal refinement of the transport solution using the IMC solver. This figure shows that the IMC approach performs very poorly at large time steps. The refinement of the CMFD approach is shown in Figures 44 and 45 for both Backward Euler and Crank-Nicholson discretizations, respectively. These plots show that while both the CMFD-Euler and IMC solver are first order accurate, the CMFD-Euler is initially more accurate. The CMFD-CN is initially more accurate than both CMFD-Euler and the IMC solvers. The rate of convergence for the CMFD methods is difficult to assess from these figures because of the statistical noise.

Typically the L_∞ norm (which is the maximum value in a vector) of the relative error is plotted on a log-log plot to numerically verify the order of accuracy of any given method. Figure 46 is the log-log plot of the infinity norm for each method. The rate of convergence, as determined by the slope of this curve, for the diffusion solver using both Crank-Nicholson ("Scalar Crank") and Backward Euler ("Scalar Euler") show convergence rates of second and first order, respectively. The refinement of the IMC solver initially shows a convergence order of less than one, which quickly flattens out for refinements beyond 8 time steps. This degradation of the convergence rate is likely related to statistical noise which becomes greater

than the numerical error associated with the temporal discretization. The slope of the L_∞ norm for the CMFD method with the Backward Euler discretization is very flat. The overall accuracy of the method is better than the IMC method for all refinements, and at 16 time steps it is more accurate than 32 time steps using IMC. The slow convergence rate of this method is also limited by numerical noise and the number of CMFD iterations used to converge the streaming operator. The CMFD method with the Crank-Nicholson discretization is more accurate than both IMC and the Backward Euler discretized CMFD method for all refinements. In fact, with only two time steps it is more accurate than the 32 time steps IMC solution and the 8 times step solution using the Backward Euler method. The CMFD-CN shows a better rate of convergence than the CMFD-Euler discretization. This indicates that the Crank-Nicholson discretization might be less limited by the statistical noise and/or the number of CMFD iterations used.

The L_1 norm relative error results are displayed on a log-log plot in Figure 47. The slopes of the mean error for the IMC and scalar Euler problems match very well, as they should, both being first-order accurate in time. The scalar Crank-Nicholson mean has a slope matching a second order accurate problem. The CMFD models show slopes that are flatter than would be expected for the known discretization error of the transport and diffusion methods. All three Monte Carlo solvers show degraded convergence behavior with decreasing time step size, which is likely related to the statistical errors associated with these methods. Figure 48 shows the L_2 norms of the relative error. This error norm helps illustrate how consistent the solution is across the spatial domain and is analogous to the standard deviation. The L_2 error norms decrease at a rate very similar to that of the L_1 norm for the scalar solvers.

The standard deviations of the original values are evaluated by averaging the results in the x-direction. These standard deviations are carried through the evaluation of the norms to illustrate the confidence in the results.

The reduced rate of convergence that was observed for small time in the CMFD and IMC methods prompted a sensitivity study. The goal was to establish the influence of the number of CMFD iterations and number of Monte Carlo histories on the accuracy of each method. Both the number of CMFD iterations and number of histories were refined independently for the 32 time step case. The results for the number of Monte Carlo histories, shown in Tables 17, 19, and 22, used 1 CMFD iteration in each simulation. These tables show that as the number of particle histories are increased for the IMC method, the norms and their standard deviations are reduced. The norms for the CMFD methods are reduced, but not consistently. The standard deviations of all the norms are reduced, as expected, because increasing the number of histories reduces statistical noise. This indicates that the accuracy of the CMFD method for is likely being limited by the accuracy of the non-converged CMFD iterations.

The sensitivity of the CMFD method to the number of CMFD iterations was tested with simulations using 32 time steps and 1000 histories per time step. This study shows an inconsistent improvement in accuracy and in standard deviation for both methods. The accuracy of the solutions in these simulations is likely being hampered by the statistical errors in the solution after each time step.

To show that as both the number of particle histories and the number of CMFD iterations are increased the accuracy of the methods improve, a refined simulation was performed. This is the "32_fine" date shown in Table 21. In this simulation, four CMFD iterations were used with 5000 histories per time step and 10 minimum

particles per cell source term for 32 time steps. This shows a small reduction in the maximum relative error and a large reduction in the mean relative error (L_1 norm).

The total figure of merit (Tables 24 and 25), as determined by the inverse of the calculation time multiplied by the mean relative error, is used to compare the methods because it helps account for the increase in computation time associated with the CMFD method. From this data, it is evident that largest figure of merit is achieved with the coarsest representation of the CMFD method at 32 time steps. Furthermore, using two CMFD iterations out-performs all other methods. To find the maximum figure of merit, a full three dimensional refinement study of time step size, number of CMFD iterations, and number of particle histories is necessary. The goal of this study is simply to highlight that such a maximum exists and that CMFD with a Crank-Nicholson discretization can out-perform IMC for these type of problems. This method would likely perform best in thick transient problems. In these problems, IMC would require many effective scattering events and small cells to reduce teleportation errors. The CMFD method will likely perform poorly in optically thin and/or strongly scattering media where the streaming operator is difficult to evaluate.

Even though this research does not show that CMFD with Crank-Nicholson is second-order accurate in time, it does show that it is more accurate and computationally efficient than the IMC method for the problem in question. A better assessment of the order of convergence may be possible with an adaptive convergence criteria for the CMFD method. Statistical noise, however, makes determining convergence difficult.

7.4 Overall Conclusions and Future Work

We have investigated three different aspects of the numerical solution of radiative heat transfer equation in application to coal combustion problems. The first is the parallel performance of two different opacity models; the Line-by-Line (LBL) model and the spectral-line-based weighted sum of grey gases (SLW) model. The second is the sensitivity of turbulent radiation interaction effects to the addition of coal-type particulate. The third is increasing the temporal order of convergence for a Monte Carlo solver using CMFD with a second order Crank-Nicholson discretization.

We have shown that the SLW model, and likely other similar global models, scale more efficiently for load imbalanced problems on parallel systems that are domain decomposed. Load balancing plays a strong role in the scaling efficiency of these models. The SLW model proved to be significantly less sensitive to the load imbalance associated with the Su Olson test problem we considered. Even though the SLW model showed scaling advantages, the overall computational time for the LBL model was smaller. This will not be true for all cases; problems that are more homogeneous and problems evaluated using deterministic methods may exhibit different scaling behavior. A more in depth study of different solvers and more advanced K-distribution methods is warranted. This requires the evaluation of a figure of merit because the accuracy of the solvers would be different.

Our research determined that for the relatively low mass fraction considered, the TRI effects are very insensitive to the addition of coal-type particulate. The primary differences observed are associated with differences in the turbulence initialization. This affects the temporal dependence of the mixture fraction variance, which drives the source terms associated with the radiation field. The treatment

of the particulate temperature has little effect at low mass loadings and becomes more dominant as the loading is increased. For large mass loadings, the treatment of the particulate temperature will effect the TRI parameters and the accuracy of the solution. The TRI effects associated with the emission source are reduced by the addition of optically thick, constant-temperature particulate. This will likely be reflective of real coal particulate opacities, which are relatively constant and thick compared to gas opacities. More simulations of the same problem should be performed different random initial states of the kinetic energy. This would help evaluate if the differences in the mixture variances are related to the initialization of the turbulence or the presence of the particulate. The addition of a simulation that is driven by the combustion of particulate would be very advantageous to evaluate changes in TRI effects when particulate fully drives the radiation source.

We have shown that a coarse mesh finite difference approach, with a high order integration scheme, can improve the temporal accuracy of a standard Monte Carlo approach as compared to Implicit Monte Carlo (IMC). We have been unable to directly evaluate the order of temporal convergence for the CMFD method with different temporal integration schemes because of statistical errors associated with the Monte Carlo solver. However, we did observe that CMFD with a Crank-Nicholson discretization is more accurate than either CMFD with a Backward Euler discretization or standard IMC. The development of dynamic statistical and numerical convergence criteria would greatly improve this approach.

Bibliography

[1] M. F. Modest, *Radiative heat transfer*, Academic Press (2003).

[2] G. Pal, A. Gupta, M. F. Modest, and D. C. Haworth, Comparison of Accuracy and Computational Expense of Radiation Models in Simulation of Non-Premixed Turbulent Jet Flames, *ASME Conference Proceedings*, **2011**, 38921, pp. T20116–T20116–10 (Jan. 2011).

[3] A. Wang and M. F. Modest, Spectral Monte Carlo models for nongray radiation analyses in inhomogeneous participating media, *International Journal of Heat and Mass Transfer*, **50**, 19-20, pp. 3877–3889 (Sep. 2007).

[4] K. Deshmukh, D. Haworth, and M. Modest, Direct numerical simulation of turbulence-radiation interactions in homogeneous nonpremixed combustion systems, *Proceedings of the Combustion Institute*, **31**, 1, pp. 1641–1648 (Jan. 2007).

[5] H. Park and D. Knoll, Moment-Based, Multiscale Solution Approach for Thermal Radiation Transport, (2011).

[6] J. Fleck and J. Cummings, An implicit Monte Carlo scheme for calculating time and frequency dependent nonlinear radiation transport, *Journal of Computational Physics*, **8**, 3, pp. 313–342 (Dec. 1971).

[7] S. Manickavasagam and M. P. Menguc, Effective optical properties of pulverized coal particles determined from FT-IR spectrometer experiments, *Energy & Fuels*, **7**, 6, pp. 860–869 (Nov. 1993).

[8] W. Barbour, C. Carner, M. Johnson, R. Morgan, R. Sacquety, and S. Scott, Carbon Dioxide Emissions from the Generation of Electric Power in the United States, Tech. rep., Department of Energy (2000).

[9] K. Okazaki and T. Ando, NOx reduction mechanism in coal combustion with recycled CO2, *Energy*, **22**, 2-3, pp. 207–215 (1997).

[10] N. G. Shah, *New method of computation of radiation heat transfer in combustion chambers*, Ph.D. thesis, Imperial College of Science and Technology, London, England (1979).

[11] L. L. Carter and E. D. Cashwell, Particle-transport simulation with the Monte Carlo method, Tech. Rep. TID–26607, USDOE (1975).

[12] T. F. Chan and J. P. Shao, Parallel complexity of domain decomposition methods and optimal coarse grid size, *Parallel Comput.*, **21**, 7, p. 10331049 (Jul. 1995).

[13] M. K. Denison and B. W. Webb, A Spectral Line-Based Weighted-Sum-of-Gray-Gases Model for Arbitrary RTE Solvers, *Journal of Heat Transfer*, **115**, 4, pp. 1004–1012 (Nov. 1993).

[14] A. Wang, M. F. Modest, D. C. Haworth, and L. Wang, Monte Carlo simulation of radiative heat transfer and turbulence interactions in methane/air jet flames, *Journal of Quantitative Spectroscopy and Radiative Transfer*, **109**, 2, pp. 269–279 (Jan. 2008).

[15] J. J. Duderstadt and L. J. Hamilton, *Nuclear reactor analysis* (1976).

[16] J. G. Marakis, C. Papapavlou, and E. Kakaras, A parametric study of radiative heat transfer in pulverised coal furnaces, *International Journal of Heat and Mass Transfer*, **43**, 16, pp. 2961–2971 (Aug. 2000).

[17] T. Downer, D. Lee, Y. Xu, T. Kozlowski, and J. Staudenmier, PARCS v2.6 U.S. NRC Core Neutronics Simulator, Tech. rep., Perdue (2004).

[18] K. Smith, Nodal method storage reduction by nonlinear acceleration, *Transactions of the American Nuclear Society*, **44**, pp. 265–266 (1984).

[19] A. Hummel, *Accelerating the Convergence of the k-Eigenvalue Problem using a Coarse Mesh Finite Differencing Scheme in Cylindrical Geometry*, Ph.D. thesis, Oregon State University (Dec. 2010).

[20] G. V.Ya., A quasi-diffusion method of solving the kinetic equation, *USSR Computational Mathematics and Mathematical Physics*, **4**, 6, pp. 136–149 (1964).

[21] D. Edwards and S. Morizumi, Scaling of vibration-rotation band parameters for nonhomogeneous gas radiation, *Journal of Quantitative Spectroscopy and Radiative Transfer*, **10**, 3, pp. 175–188 (Mar. 1970).

[22] D. Edwards and A. Balakrishnan, Slab band absorptance for molecular gas radiation, *Journal of Quantitative Spectroscopy and Radiative Transfer*, **12**, 10, pp. 1379–1387 (Oct. 1972).

[23] H. Zhang and M. F. Modest, Multi-group full-spectrum k-distribution database for water vapor mixtures in radiative transfer calculations, *International Journal of Heat and Mass Transfer*, **46**, 19, pp. 3593–3603 (Sep. 2003).

[24] M. K. Denison and B. W. Webb, The Spectral Line-Based Weighted-Sum-of-Gray-Gases Model in Nonisothermal Nonhomogeneous Media, *Journal of Heat Transfer*, **117**, 2, pp. 359–365 (May 1995).

[25] T. Rodolphe, A consistent multigroup model for radiative transfer and its underlying mean opacities, *Journal of Quantitative Spectroscopy and Radiative Transfer*, **94**, 3-4, pp. 357–371 (Sep. 2005).

[26] D. R. Reinert, Investigation of stochastic radiation transport methods in random heterogeneous mixtures, (2008).

[27] L. Liu, A concept of multi-scale modeling for radiative heat transfer in particle polydispersions, *Journal of Quantitative Spectroscopy and Radiative Transfer*, **78**, 2, pp. 227–233 (May 2003).

[28] L. Liu, Multiple size group analysis for transient radiative heating of particle polydispersions, *Journal of Quantitative Spectroscopy and Radiative Transfer*, **76**, 2, pp. 225–234 (Jan. 2003).

[29] P. Mendius, C. Harmon, R. Busch, J. Briesmeister, and R. Forster, Criticality calculations with MCNP $$sup TM$$: A primer, Tech. rep., Los Alamos National Lab., NM (United States) (1994).

[30] F. B. Brown and W. R. Martin, Stochastic geometry capability in MCNP5 for the analysis of particle fuel, *Annals of Nuclear Energy*, **31**, 17, pp. 2039–2047 (Nov. 2004).

[31] D. Haworth, Progress in probability density function methods for turbulent reacting flows, *Progress in Energy and Combustion Science*, **36**, 2, pp. 168–259 (Apr. 2010).

[32] G. L. Olson, D. S. Miller, E. W. Larsen, and J. E. Morel, Chord length distributions in binary stochastic media in two and three dimensions, *Journal of Quantitative Spectroscopy and Radiative Transfer*, **101**, 2, pp. 269–283 (Sep. 2006).

[33] D. S. Miller, F. Graziani, and G. Rodrigue, Benchmarks and models for time-dependent grey radiation transport with material temperature in binary stochastic media, *Journal of Quantitative Spectroscopy and Radiative Transfer*, **70**, 1, pp. 115–128 (Jul. 2001).

[34] L. Tess, F. Dupoirieux, and J. Taine, Monte Carlo modeling of radiative transfer in a turbulent sooty flame, *International Journal of Heat and Mass Transfer*, **47**, 3, pp. 555–572 (Jan. 2004).

[35] H. C. Hulst, *Light scattering by small particles*, Courier Dover Publications (1981).

[36] S. Apte, K. Mahesh, P. Moin, and J. Oefelein, Large-eddy simulation of swirling particle-laden flows in a coaxial-jet combustor, *International Journal of Multiphase Flow*, **29**, 8, pp. 1311–1331 (Aug. 2003).

[37] P. A. Bejarano and Y. A. Levendis, Single-coal-particle combustion in O2/N2 and O2/CO2 environments, *Combustion and Flame*, **153**, 1-2, pp. 270–287 (Apr. 2008).

[38] M. A. Cleveland, Extending the applicability of implicit Monte Carlo Diffusion : frequency dependence and variance reduction using the difference formulation, http://ir.library.oregonstate.edu/xmlui/handle/1957/9215 (Aug. 2008), graduation date: 2009.

[39] D. Knoll, W. Rider, and G. Olson, An efficient nonlinear solution method for non-equilibrium radiation diffusion, *Journal of Quantitative Spectroscopy and Radiative Transfer*, **63**, 1, pp. 15–29 (Sep. 1999).

[40] M. LEE, H. JOO, D. Lee, and K. Smith, Multigroup Monte Carlo Reactor Calculation with Coarse Mesh Finite Difference Formulation for Real Variance Reduction, (2010).

[41] E. R. Wolters, Hybrid Monte Carlo - Deterministic Neutron Transport Methods Using Nonlinear Functionals. http://deepblue.lib.umich.edu/handle/2027.42/84570 (2011), Ph.D.

[42] E. E. Lewis and W. F. Miller, *Computational methods of neutron transport* (1984).

[43] Z. Lan, V. E. Taylor, and G. Bryan, A novel dynamic load balancing scheme for parallel systems, *Journal of Parallel and Distributed Computing*, **62**, 12, pp. 1763–1781 (Dec. 2002).

[44] W. C. Reade and L. R. Collins, Effect of preferential concentration on turbulent collision rates. *Physics of Fluids*, **12**, 10, p. 2530 (Oct. 2000).

[45] T. Donovan and Y. Danon, Application of Monte Carlo Chord-Length Sampling Algorithms to Transport Through a Two-Dimensional Binary Stochastic Mixture, *Nuclear Science and Engineering*, **143**, 3, pp. 226–239 (2003).

[46] S. Torquato and B. Lu, Chord-length distribution function for two-phase random media, *Physical Review E*, **47**, 4, p. 2950 (Apr. 1993).

[47] Submodels-Radiation, http://www.sandia.gov/TNF/radiation.html.

[48] B. Su and G. L. Olson, Non-grey benchmark results for two temperature non-equilibrium radiative transfer, *Journal of Quantitative Spectroscopy and Radiative Transfer*, **62**, 3, pp. 279–302 (Jun. 1999).

[49] G. L. Olson, Gray radiation transport in multi-dimensional stochastic binary media with material temperature coupling, *Journal of Quantitative Spectroscopy and Radiative Transfer*, **104**, 1, pp. 86–98 (Mar. 2007).

[50] G. Wood, T. Kehn, M. D. Carter, and W. Culbertson, Circular 891 - Glossary of Coal Classification System and Supplementary Terms, Tech. rep., USGS (2003).

[51] B. T. S. Lundgren, Linearly forced isotropic turbulence, *Center for Turbulence Research*, **2**, pp. 461–473 (2003).

[52] V. Eswaran and S. B. Pope, Direct numerical simulations of the turbulent mixing of a passive scalar, *Physics of Fluids*, **31**, 3, p. 506 (1988).

[53] N. T. Myers, Evaluating preconditioning options for the Jacobian-Free Newton Krylov Method applied to radiative transfer with matter coupling, http://ir.library.oregonstate.edu/xmlui/handle/1957/21698 (Jun. 2011), graduation date: 2011.

A APPENDIX

A.1 Code

```
function get_plane_intersect(intersection,
   plane_normal, plane_point, vector_point_1,
   vector_point_2) result(intersect)

      implicit none
      logical, intent(inout) :: intersection
      real (WP) :: intersect(3)
      real (WP), intent(in), target ::
         plane_normal(3), plane_point(3),
         vector_point_1(3), vector_point_2(3)
      real (WP), pointer ::  a(:), p0(:), p1(:),
         p2(:)
      real (WP) :: lambda, x(3)

      a => plane_normal
      p0 => plane_point
      p1 => vector_point_1
      p2 => vector_point_2

      lambda = (a(1)*(p0(1)-p1(1)) + a(2)*(p0(2)-
         p1(2)) + a(3)*(p0(3)-p1(3))) &
      /(a(1)*(p2(1)-p1(1)) + a(2)*(p2(2)-p1(2)) +
          a(3)*(p2(3)-p1(3)))
      !print *, "[",myrank,"] lambda",lambda,
         plane_point
      !if(myrank==6) print *, "lambda = ", lambda
         , (a(1)*(p0(1)-p1(1)) + a(2)*(p0(2)-p1
         (2)) + a(3)*(p0(3)-p1(3))), &
      !          (a(1)*(p2(1)-p1(1)) + a(2)*(p2(2)-
         p1(2)) + a(3)*(p2(3)-p1(3)))
      if ( lambda < 1 .and. lambda > 0 ) then !
         if lambda is one then it stops at the
         face exactly so we default to stay in
         the cell
            intersection = .true.
            x(1) = p1(1) + lambda * (p2(1)-p1
               (1))
            x(2) = p1(2) + lambda * (p2(2)-p1
               (2))
            x(3) = p1(3) + lambda * (p2(3)-p1
```

```
                    (3))
                intersect = x
            else ! if lambda is greater then one it
                doesn't intersect the plane and if
                lambda is zero then it started from the
                current face or it is parallel to the
                plane
                intersection = .false.
                !FIXME: should check if sourced on
                    face. In this case Lambda will
                    be zero but p2 will not be
                    inside the current cell.
            end if

            nullify(a)
            nullify(p0)
            nullify(p1)
            nullify(p2)


        end function get_plane_intersect

function facet_area_diff(a, v)

  implicit none

  real (WP), intent(in) :: v(:,:), a(:)
  real (WP) :: facet_area_diff
  real (WP) :: facet_area
  real (WP) :: partial_area_sum

  integer :: vs(2), nd, nv, iv

  vs = shape(v)

  nd = vs(1)
  nv = vs(2)
  if (nd == 2) then      ! check if a is on the line
     if (nv > 2) then
        write(*,*) 'Error in facet_area_diffs'
        stop
     end if
```

```
      facet_area = sqrt(sum((v(:,2)-v(:,1))**2))
      facet_area_diff = abs(sqrt(sum((v(:,1)-a(:))**2)) &
           + sqrt(sum((v(:,2)-a(:))**2)) - facet_area) /
              facet_area

   else if (nd == 3) then

      facet_area = 0.0_WP
      do iv = 2, nv-1
         facet_area = facet_area &
              + 0.5_WP * cross_mag(v(:,iv)-v(:,1), v(:,iv
                 +1)-v(:,1))
      enddo

      partial_area_sum = 0.0_WP
      do iv = 1, nv-1
         partial_area_sum = partial_area_sum &
              + 0.5_WP *  cross_mag(v(:,iv)-a(:), v(:,iv
                 +1)-a(:))
      end do
      partial_area_sum = partial_area_sum &
           + 0.5_WP *  cross_mag(v(:,nv)-a(:), v(:,1)-a(:)
              )


      facet_area_diff = abs(partial_area_sum - facet_area)
          &
           / facet_area
   endif

   return

end function facet_area_diff
```